Tidal Tales of Minor Mergers:

Star Formation in the Tidal Tails of Minor Mergers

by

Karen A. Knierman

A Dissertation Presented in Partial Fulfillment
of the Requirements for the Degree
Doctor of Philosophy

Approved April 2013 by the
Graduate Supervisory Committee:

Paul Scowen, Co-Chair
Christopher Groppi, Co-Chair
Philip Mauskopf
Rogier Windhorst
Rolf Jansen

ARIZONA STATE UNIVERSITY

May 2013

ABSTRACT

This work examines star formation in the debris associated with collisions of dwarf and spiral galaxies. While the spectacular displays of major mergers are famous (e.g., NGC 4038/9, "The Antennae"), equal mass galaxy mergers are relatively rare compared to minor mergers (mass ratio < 0.3) Minor mergers are less energetic than major mergers, but more common in the observable universe and, thus, likely played a pivotal role in the formation of most large galaxies. Centers of mergers host vigorous star formation from high gas density and turbulence and are surveyed over cosmological distances. However, the tidal debris resulting from these mergers have not been well studied. Such regions have large reservoirs of gaseous material that can be used as fuel for subsequent star formation but also have lower gas density.

Tracers of star formation at the local and global scale have been examined for three tidal tails in two minor merger systems. These tracers include young star cluster populations, H-alpha, and [CII] emission. The rate of apparent star formation derived from these tracers is compared to the gas available to estimate the star formation efficiency (SFE). The Western tail of NGC 2782 formed isolated star clusters while massive star cluster complexes are found in the UGC 10214 ("The Tadpole") and Eastern tail of NGC 2782. Due to the lack of both observable CO and [CII] emission, the observed star formation in the Western tail of NGC 2782 may have a low carbon abundance and represent only the first round of local star formation. While the Western tail has a normal SFE, the Eastern tail in the same galaxy has an low observed SFE. In contrast, the Tadpole tidal tail has a high observed star formation rate and a corresponding high SFE. The low SFE observed in the Eastern tail of NGC 2782 may be due to its origin as a splash region where localized gas heating is important. However, the other tails may be tidally formed regions where gravitational compression likely dominates and enhances the local star formation.

DEDICATION

For Patrick, my love.

To my family by blood whose love has been with me from the beginning and my family by choice whose love has blossomed through the years, you are all family of my heart. Thank you for your unending love and support.

In memory of my beloved grandparents, Beulah & Earvin Cash and Louise & Paul Knierman, Aunt Gertie, Aunt Betty, Sr. Kathleen Blair, “Aunt" Irma, Mrs. Ginny Spaeder, Sr. Regina, and all those who have gone before.

Thank you to my wonderful Earth Science teacher Sr. Martha Ann & Carl Sagan for inspiring my love of astronomy and to Prof. Roger Knacke at Penn State Behrend for setting up “Open House Nights in Astronomy" where my first look through a telescope was at Jupiter on the night of July 16, 1994.

I have been blessed with so many amazing & caring teachers, administrators, and school staff throughout my life. From St. George School (Miss Young, Sr. Jenny, Mr. Schroeck, Miss Arnold, Miss Morgan, Kay, Miss Spenik, Mrs. Gunter, Sr. Bernadette, the Cafeteria staff, Sr. Becky, Fr. Mike, Mr. Callaghan, Miss Piszker, Mr. Donch, Mrs. Van Den Honert, Mrs. Baltes, Katie, George, Mrs. Buzanowski), to the Prep Band (Mr. Stevens, Mr. Sherman, Mr. Hannah, & D. Nawrocki), to Villa Maria Academy (Mrs. Walker, Mr. Gardner, Sr. Martha Ann, Sr. Anne Marie, Mrs. Stadtmiller, Miss Wilson, Mr. Hall, Miss Massello, Mrs. Trambley, Mrs. Hughes, Mrs. Fitzreiter, Mrs. Blatt, Ms. Swartzfager, Mrs. Kirkwold, Mrs. Vitron, Ms. Tann, Mr. Ek), & Penn State (Dr. Schneider, R. Ciardullo, M. Eracleous, N. Brandt, L. Ramsey, R. Wade, R. Downs), thank you all for your time and attention over the years.

“The price of anything is the amount of life you exchange for it." - Henry David Thoreau

ACKNOWLEDGEMENTS

Observations used the Vatican Advanced Technology Telescope (VATT), NASA/ESA Herschel Space Observatory, & the Kitt Peak 12 Meter (Arizona Radio Observatory). P. Young, R. Cool, W. Liu, M. Prescott, K. Finlator, J. Monkiewicz, and I. Momcheva assisted with VATT observing. R. Kennicutt provided access to his narrowband filters. J. Lee, S. Sakai, & J. Funes provided assistance with Hα calibration. U. Lisenfeld & J. Hibbard provided IRAM and VLA data. Funding provided by the Univ. of Arizona/NASA Space Grant Graduate Fellowship (2004-2006), NASA Herschel Science Center, teaching assistantships, and the Hubble Space Telescope E/PO Project "Sharing Gravity's Microscope". Amazing scientific feedback & support was provided by my advisors: Paul Scowen & Chris Groppi. Helpful comments & feedback provided by committee members: Philip Mauskopf, Rogier Windhorst, & Rolf Jansen. P. Knezek, E. Wehner, B. Mullan, I. Konstanopolous, J. Charlton, T. Veach, & two anonymous referees provided detailed comments on sections of this work. P. Massey & L. Amundson provided assistance obtaining a reference. Ample thanks to Teresa, Becca, & Becky for assistance above and beyond the call of duty. N. Hinkel, H. Kim, & M. Rutkowski provided dissertation formatting assistance. Fruitful discussions with B. Whitmore, N. Bastian, J. Monkiewicz, P. Young, Y. Shirley, S. Cohen, C. Kaleida, H. Kim, C. Kulesa, A. Hedden, M. Prescott, J. Gallagher, E. Wilcots, M. Bershady, E. Barton, D. McCarthy, J. Feldmeier, P. Durrell, J. Bailin, J. Rigby, A. Leistra, E. Mamajek, & S. Malhotra helped shape this work. Thanks to the esteemed faculty on my dissertation committee at Univ. of Arizona & the Academic Program Committee Chair at Steward Observatory, who deemed my prestigious NSF AAFP fellowship unworthy of acceptance, leading me to this fruitful 6-year career detour at Arizona State University. Your objectivity & professionalism will be long remembered. Thank you to the School of Earth and Space Exploration for providing a wonderful

interdisciplinary environment where I could learn about water on Mars & study distant galaxies. Thank you to Astronomy Campers & staff, Girl Scouts, Earthwatch, W. Taylor, M. Hufford, B. Grigsbee, L. Rogers, MSIP students & teachers for helping me find my calling and encouraging me to finish this work.

Sanity provided by Danu (Angelia & Joy), the present & past members of Vorpal Shimmy (Meghan, Jacque, Kelly, Patrick, Evan, Kay, Jen, Themis, Rosie, Nahks, Kaely), Indigo Fire, Entropy Fire, my dance teachers, & Laughing Buddha Yoga Studio. Thanks, Beth, for introducing me to tribal fusion & fire arts. Thank you to Cassie, Teresa, Angel, Brian, Mark, Kim, Ray, Brent, Mike, Luke, & Boom for help with outreach. To RPGers including Ry, Tom, Krystal, Thomas, Paul, Jeff, & Scott, thanks for keeping the laughter & dice rolling. Forward momentum & inspiration provided by Vorkosigans, LMB, J.A. Owen, TORC, FB, CPB, ASC, PGSS, JIFC, & OPL. Thank you to Endo, Abbott, Alaven, Salix, Forest, Wyeth & GlaxoSmithKline. To my family by choice, Aunt Jerri & Uncle Harold, Barbara Warren, the Segals, Meghan, Evan, the Drapers, Jackie, Jacque, Kit, Tony, Terry, Margaret, Zimmermania, Gregg, Peter, Jon, Katrina, Jen, Amy, David, Anne, Dave, & Bette, thank you for your laughter, support, & love. Much love to my parents, August & Shirley Knierman, my brothers, Paul, Mike, & Pat, who inspired me to explore the universe, & to Paul, Olivia, Matt, Joe, Alex, Rachel, & Kaitlyn for your boundless wonder & inspiration. Special thanks to my brother Mike for inspiring my love of science, to Pat for attending my defense, & to my Aunt Pauline & Uncle Dale who have been so very supportive throughout my scholastic endeavors. And also to my sisters-in-law, aunts, uncles, & many cousins, including my godmother Mary Lou and my godchild Megan, for their love and support. Love, purrs, & cuddles were kindly provided by Shilhiriel, Ashel, & Rhianwe. Abundant love & gratitude goes out to Patrick Young, who endured so much & gave up so many things (such as a honeymoon) to see this work completed.

TABLE OF CONTENTS

LIST OF TABLES

LIST OF FIGURES

Figure Page

Chapter 1

INTRODUCTION

This work focuses on galaxies that are merging. Merging galaxies are most often classified as irregular or peculiar rather than as regularly shaped spiral and elliptical galaxies. These mergers are often characterized by disturbed morphologies and can often have long narrow tails or plumes possibly extending from their chaotic centers. See Figure 1.1 for example images of galaxy mergers from the Atlas of Peculiar Galaxies (Arp, 1966). Possibly the first recognition of peculiar galaxies as collisions or "capture" is by Holmberg (1941), who performed the first simulation of a galaxy collision, long before computers were up to the task. His analog simulation discovered that galaxies can lose enough kinetic energy to thermal energy that they will merge together. In addition, tidal forces in the collision can deform the galaxies. Further simulations (e.g., Toomre & Toomre, 1972; Barnes & Hernquist, 1996) have shown that whether or not two galaxies merge together is a function of their mass, their distance apart, and their relative velocities. If two galaxies are moving too fast, the increase in internal energy cannot make up for the high kinetic energy, and then they do not merge together.

There can also be different types of mergers. If two galaxies are the same or very similar mass (with mass ratios of 1:1 down to 1:3), this type of merger is classed as a major merger. Often, these are defined as the merger of two spiral galaxies. Toomre & Toomre (1972) and subsequent simulations show that the end result of major merger of two spiral galaxies may resemble an elliptical galaxy since the regular orbits of stars in a spiral are thrown into the random orbits of a spheroid. Lower mass ratio mergers (less than 1:3 to 1:10) are generally classified as minor mergers. These can be mergers between a massive elliptical galaxy and a smaller spiral galaxy or between a small dwarf galaxy and a larger spiral galaxy. In

this work, a minor merger is considered to be between a small dwarf galaxy and a larger spiral galaxy.

The tidal tails of merging galaxies are caused by the tidal forces of the interaction that pull on opposite sides of the galaxies, launching tails both toward the other galaxy and on the opposite side. After the first passage of two galaxies, the tidal tails begin to extend and a bridge is formed between the two galaxies. As the galaxies then spiral in towards each other, the bridge disappears (consumed in the collision) while the tails continue to move outward. The end fate of the tidal tails is debated; certainly some of the tail material will return to the main merger remnant, but some of it may reach escape velocity from the merger and contribute to the material that exists between galaxies, the intergalactic medium (IGM). These tidal tails can be very gas rich and some have larger conglomerations of gas and stars in them that have masses, similar to dwarf galaxies. These entities are referred to as Tidal Dwarf Galaxies (TDGs), although there is debate about whether they will survive the merger to become a separate dwarf galaxy of their own or if they will dissolve or be consumed by the main merger remnant. Smaller in scale than small dwarf galaxies, tidal tails can also have star clusters which are compact groups of stars on the order of $10^4 - 10^6$ $M_\odot$.

1.1 Motivation

How does the tidal debris of minor galaxy mergers contribute to structures in spiral galaxies or in the IGM? Major mergers (e.g., two spiral galaxies) are known to create structures such as TDGs and star clusters within their debris (e.g., Duc et al., 2000; Weilbacher et al., 2002; Knierman et al., 2003; Mullan et al., 2011). While the spectacular displays of major mergers are well known (e.g., NGC 4038/9 "The Antennae"; Whitmore et al., 1999) interactions between equal mass galaxies are relatively rare compared to unequal mass mergers ($M_2/M_1 < 0.3$ Lotz et al., 2011).

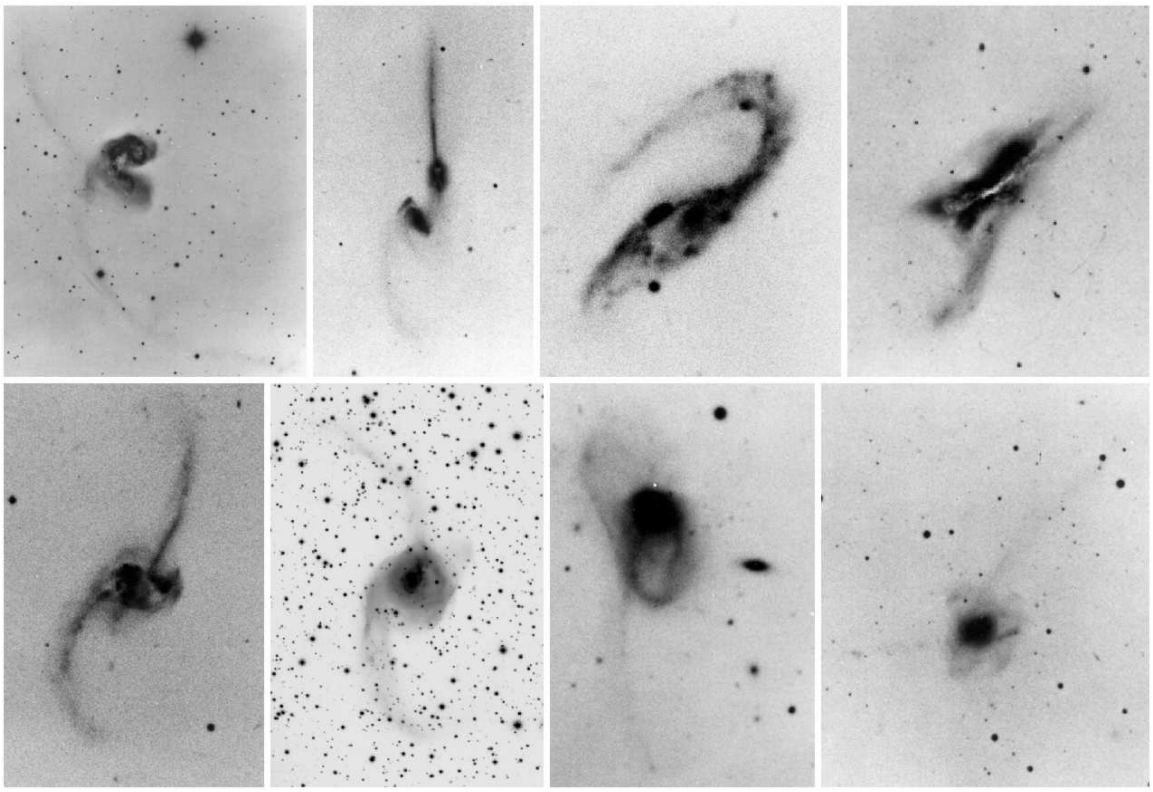

Figure 1.1: A montage of Toomre Sequence galaxies (Toomre, 1977) taken from the Atlas of Peculiar Galaxies (Arp, 1966).

In Cold Dark Matter (CDM) models of structure formation, minor mergers are predicted to be of fundamental importance in shaping galaxy properties. Indeed, galaxy-size CDM halos are predicted to gain most of their mass in 10:1 merger events (Zentner & Bullock, 2003) and these events are expected to be much more common in the past than they are in the local universe. Minor mergers are less affected by dynamical friction than major mergers, and we generally expect tidal tails in these encounters (see e.g., the Sagittarius dwarf and tidal stream around the Milky Way; Ibata et al., 1997).

The work is motivated not just by the general importance of understanding how these frequent encounters shape galactic structure, but also as a probe of star formation in gas that may be on the edge of "stability". Minor merger tidal streams also are important for understanding stellar halo formation and potentially IGM

enrichment. For example, tidally liberated stars that remain bound to the larger galaxy after a minor merger event are believed to play a fundamental role in building galaxy stellar halos (e.g., Searle & Zinn, 1978; Bullock & Johnston, 2005). An important puzzle in this case is that the chemical abundance pattern of Milky Way stellar halo stars does not match that of (non-interacting) Local Group dwarfs (e.g., Venn et al., 2005). Star formation that occurs in the tidal arms may have important implications for understanding these enrichment patterns. It is important then to characterize the rate of star formation in tidal debris and to estimate whether it could contribute significantly to the diffuse halo. It is also possible that tidal material is thrown out into the IGM after minor encounters. If so, then this will be an important factor in understanding the metallicity of the IGM. Finally, in the case of TDGs, frequent minor mergers over the last ~ 10 Gyr could have contributed significantly to the dwarf galaxy population in the universe. Therefore, studying the formation of structure in the tidal debris of minor mergers can help us understand a common process in galaxy formation.

1.2 Major Mergers

Significant work has been done on major mergers. Beginning with such work by Holmberg (1941) and Toomre & Toomre (1972), mergers have been seen as an important part of galaxy evolution. The Toomre Sequence (Toomre, 1977) was put together as an ordering of ongoing mergers in a time sequence from two galaxies just coming together to those which have already merged into one galaxy. This sequence is an optically selected ensemble of strongly interacting galaxies representing a suggested evolutionary sequence of disk–disk mergers, based on their stellar tidal tail lengths and the separation of the two nuclei (Toomre, 1977).

1.2.1 Observations

Tidal tails in major mergers have blue $UBVR$ colors (e.g., $B-V=0.53\pm0.13$ from Schombert et al. (1990); see also Weilbacher et al., 2000), and regions of [OII] and Hα line emission have been found within the tails (Schweizer, 1978; Mirabel, Dottori, & Lutz, 1992; Duc & Mirabel, 1998, 1999; Iglesias-Páramo & Vílchez, 2001; Weilbacher, Duc, & Fritze-v.Alvensleben, 2003). The inferred ages of the young stars and giant HII regions are much less than the dynamical age of the tails, indicating that star formation is occurring within the tails. Observations of 21 cm neutral hydrogen (HI) observations indicate that tails are gas rich (Yun, Ho, & Lo, 1994; Hibbard et al., 2001), and the evolution of the HI therein may play a role in the star formation history. Many tidal tails have associated HI which is falling back toward the center into the remnant. The infalling gas onto the central regions may enable star formation to continue for time scales on the order of 1 Gyr after tail formation (Hernquist & Mihos, 1995). Finally, tidal dwarf galaxies are found in tidal tails in a variety of environments, particularly at the ends of the tails (Mirabel, Dottori, & Lutz, 1992; Duc & Mirabel, 1994; Hunsberger, Charlton, & Zaritsky, 1996).

1.2.1.1 Star Clusters

Even though Knierman et al. (2003) identify dozens of young compact clusters ($0.2<V-I<0.9$) in the tidal tails of NGC 3256 (after background corrections), they find that not all tidal debris forms an abundance of these objects; the other three Toomre Sequence mergers in their study, NGC 4038/9 ("The Antennae"), NGC 3921, and NGC 7252 have only a few compact clusters within their tails. Small populations of compact star clusters in the tidal debris are found in the Cycle 11 Early Release Observations of NGC 4676 ("The Mice") major merger (de Grijs et al., 2003). With only a few examples of cluster–rich debris, we do not yet know

how common it is for tidal star formation to result in a population of compact clusters. A number of variables are likely to affect the nature of star formation in merging systems: the environment of the merging system, the stage of the merger, the mass ratio of the individual galaxies, and the gas properties, size and surface density of the tails.

The super star clusters tend to have blue colors ($V - I \sim 0.5$; Knierman et al., 2003) ($B - V \sim -0.2$; de Grijs et al., 2003) with young ages indicating they formed within their tidal tail. Three star clusters in the Western Tail of NGC 3256 were spectroscopically confirmed by Trancho et al. (2007) at Gemini South. From their GMOS-S spectra, they determine ages to be ~ 80 Myr for two star clusters and ~ 200 Myr for the third, assuming approximately solar metallicities. The three star clusters in the Western tail of NGC 3256 have masses of $1 - 2 \times 10^5$ $M_\odot$. Using the HST/WFPC2 images of the Western tail of NGC 3256, Trancho et al. (2007) show the three star clusters to have a large size ($r_{eff} \sim 10 - 20$ pc) compared to Milky Way globular clusters or other young massive clusters ($r_{eff} \sim 3 - 4$ pc). The large size of the star clusters may mean that the giant molecular cloud (GMC) underwent weak compression during the star cluster formation. On the other hand, the tidal tail star clusters may not have experienced the tidal stripping that other young clusters in the centers of galaxies have.

Chien et al. (2007) observed twelve star clusters in the Mice with Keck/LRIS to determine ages and metallicities. These star clusters were discovered with ACS Early Release Observations by de Grijs et al. (2003). de Grijs et al. (2003) found more than 40 star clusters in the tails of NGC 4676. Of the brighter clusters observed, Chien et al. (2007) confirmed 6 star clusters in the Northern tail and 4 star clusters in the Southern tail. The Northern tail star clusters have ages from 2.7-7.1 Myr and one with an age of 163 Myr. Their metallicities are greater than solar and form a tight range of $8.92 < 12 + \log(O/H) < 8.97$. In the Southern tail,

ages range from 2.5-6 Myr with one at 172 Myr. One star cluster has a low metallicity of $0.04 Z_{\odot}$ with the others having metallicities comparable to star clusters in the Northern tail. The Northern tail has a flat metallicity distribution, which provides evidence that gas mixing occurred there. The older star clusters in the tails likely formed via shock induced star formation when the first passage of the two galaxies occurred ~ 175 Myrs ago (Barnes, 2004).

1.2.1.2 Tidal Dwarf Galaxies

Mergers of large equal mass galaxies, such as NGC 4038/39 ("The Antennae") and NGC 7252, can create star clusters and clumps of star forming material, often called TDGs, in their tidal debris (Knierman et al., 2003; Duc et al., 2000). TDGs are blue condensations at the tips of tidal tails and have H I masses ranging from $0.5 - 6 \times 10^9$ $M_{\odot}$. They also have properties consistent with dwarf irregulars or blue compact dwarf galaxies regarding surface brightness, blue colors, and strong star formation bursts, but have higher metallicities (Duc et al., 2000). By their metallicity, the TDGs are shown to have been pulled out from the outer regions of the spiral disk.

Evidence for internal dust extinction has been found in other TDGs (e.g., Temporin et al., 2003). With both optical and near–IR images and optical spectra of the TDGs, they show that $V - K$ colors support the evidence for the large amount of dust as determined from the Balmer decrement in the optical spectra.

Weilbacher et al. (2002) has optical (BVR) and near–IR (H, some JK_s) images as well as optical spectra of 14 mergers including the 13 TDGs. Their sample was chosen from the Arp & Madore (1987) catalog and was based on the chaotic shape of the merger and the presence of any probable knots in the tidal features (see also Duc et al., 2000; Schombert et al., 1990). Using SED fitting, they discover that the TDGs in their sample of major mergers have both old and young stellar populations.

1.2.2 Simulations of Major Mergers

Even in early simulations, tidal tails were found to form during the process of major mergers. The earliest analog simulations of Holmberg (1941) found "spiral arms" forming in the two disks which are the precursors to tidal tails. In this paper, the first simulations of galaxy collisions are described. This simulation used 74 light bulbs to represent mass particles in the two colliding galaxies and the inverse square law of light as stand in for gravity. This analog simulation did discover that the two galaxies are deformed tidally, mostly after the first passage. As a result of this deformation, the gravitational attraction between the two galaxies increases. The kinetic energy of the two galaxies moving past each other is converted into internal energy in the galaxies and the decrease in orbital kinetic energy can be enough that the two galaxies merge together. Figure 1.2 shows results of this simulation including indications that prograde encounters (both galaxies have the same sense of rotation) will make longer tidal tails. The early N-body computer simulations of Toomre & Toomre (1972) find bridges and tidal tails forming in their simulation of several mergers including NGC 4038/9. Further simulations of major mergers by Barnes (1988) confirmed this early result. Later models included prescriptions for star formation using an equation of state for the gas density (e.g., Barnes, 2004) which found that only about $\sim 10\%$ of the star formation of the merger would be in the tidal debris and may be caused by shocks.

Recent major merger simulations by Hopkins et al. (2013) include many state of the art features unavailable in previous decades. Using over 200 million particles, these simulations can reach down to ~ 1 pc scales. Included in the simulations are realistic feedback mechanisms in the interstellar medium (ISM). This feedback includes momentum from stellar radiation pressure, radiation pressure from star forming regions, HII photoionization heating, and heating,

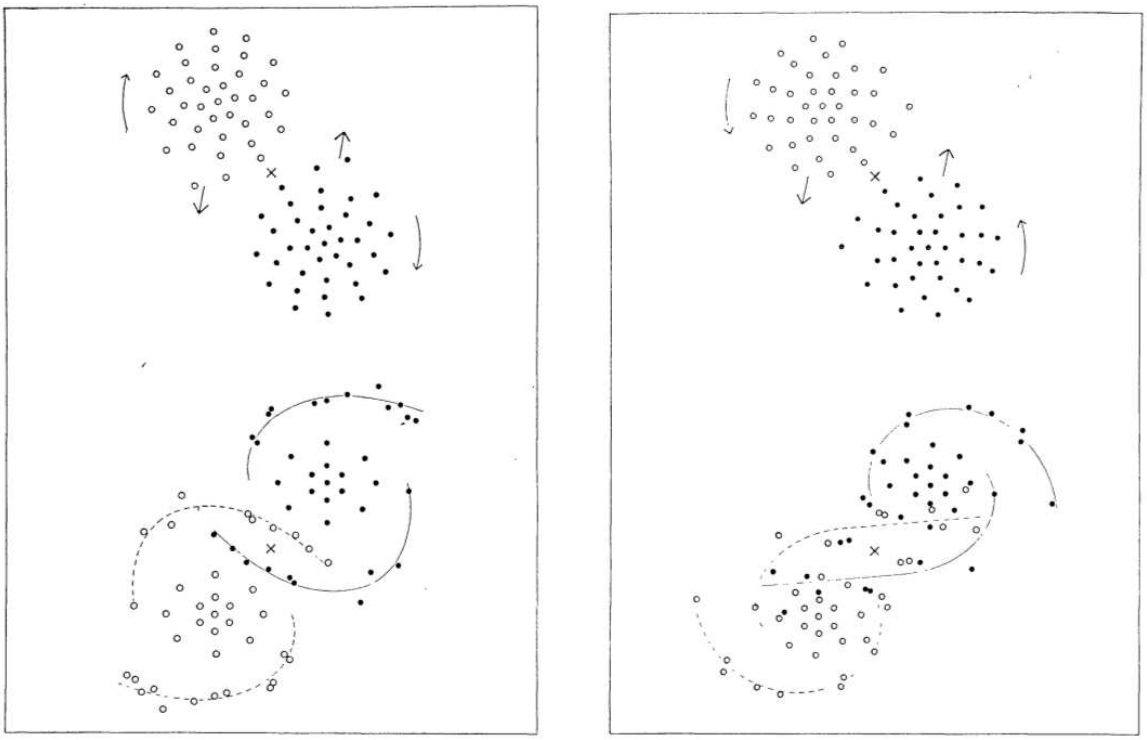

Figure 1.2: Diagrams of the first merger simulation (Holmberg, 1941) showing the position of light bulbs before and after the collision. Left: Retrograde encounter where the two galaxies have opposite rotation. Right: Prograde encounter where the two galaxies have the same sense of rotation.

momentum, and mass loss from SNe I and II and stellar winds of O and AGB stars. Other improvements include realistic cooling of gas to < 100 K and treating the transition between atomic and molecular gas and its effect on star formation. The resulting simulations find that the star formation in mergers is more bursty than in previous simulations and that the star burst associated with the first passage of the two galaxies is sensitive to the orbital parameters and initial structure of the galaxies. Due to the better treatment of star formation on small scales, the Hopkins et al. (2013) models show that $20 - 50\%$ of star formation in the merger can be in tails and bridges, which is higher than previous models ($\sim 10\%$; Barnes, 2004).

1.2.2.1 Formation of TDGs

Numerical simulations of major mergers indicate that there may be two different methods for building TDGs. Barnes & Hernquist (1996) predict that a stellar component is pulled out from the outer regions of the parent galaxy followed by an infall of gas into the potential well of the TDG. Elmegreen, Kaufman, & Thomasson (1993) propose that gas condenses first in the debris and stars form in the gas. In another study, Weilbacher et al. (2002) performed an observational study of 14 interacting systems (mostly major mergers and groups) in which they found 13 TDG candidates. Using evolutionary synthesis modeling of TDGs from their optical and near–infrared colors, they produce spectral energy distributions which they compare to their models. They find that the majority of TDGs in their sample have an old population of stars along with the new population, indicating that the TDGs formed from stellar clumps rather than gas cloud instabilities (which consist of only a young population). However, HI studies of a few individual pairs (e.g. NGC 7252; Hibbard et al., 1994) detect a large HI cloud in the tidal debris indicating that TDGs formed from gas cloud instabilities.

1.2.2.2 Star Clusters in Merger Simulations

While many simulations have touched on the formation of massive structures in tidal tails such as TDGs (Barnes, 1998), few have the resolution needed to study the less massive super star clusters. In their simulations of major mergers, Duc, Bournaud, & Masset (2004) find that the formation of massive TDGs ($> 10^9$ $M_\odot$) is different from the formation of super star clusters. TDGs are formed via a kinematical process where material accumulates in the tail via tidal forces (often at the tip of the tail) and then later gravitationally collapses. In contrast, the less massive super star clusters (SSCs) form via local gravitational instabilities along the

tails. Their simulations also show that it is not necessarily the case that the two types of structure do not both form in the same tidal tail. However, with the TDG using about 75% of material in the tail there is not much material left to form SSCs. These findings may be connected to the observations of Knierman et al. (2003) which found that major merger tidal tails form either star clusters along the tidal tail or a TDG which hosts star clusters within it. Recent simulations by Hopkins et al. (2013) are able to resolve down to star cluster scales, but detailed analysis of when and where they might form in the tidal debris is awaited.

1.3 Minor Mergers

Minor mergers have been defined in several ways in the literature. One way is to define those interactions as minor where the mass ratio is < 0.1. Intermediate interactions are then defined as those where the mass ratio is between 0.1 and 0.25 (or 0.5). This use of mass ratios can then be used to refer to interactions between a massive elliptical and regular spiral galaxy as minor. Others define minor mergers as interactions which preserve the disk of the larger spiral galaxy, whereas major mergers disrupt the disk orbits ending with an elliptical galaxy. In this study, minor merger will refer to an interaction between a spiral galaxy and a smaller galaxy where the mass ratio is less than ~ 0.3 which preserves the disk structure.

1.3.1 Observations

While some work on tidal debris in minor mergers has been done on an individual galaxy basis, no comprehensive study has been accomplished to date. An example of a minor merger in this work, UGC 10214 ("The Tadpole"), has been studied in HI by Briggs et al. (2001) who discovered the presence of a dwarf galaxy behind the western side of the spiral disk. The mass ratio between the large spiral galaxy and the dwarf galaxy that perturbed it is 0.15. There is HI located in the long streamer

and Briggs et al. (2001) speculate that this interaction is different from simulated major mergers (like NGC 7252; Hibbard et al., 1994) in the low mass of the companion and its high velocity in the encounter. HST/ACS ERO of UGC 10214 in F475W (g), F606W (broad V), and F814W (I) show 2 large concentrations of material mid-point along the tidal tail and very blue colors of the tidal debris. Small populations of compact star clusters in the tidal debris are found along the tidal tail of the Tadpole (Tran et al., 2003; de Grijs et al., 2003).

Several groupings of star clusters were discovered in VLT observations of the tidal tails of the minor merger NGC 6782 (Bastian et al., 2005b). These star clusters have ages from 1-100 Myr with masses ranging from $10^4 < M/M_\odot < 10^7$. The ages of the young star clusters are conducive to having formed within the tidal tails which have an age of ~ 130 Myr from N-body simulations by Horellou & Koribalski (2007). These simulations match the morphology of the merger, particularly the tail length and thinness of the southern tail. Horellou & Koribalski (2007) also compare the locations and properties of star clusters in Bastian et al. (2005b) with the HI distribution. They find that the ends of the tidal tails which are low in HI host young, low mass, and low extinction star clusters.

Another sample galaxy is NGC 2782. With VLA HI data, Smith (1994) constrains dynamical models such that a head–on interaction between a large disk galaxy and a lower mass disk galaxy ($M_2/M_1 \sim 0.25$) occurred, leaving a stellar plume in the eastern tail with a putative TDG contained there (Smith, 1994) and a long HI-rich western tail. A five minute exposure in R from WIYN (Jogee et al., 1998) shows a faint western tail at high stretches.

In NGC 3310, another minor merger, Kregel & Sancisi (2001) discover a large southern HI extension. This galaxy may have cannibalized a dwarf galaxy, perhaps as recently as 10 Myrs ago based on its "bow and arrow" structure as well

as the presence of very young super star clusters in the central regions (Conselice et al., 2000; Elmegreen et al., 2002). The Hubble Heritage image[1] of this galaxy only contains the central region and not the brighter optical tidal debris located a few arcminutes from the center or the extended HI area. Wehner & Gallagher (2004) study the tidal debris of NGC 3310 and find a new loop of tidal debris located around the outskirts of this system.

Ferreiro, Pastoriza, & Rickes (2008) observe a sample of minor mergers using Hα observations. They discover more massive structures in the tidal tails such as HII regions and Tidal Dwarf Galaxies with very few star clusters detected. The masses of the HII regions in the tidal tails range from 10^6 $M_\odot$ to 3×10^7 $M_\odot$ and indicate that minor mergers can form objects of similar mass to TDGs.

1.3.2 Simulations

N-body simulations have given insight into minor mergers starting with Toomre & Toomre (1972) who studied 1:4 mass ratio interactions as well as 1:1 mass ratio interactions (see Figure 1.4). They found that direct encounters produce more extended tidal features because the orbits of the particles in the disk are near resonance and are matching the orbital angular speeds. Also, the unequal mass mergers produced longer lived bridges between the galaxies, but tails formed more in equal mass mergers. True tails that escape to infinity required the violent interactions of major mergers, however, the minor merger has 4 out of 120 particles that do escape the merger. Later work by Barnes (1998) shows that in comparison of 1:1 and 1:3 mass ratio simulations, the equal mass mergers show more extended tidal features and confirm that direct passages produce more impressive bridges and tails. In addition to the creation of tidal debris, Mihos & Hernquist (1994) and Walker et al. (1996) show the ability of minor mergers to fuel central starbursts by

[1] http://heritage.stsci.edu/2001/26/

driving gas into the centers of the larger galaxy. Also, minor mergers can induce spiral arms, bars, and warps and cause the disk not to be destroyed but to heat and thicken, and the merged satellite to enhance the bulge (see Figure 1.5). Hence, minor mergers can cause a spiral galaxy to evolve to an earlier Hubble type.

Bullock & Johnston (2005) model the formation of the halo of a Milky Way-type object using a hybrid semianalytic plus N-body approach. Their model separates the light and dark matter evolution to determine resulting structures of both the stellar and dark matter halos. They reproduce properties of the current Milky Way satellites and find that the luminosity of those satellites that were accreted in the simulation matches the current estimates of stellar halo luminosity (10^9 $L_\odot$). The stellar halo is more concentrated than the dark matter halo, forms inside out, and has most of its mass coming from the ∼15 most massive accreted satellites, which are dwarf-irregular galaxies with masses of $\sim 10^{10}$ $M_\odot$and luminosities of $\sim 10^7 - 10^9$ $L_\odot$. These satellites were accreted and destroyed ~ 9 Gyr ago or longer whereas the surviving dwarf galaxy population were captured ~ 5 Gyr ago. Therefore, the stars in the inner halo come from massive satellites that were accreted > 9 Gyr ago. However, the current dwarf galaxy satellites are lower mass and were captured later. This prediction matches the observed differences in chemical abundance between halo stars and those within the current dwarf satellite population of the Milky Way (Venn et al., 2005).

Pisano & Wilcots (2003) examine analytic estimates of orbital timescale, dynamical friction timescale, and tidal mass for a sample of 13 companions to 10 isolated galaxies. Their analysis begins with orbital timescale given by

$$t_{orbit} = \frac{2\pi\Delta R}{\Delta V} \tag{1.1}$$

where M_{comp} is the mass of the companion galaxy, ΔR is the separation of

the companion from the main galaxy, and ΔV is the velocity difference between the two. Simulations of minor mergers by (Walker, Mihos, & Hernquist, 1996) show satellite orbits decaying within a few orbital times. The comparison continues with the dynamical friction timescale

$$t_{dyn.fric.} = \frac{2.5 \times 10^{14} \Delta R^2 \Delta V}{M_{comp} ln\Lambda} yr \tag{1.2}$$

where

$$\Lambda = \frac{\Delta R \Delta V^2}{M_{comp} G} \tag{1.3}$$

This dynamical friction timescale characterizes the amount of time required for a companion within the primary's dark matter halo to spiral into the primary's center. This formula assumes an infinite isothermal halo with no gaseous medium and so may be high by factors of 2 or more. Both of these estimates assume a circular orbit (which Pisano & Wilcots (2003) find to be the most common type of orbit in their sample). They find that t_{orbit} ranges from 2 to 115 Gyr, with a median of 6 Gyr. The value of $t_{dyn.fric.}$ is in general higher, ranging from 3 to 138 Gyr with a median of 8 Gyr. Half of the sample should be accreted within a Hubble time with these simple assumptions. The companions showing evidence of interaction have the shortest timescales. Pisano & Wilcots (2003) then evaluate the stability in terms of the Dahari parameter:

$$Q_D = \frac{M_{comp}/M_{gal}}{(\Delta R/R_{gal})^3} \tag{1.4}$$

where $Q_D > 1$ is considered a strong reaction and $Q_D \sim 0.1$ is a weak interaction. All of the interacting galaxies in the sample have Q_D ranging from a few times 10^{-4} to 10^{-2}.

Seven of the companion galaxies have a Jacobi limit

$$r_J = \pm(\frac{M_{comp}}{3M_{gal}})^{1/3}\Delta R \tag{1.5}$$

less than their observed radius in HI. The Jacobi limit is an approximation to the tidal radius at the current distance of the galaxy. It appears that even for a sample of field galaxies in the local universe outside of groups, roughly half will accrete their companions within a Hubble time, increasing their gas mass by 5-50% an undergoing a burst of star formation.

1.4 The Local Group

The Local Group of galaxies consists of 3 larger spiral galaxies (our own Milky Way galaxy, the Andromeda Galaxy (M31), and the Triangulum Galaxy (M33)) along with many smaller dwarf galaxies. While the major merger in the Local Group, between the Milky Way and Andromeda, will not occur for another 3 Gyr, minor mergers are more common. Since minor mergers can contribute structures such as star clusters and streamers to their parent galaxies, the properties of these objects in the Local Group are examined.

1.4.1 Super Star Clusters and Globular Clusters

Since SSCs are found in mergers, some local analogs of these star clusters are reviewed here. A new class of extended, luminous globular clusters was discovered in the outskirts of M31 (Huxor et al., 2005). The large half light radius (~ 30 pc) and bright luminosities ($M_V \sim -7$) are unusual for globular clusters. Color magnitude diagrams show that these star clusters are old (> 10 Gyr) and metal poor (Mackey et al., 2006).

There are a few nearby resolved clusters with stellar masses approaching those found in this study, namely the Arches, NGC 3603 Young Cluster (YC), 30 Dor, and Westerlund 1, at $7 \times 10^3 M_\odot$, $7 \times 10^3 M_\odot$, $2 \times 10^4 M_\odot$, and $1 \times 10^5 M_\odot$, respectively. All of these clusters contain large numbers of O stars, including multiple O3 stars, and so have ages less than 2-3 Myr. The latter three clusters extend to 3-4pc, while the Arches has an extent of $\sim$1 pc, probably due to the Galactic Center tidal field. Unlike the Arches and NGC 3603 YC, 30 Dor has an extended halo out to 130 pc. 30 Dor has $B - V = +0.13$ and $U - B = -0.75$. NGC 3603 YC contains 37 early O stars, while 30 Dor and Westerlund 1 contain 52 and 53.

1.4.2 Streamers

Since minor mergers can create streamers in galaxy halos, the streamers in the Milky Way halo are reviewed. In recent years, the halo of the Milky Way has been found to include streams of stars that in certain cases are traced to the stripping of an infalling dwarf galaxy. The first of these was the discovery of the the Sagittarius dwarf (Ibata et al., 1997) and its tidal streams around the Milky Way (Majewski et al., 2003, and references therein). While other stellar streams originating from other sources have been detected, the Sagittarius dwarf is the largest contributor of substructure to the halo of the Milky Way.

The interactions of the Large Magellanic Cloud (LMC) and Small Magellanic Cloud (SMC) with the Milky Way have produced two tidal features: the Magellanic Stream and the Magellanic Bridge. The Magellanic Stream is observed to be a pure gas feature (Guhathakurta & Reitzel, 1998), while the Magellanic Bridge is known to have both young stars and HI gas (Putman et al., 2003). Recent work by Harris (2007) has shown that the stellar population of the Magellanic Bridge consists only of young stars with no old stellar population. This means that pure gas with no

stars was pulled out in the interaction that caused the bridge to form. By modelling star formation histories in various fields across the Bridge, he finds that star formation started in the Bridge about 200-300 Myr ago and continued until 40 Myr ago. Stars were also only found in the western part of the Bridge, as would be expected by the HI surface density, which falls below the critical threshold (Kennicutt, 1998a) at that point.

In their survey of the SMC and Bridge area, Bica & Schmitt (1995) find 11 star clusters and 97 stellar associations in the Magellanic Bridge along with 3 possible candidates for forming dwarf galaxies. These 3 tidal dwarf galaxy candidates are clumps of extended objects, two in the Bridge, one in the wing of the SMC.

Recent work using star count maps of M31 have discovered several substructures in the halo of M31. The faintest features have $\mu_V \sim 28 - 31$ mag arcsec^{-2}. While the metallicity and age varies among the different substructures, all metallicities ($[Fe/H] > -0.7$) are higher than present-day satellites in the Local Group ($[Fe/H] < -1.5$). This indicates that such satellites are not likely to be the progenitors of the substructures. Low latitude substructures due to their ages and rotation signature are likely to be from perturbations of the thin disk, not from an accreted satellite. The giant stream has been thought to be linked to inner satellites of M31 such as M32 or NGC 205 due to position on the sky and similar metallicities. However, current models using stellar velocities in the stream provide orbits which do not match this (Ferguson, 2007, and references therein).

No substructures have been detected around M33 to limits reaching similar depth as M31 ($\sim$3 magnitudes below the tip of the RGB) (Barker et al., 2011). If substructures exist around M33, they are at a significantly lower surface brightness than those around M31.

1.5 Star Formation and Environmental Effects

The process of atomic gas turning into molecular gas and then forming stars is a fundamental part of understanding star formation in galaxies. However, the factors that influence this process are numerous, and the exact details are still uncertain. Star formation depends on the local conditions in the gas (e.g., pressure) and the molecular gas column density. Other factors that influence star formation are less understood, such as feedback, shear, and global effects from mergers. The general description of how star formation depends on gas density is the Kennicutt-Schmidt law (Kennicutt, 1998b, and references therein):

$$\Sigma_{SFR}(gas) = 2.5 \times 10^{-4} (\frac{\Sigma_{gas}}{1 M_{\odot} pc^{-2}})^{1.4} [M_{\odot} yr^{-1} kpc^{-2}] \tag{1.6}$$

This uses the surface density of the gas (Σ_{gas}, usually molecular and atomic combined) versus the star formation rate (SFR) surface density, Σ_{SFR} (gas). This equation assumes a Salpeter initial mass function (IMF, Salpeter, 1955) and solar metallicity. This indicates that for a higher gas surface density, there will be a higher SFR surface density. It was initially calibrated for galaxies as a whole (global scales), but also has been compared to HII regions inside galaxies. Determining whether the Kennicutt-Schmidt law holds on local scales and for different galaxy types has been the subject of ample recent work (e.g., Daddi et al., 2010; Bigiel et al., 2008; Boselli et al., 2002; Boquien et al., 2011).

In spiral galaxies, the critical surface density above which a self-gravitating infinitely-thin rotating gas disk is locally unstable to axisymmetric perturbations is,

$$\Sigma_{crit} = \frac{\alpha \sigma \kappa}{\pi G} \tag{1.7}$$

with σ as the velocity dispersion of the gas, κ as the epicyclic frequency and α a constant of order unity (Kennicutt, 1989). However, using this formulation of a star formation threshold is not applicable for tidal debris since they are not rotating like the gas disk of a spiral galaxy.

Blitz & Rosolowsky (2006) find a star formation prescription which is based on pressure determining the amount of the ISM that is molecular. Their work uses observational data of 14 galaxies with a range of masses and metallicities to show that the ratio of atomic to molecular gas is linearly related to the hydrostatic pressure. Their revised prescription reduces to the Kennicutt (1998a) star formation rate at high pressures, but provides a more accurate determination of star formation for low pressure regions such as outer regions of spirals. Their low pressure regime equation, which gives lower results than Kennicutt (1998a), is

$$\Sigma_{SFR} = 0.1\epsilon\Sigma_g(\frac{P_{ext}}{P_0})^{0.92} M_\odot pc^{-2} Gyr^{-1} \tag{1.8}$$

with P_{ext} given by:

$$\frac{P_{ext}}{k} = 272 cm^{-3} K(\frac{\Sigma_g}{M_\odot pc^{-2}})(\frac{\Sigma_s}{M_\odot pc^{-2}})^{0.5} \times (\frac{v_g}{kms^{-1}})(\frac{h_s}{pc})^{-0.5} \tag{1.9}$$

Wallin (1990) suggests a mechanism by which star formation can be triggered in tidal tails. Using a restricted three body simulation with test particles, this work shows that gas can be compressed by factors of two to five in a tail by a) twisting of the tidal tail which produces a traveling density wave and b) passage of gas through orbital caustics which results in an extended compression followed by a short period of rarefaction. This study should be taken with caution as an upper estimate on the level of density enhancements in the tail that can seed star formation. The simulation neglects hydrodynamics, self gravity, and cooling, all of

which can be expected to drive compression into the nonlinear regime during self-collision of gas within a caustic or density wave.

To determine the star formation efficiency (SFE), or how efficient a system is at turning its gas into stars, two main but related, methods are used: comparison to the Kennicutt-Schmidt Law and the gas depletion timescale. An estimate of the SFE of a system can be done by comparing the SFR per area measured via a tracer such as Hα emission, far ultraviolet emission, or the far infrared luminosity to the gas density per area. These quantities are the ones used in the Kennicutt-Schmidt relation. If a particular system (e.g., an HII region or an entire galaxy) falls above the Kennicutt-Schmidt law for normal spiral galaxies, it is said to have high SFE whereas if it falls below the line, it has a low SFE. The gas depletion timescale is τ_{dep} =M$_{gas}$/SFR and can be calculated for molecular, atomic, or the total gas mass. One way to think about gas depletion timescales is that τ_{dep} of 0.1, 1, and 10 Gyr correspond to the SFR needed to consume 1%, 10%, and 100% of the gas reservoir in 100 Myr. If $\tau_{dep} > 10$ Gyr, then the system has a low SFE (Bigiel et al., 2008). A typical normal spiral galaxy has $\tau_{dep} \sim 2$ Gyr (Kennicutt, 1998b) indicating that τ_{dep} in the range around 1 Gyr corresponds to a normal SFE. For $\tau_{dep} < 0.7$ Gyr, this corresponds to high SFE (Boquien et al., 2011).

1.5.1 Star Clusters

Star clusters are the place where most stars are formed (Lada & Lada, 2003). By studying the formation and evolution of star clusters, we can determine how the majority of stars in the universe are born and evolve. Young compact star clusters were discovered to be forming in several environments, including starburst galaxies (Meurer et al., 1995), barred galaxies (Barth et al., 1995), some spiral disks (Larsen & Richtler, 1999), the inner regions of mergers (Holtzman et al., 1992; Whitmore et al., 1993; Schweizer et al., 1996; Miller et al., 1997; Whitmore et al., 1999; Zepf

et al., 1999) and in the space between galaxies in compact groups (Gallagher et al., 2001). Finding common characteristics between these environments may allow us to identify the mechanism that causes gas clouds to collapse and efficient star formation to begin (e.g., Jog & Solomon, 1992).

1.5.1.1 Formation

One of the principal mysteries of the tidal debris mode of star formation is the rarity of observed molecular gas. In order to solve it, the star formation efficiency and timescales in molecular clouds need to be understood. If the lifetime of a cloud and its accompanying star formation is short, then the problem is largely resolved. It is also useful to know the star formation efficiency so that there is a gauge of how much gas can be expected in the tails.

The estimation of star formation timescales in the Galaxy has given a large variety of answers depending upon the spatial scales examined. This turns out to be because the the evolution of molecular clouds and cores are set by the local dynamical timescale. For molecular density n, $t_{dyn} \equiv (G\rho)^{-1/2} = 61 n^{-1/2}$ Myr. Each stage of evolution occurs over a few crossing times. In the high density cores where stars are actively forming, the dynamical timescale is of order 1.5 Myr. In the cloud envelope dynamical times may be of order 50 Myr . This has two consequences. When molecular gas is in its diffuse state, which exists at low densities in the low pressure environment of tidal tails, its dynamical time and accompanying evolutionary timescale are long. Once collapse begins, the evolution of the entire cloud is controlled by the dynamical timescale in the densest regions. Dense cluster cores quickly arrive at star forming conditions, and star formation occurs in ~ 3 Myr. At this point the further evolution of the cloud is controlled by the evolutionary timescale of the massive stars which ionize 10-20% or more of the cloud and disperse the rest through winds and supernovae. The dispersed molecular gas

may undergo triggered star formation at another location, but the life of the molecular cloud as a recognizable entity is over. The whole evolution is biased against preserving observable molecular gas. Before star formation starts the gas spends most of its time in a diffuse stage that is less amenable to the formation of CO. Once collapse begins the shortest timescales in the cloud take over driving the evolution, dispersing the cloud in a few Myr when the star forming structures in question are clusters (Elmegreen, 2007).

The second question is the efficiency of star formation in these clouds. The typical star formation efficiency for an OB association is a few percent. For denser clusters this will rise over 10%. Krumholz & Tan (2007) discuss the star formation efficiency per free fall time, ϵ_{ff}. The free fall time is $t_{ff} = (3\pi/32G\rho)^{1/2}$, which is $(3\pi/32)^{1/2} = 0.54$ times the crossing time. An ϵ_{ff} of 1% gives an efficiency of 1.8% for a period of $1.5t_{ff}$, typical of OB associations. In denser regions star formation may persist for a few free fall times before stellar kinetic energy can disperse the cloud, yielding efficiencies of closer to 10%, more typical for a dense star cluster. It is also reasonable to expect ϵ_{ff} to rise slightly with density. Krumholz & McKee (2005) suggest that ϵ_{ff} scales with the cube root of the Mach number, which in turn scales with $\rho^{-1/2}$. This gives $\epsilon_{ff} \propto \rho^{1/6}$ (Elmegreen, 2007). The amount of gas involved in star formation can then be factored in. If the ratio of density in the cloud core to the cloud average is 100, then the ratio of dynamical times is 10. Therefore 90% of the gas is in in its long evolutionary timescale phase. If star formation in a dense core is 10% efficient, the cloud as a whole has a star formation rate of $\sim 1\%$. In a mostly diffuse cloud in the low pressure environment of a tail, the density contrast may be higher, resulting in a lower overall star formation efficiency per burst. Triggered star formation is likely, yielding a few generations of stars, which agrees with the presence of an age spread in tails with a significant number of clusters. In addition, several dense cores may form in any one cloud.

Considering these two factors, the total efficiency over the age of the tail may rise to a few percent.

Using HST/ACS images of NGC 1313 to resolve individual stars, Pellerin et al. (2007) determine that there is a large number of early B-type stars found outside of star clusters and distributed throughout the disk of the galaxy. This means that the star clusters these stars formed within were disrupted within the early B-star lifetimes of 25 Myr, which indicates an infant mortality scenario. In this scenario, the star cluster does not survive beyond when the death of the most massive stars expel gas and dust from the star cluster, removing enough mass for it to become unbound.

1.5.2 Outer Regions of Spirals

The outer regions of spiral galaxies have similar properties to tidal tails. Both of these regions have low gas surface density, low star formation surface density, and tend to lack abundant molecular gas. The spiral galaxy NGC 6946 shows a drop in $\Sigma_{H\alpha}$ of a factor of 100 at $0.8R_{25}$ where R_{25} is the isophotal radius at the limiting surface brightness of 25 mag arcsec^{-2}. This is likely due to the lower covering factor of HII regions at these large radii, not to any change in the intensity of star formation locally (Ferguson, 2007). To see if gravitational instability plays a significant role in determining star formation rates at large radii, Ferguson (2007) plot the $\frac{\Sigma_{gas}}{\Sigma_{crit}}$ versus radius where Σ_{crit} is as in Kennicutt (1989). They discover that the ratio lies within a factor of two of the instability limit $\frac{\Sigma_{gas}}{\Sigma_{crit}} \sim 1$ at all radii. In addition, the radius where the large decline in $\Sigma_{H\alpha}$ happens is not the same as where the instability limit occurs. This indicates that gravitational instability is not ruled out as a cause of star formation at large radii, but it does not exactly match the picture. Since gas disks flare at large radii, there is a large decline in the gas volume density toward galaxy outskirts. This lower density could affect star

formation by lessening the collisions that allow molecular cloud growth or lowering the chance of sustaining a cold neutral medium (Ferguson, 2007). Using high resolution and high sensitivity CO maps of M33, Rosolowsky et al. (2007) find that the amount of molecular gas located within GMCs ($M > 1.3 \times 10^5$ $M_\odot$) declines rapidly at a radius of 4 kpc. Outside that radius, GMCs are nearly absent.

1.6 Contributions of Minor Merger Tidal Debris

The entities formed in minor merger tidal debris could contribute to structures in various environments and to metals in the IGM.

1.6.1 Structures

Various structures can form in minor merger tidal debris including stars, star clusters, and tidal dwarf galaxies. These structures can fall back onto the parent galaxy or escape into the IGM.

Stars formed in the tidal debris of mergers and interactions can escape from the parent galaxy to add to the population of stars between galaxies. Using planetary nebulae surveys, Feldmeier et al. (2004) found that 10-20% of stars in the Virgo and Fornax clusters are located in the intracluster medium. These stars may have formed within galaxies and been stripped by infall into the cluster or interactions with other galaxies. These stars could have also formed in the tidal debris of mergers and interactions.

The small galaxies (or a subset of them) orbiting our Milky Way galaxy could have been formed in tidal debris. Kroupa, Theis, & Boily (2005) show that the distribution of Milky Way satellites is could not have come from a distribution of dark matter dominated satellites. They postulate that the dwarf galaxies originated as TDGs during a minor merger with a gas-rich satellite. The LMC could be a remnant of this satellite, while the smaller dwarf galaxies could have formed in

the tidal tails of this interaction. Previous work by Kroupa (1997) showed that TDGs may evolve to be dwarf spheroidal galaxies, but without dark matter halos.

The TDGs that form in tidal tails may be gravitationally stable and have an orbit such that they last beyond the tidal tail lifetime and become a new galaxy. These can then add to the new galaxy population. The distribution of TDGs around a larger galaxy could be compared with those from predicted hierarchical galaxy formation scenarios. Additionally, TDGs could tell us about the distribution of dark matter in a galaxy. It is thought that there may be little dark matter in the disk of a galaxy. Since TDGs are formed from material originating from a galactic disk, they would likely have little dark matter. Observations of dark matter in TDGs could determine if this model is incorrect, and thus help with studies of cosmology (Duc, Bournaud, & Boquien, 2006).

1.6.2 Enrichment of the IGM

If tidal debris escapes the parent galaxy, any metals formed by new star formation therein can help enrich the IGM. What is the contribution of star clusters formed in tidal debris to the metal density of the IGM? In order to answer this it is necessary to identify the pools of gas that are likely to be enriched by these objects. The sample in this work ranges from isolated mergers to a merger in an Abell cluster, so all components from hot cluster gas to Lyα absorbers must be considered. Figure 1 of Davé & Oppenheimer (2007) summarizes the result of simulations that are in reasonable agreement with observed gas phase metallicities. Halo gas is enriched early, with $\log\langle z/z_{\odot}\rangle$ of -1.6 at redshift $z = 6$, instead of rising to -1 by $z = 0$. Hot shocked IGM rises from -1.8 to -1.5. The change in the diffuse IGM is more striking, increasing from -3 to -1.5. (This includes the damped Lyα systems.) Sub-damped Lyα systems show a stronger evolution rising as high as -0.5 by $z = 0$ Peroux (2007). Metals in low column density systems occur at lower levels. For $N_{HI} > 10^{14}$

cm^{-2} metallicities fall in the range of -3 to -4. Below this column density the metallicity appears to fall off rapidly (Cen et al., 2005).

1.7 This Work

This dissertation uses multiwavelength observations of the tidal debris in minor mergers to determine the star formation rate and star formation efficiency in these environments that may be on the edge of stability.

1.7.1 Sample Selection

A sample of 15 minor mergers were chosen from UGC peculiar galaxies and minor mergers found in the literature. Care was taken to select a sample of well studied galaxies that have known mass ratios (less than ~ 0.3 by the HI mass ratio or via simulations based on HI kinematics) or indications of minor mergers (e.g., disk of spiral galaxy is intact, but tidal debris is apparent in the optical). To have similar mergers across the sample, the large galaxy was chosen to be a spiral galaxy, not a dwarf or Magellanic spiral. The mergers were further cut in luminosity so that the sample has a range of $-21.8 < M_B < -19.5$. The presence of tidal debris indicates that we observed a certain time in the progression of the merger as well, neither too early for tidal debris to be stripped nor too late for the tidal debris to have been accreted onto the massive galaxy or to escape from the system. These minor mergers are separated into three classes based on morphology: early, late, and merged. These stages are also consistent with the dynamical ages of tidal tails. Early mergers are defined as well-separated galaxies displaying tidal interaction (e.g., disturbed morphology, tidal tails and bridges). Late mergers have already completed at least one pass by each other. In this case, the dwarf is still distinguishable from the disk of the large galaxy, though the dwarf may be touching or connected to it. Merged galaxies have only one visible galaxy with no optically

detectable dwarf, but they have significant remaining tidal debris. The sample was further cut in distance so that any star cluster candidates examined would be complete down to at least $M_V < -11$ in order to avoid comparing legitimate star cluster candidates with a population solely comprised of giant HII regions. The tidal debris of sample galaxies was observed in the optical with the 1.8 meter Vatican Advanced Technology Telescope (VATT) on Mt. Graham, Arizona using both broadband filters ($UBVR$) and narrowband Hα. The optical broadband images enable determination of the age, mass, and extinction of populations of star cluster candidates and TDGs in the tidal debris. The Hα images can determine the current rate of star formation over the past 10-20 Myr in the tidal debris. Observations in near infrared broadband filters (H and some JK_s for select tails) were done at the Bok 90-inch on Kitt Peak using the PISCES camera. The near-infrared observations can help determine if there is a population of old stars in the tidal debris, which has implications for the formation mechanism of TDGs.

In order to examine gas properties on local scales of about a few kpc in minor merger tidal debris as related to the star formation therein, a specific suite of multiwavelength observations needed to be available, including atomic and molecular gas. The galaxy NGC 2782 in the above sample had high resolution 21 cm HI observations with the VLA as well as pointed observations of CO(1-0) of various regions in the tidal debris. This enabled determination of atomic and molecular gas masses as well as total gas mass for regions within the tidal debris of NGC 2782. These gas masses could be compared to the SFR from Hα observations to determine the star formation efficiency in tidal debris. NGC 2782 is a late stage merger with two tidal tails which have different gas properties. By comparing how star formation differs between two tails in the same merger, we can gain insight into how gas properties affect star formation. Chapter 2 discusses the SFE of an HII region hosting a young star cluster in the Western tail of NGC 2782. Chapter 3

compares the SFR and SFE between the tidal tails of NGC 2782. The techniques developed by studying NGC 2782 were then applied to UGC 10214 ("The Tadpole") which is also a late stage merger and has atomic and molecular gas observations. The Tadpole also has mid-infrared data from Spitzer to help with star formation and dust determinations.

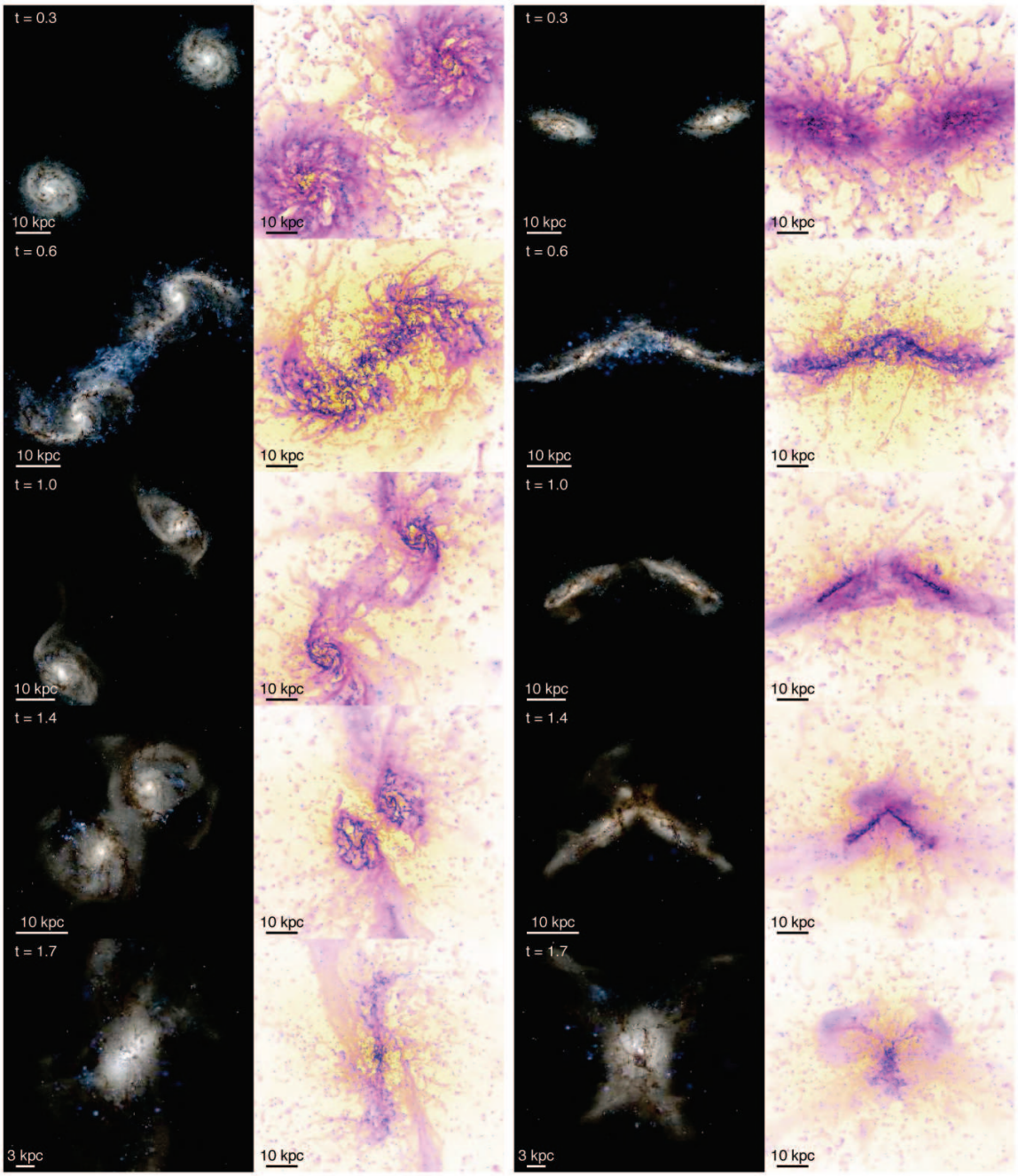

Figure 1.3: Major merger simulation of two equal mass gas rich galaxies from Hopkins et al. (2013). Two perpendicular viewing angles are shown with optical (left) and gas (right) in each pair. The time in Gyr since the beginning of the simulation is labeled in each step.

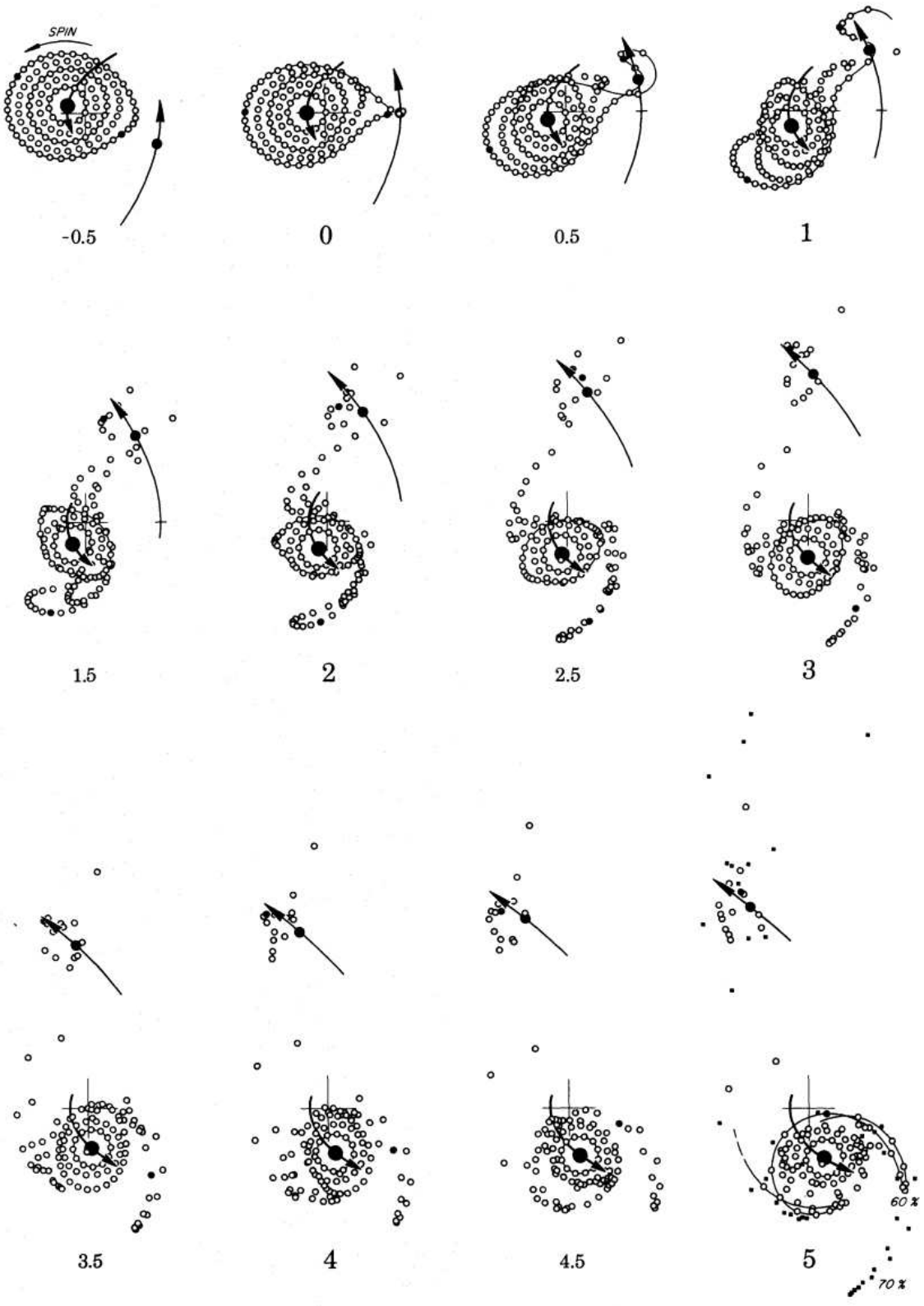

Figure 1.4: Simulation from Toomre & Toomre (1972) of a minor merger with a 1:4 mass ratio showing development of a bridge and tails in a minor merger.

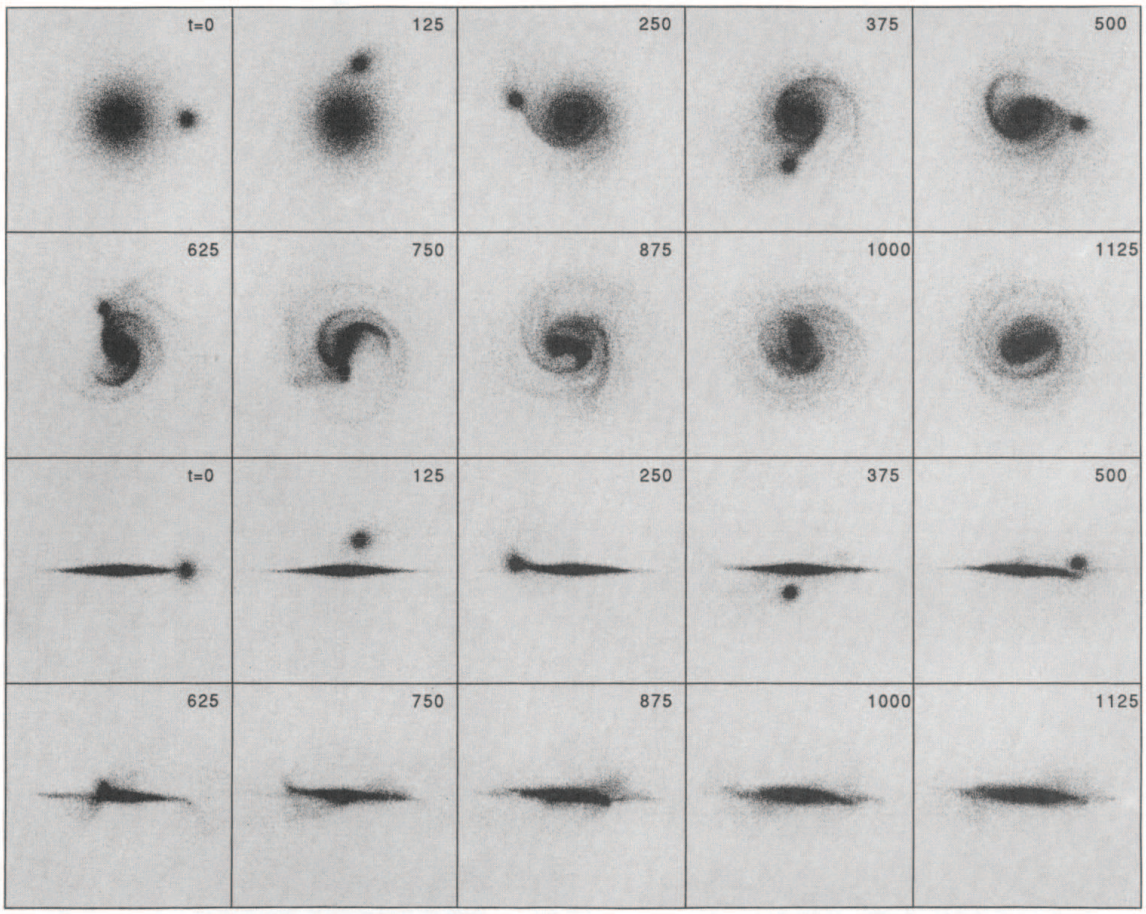

Figure 1.5: Face on and edge on views of a simulation of a minor merger with a mass ratio of 1:10 from Walker, Mihos, & Hernquist (1996). Time steps are shown in intervals of 125 Myr. The spiral is considerably disturbed by merger of the dwarf, thickening and warping the disk.

Chapter 2

STAR FORMATION EFFICIENCY IN THE WESTERN TAIL OF NGC 2782

2.1 Introduction

Major mergers of spiral galaxies are known to create structures such as TDGs and star clusters within their debris (e.g., Duc et al., 2000; Weilbacher et al., 2002; Knierman et al., 2003; Mullan et al., 2011). While examples of major mergers are well known (e.g., NGC 4038/9 "The Antennae"; Whitmore et al., 1999), interactions between equal mass galaxies are relatively rare compared to minor mergers (mass ratios of < 0.3). As part of a larger study, I aim to understand how these frequent encounters shape galactic structure and probe star formation in gas that may be marginally stable. Previous work studied how neutral hydrogen may affect star cluster formation in tidal debris (Maybhate et al., 2007; Mullan et al., 2011), but studies of molecular gas in tidal debris have focused on larger episodes of star formation such as those resulting in the formation of TDGs (Braine et al., 2001). This work examines star formation on smaller scales in the tidal debris of the minor merger NGC 2782.

NGC 2782, a peculiar spiral at a distance of (39.5 ± 2.8) Mpc^2, is undergoing a nuclear starburst (Devereux, 1989). Smith (1994) used a restricted 3-body dynamical model to show that NGC 2782 is the result of a merger of two disk galaxies with a mass ratio of ~ 0.25 occurring ~ 200 Myr ago. It has two tidal tails: an Eastern tail which has a concentration of HI and CO at its base and a gas-poor optically bright knot $2.7'$ from the center; and an HI-rich, optically faint Western tail (Smith, 1994). Mullan et al. (2011) in their V and I band HST/WFPC2 survey of tidal tails find 87 star cluster candidates in the Eastern tail of NGC 2782 and 10 candidates in the Western tail.

Non-detection of CO at the location of HI knots in the Western tail led Braine et al. (2001) to argue that the HI "has presumably not had time to condense into H_2 and for star formation to begin." However, if this tail was pulled from the lower metallicity outer regions of the spiral galaxy like TDGs (Duc et al., 2000) or the merged dwarf galaxy, the lower metallicity may affect the conversion factor between CO and H_2 and result in an underestimated molecular mass. It is possible for H_2 to be present despite CO being undetected. While the blue colors in the Western tail suggest that it formed from the disruption of the dwarf companion, the m_{HI}/L_B ratios suggest that some gas must have originated in NGC 2782's gaseous disk and is therefore mixed composition (Wehner, 2005).

I obtained new Hα observations to determine the star formation efficiency in the Western tail of NGC 2782. Section 2 presents observations, calibration, and results. In Section 3, I discuss global and local star formation in the tail and relate it to star formation in general.

2.2 Observations

Images in UBVR and Hα were taken with the Loral 2K CCD imager at the Lennon 1.8m Vatican Advanced Technology Telescope (VATT) (6.4′ field of view, 0.375″ per pixel). Hα images (6×1200 s) used an 88 mm Andover 3-cavity interference filter (λ_c=6630Å; FWHM=70Å). I observed the tail in Kron-Cousins R (3×300 s) to allow continuum subtraction, following Lee (2006). Images were reduced using standard IRAF[3] tasks. The inset in Figure 2.1 shows the continuum-subtracted Hα image that contained the only Hα emission-line source detected at more than 10σ in the Western tail.

[2]From NED, corrected for Virgo, Great Attractor, and Shapley, which I will use for the duration of this paper. Smith (1994); Braine et al. (2001) use distances of 34 Mpc and 33 Mpc, respectively.

[3]IRAF is distributed by the National Optical Astronomy Observatory, which is operated by AURA, Inc., under contract to the NSF.

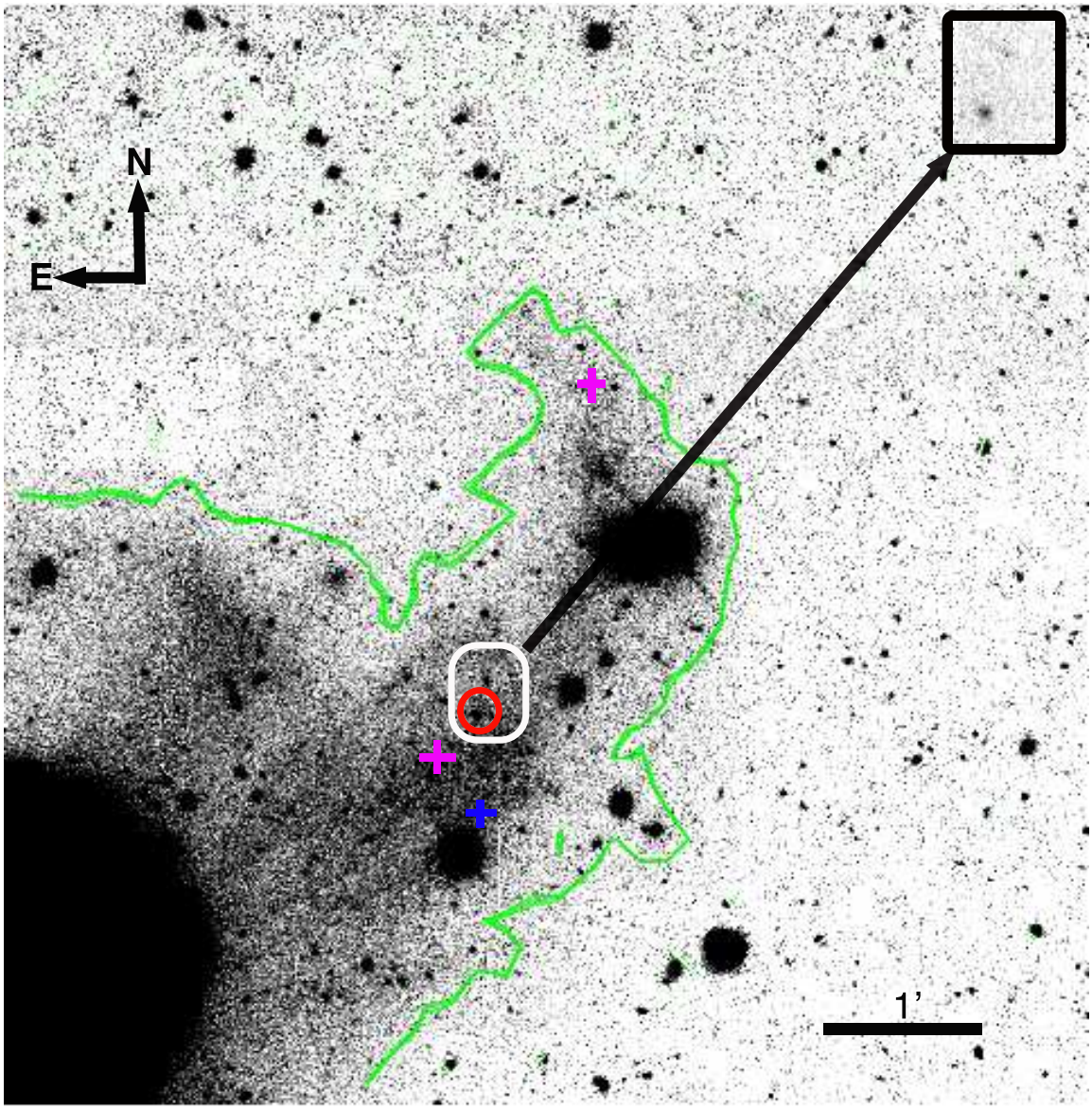

Figure 2.1: V image of Western tail of NGC 2782. The green contour indicates the area defined as the Western Tidal Tail. Red circle marks the location of the Hα source. The crosses mark the locations of massive HI clouds(Smith, 1994). Magenta crosses mark the locations of CO observations from Braine et al. (2001) for the north location and Smith et al. (1999) for the south location. The inset image is the continuum subtracted Hα image of area indicated in the white box.

2.2.1 Hα calibration

I calibrated our Hα images using observations of 3–5 spectrophotometric standard stars from (Oke, 1990). Zero points were obtained by comparing the integral over the filter response function of their spectral energy distribution and the instrumental magnitude from aperture photometry. Extinction corrections assumed a standard atmospheric extinction coefficient of 0.08 mag airmass^{-1} (Lee, 2006). The dispersion of the zero points from individual standard stars was typically 0.02 mag.

Following Lee (2006), I removed the contribution to the Hα flux of the [NII] doublet (λ6548,6583) and emission line flux from the R filter. I used an empirical relation between metallicity and the [N II]/Hα ratio from Figure 9 of van Zee et al. (1998). For a metallicity of 0.4Z$_\odot$, $12 + \log(O/H) = 8.06$ gives $\log([\mathrm{N\,II}]/\mathrm{H}\alpha) = -1.3$, from which follows the Hα flux.

2.2.2 Results

The Hα observations yielded a detection of one source in the Western tail centered on α = 9:13:51.2, δ =+40:08:07 (see Figure 2.1) with $\mathrm{L}_{H\alpha} = (1.9 \pm 0.3) \times 10^{39}$ erg s^{-1}. For comparison, this H II region is fainter than the massive star cluster 30 Dor ($\mathrm{L}_{H\alpha} = 6 \times 10^{39}$ erg s^{-1}), but $>$ 1000 times brighter than Orion with its handful of O-stars ($\mathrm{L}_{H\alpha} = 10^{36}$ erg s^{-1}). It is consistent with the formation of a large star cluster. This H II region has also been detected by Bournaud et al. (2004) and, recently, by Werk et al. (2011). The H II region is located $\sim 20''$ away, but well within the 55″ half power beam size, from the location where Smith et al. (1999) searched for CO(1-0).

2.3 Discussion

I compare SFR per unit area (Σ_{SFR}) from Hα to that expected obtained from the observed gas density using the Kennicutt law, and the SFE in the tail to that seen in other tidal debris, normal galaxies, and starbursts. Σ_{SFR} from Hα for the whole tail is much less than expected given the observed gas density. With only one Hα region in the tail, the derived Σ_{SFR} is a lower limit, as most of the stars forming are late B and A stars based on ultraviolet emission. This indicates that there is a lower star formation efficiency in the tail resulting in the formation of fewer high mass stars. Star formation on the few-kpc scale represents a Σ_{SFR} that is less than expected from the Kennicutt law, using the total gas surface density and the observed Hα. Since the original Kennicutt law was formulated using observations of spiral disks, this indicates that the star formation in the tail is less efficient than in spiral disks. Using the molecular gas depletion time, the SFE of the HII region is similar to the tidal debris regions of Arp 158 and normal galaxies but lower than observed in starburst galaxies. Using only the HI gas as a tracer of the available material, the SFE is higher than seen in the outer disks of spiral galaxies. Given a low SFE from the total gas and a normal SFE from the molecular gas, the observed HII region may be a very small, locally dense region. The lack of observed CO emission could be due to destruction of molecular gas by FUV, effects of beam dilution, the influence of low metallicity on the CO-H_2 conversion factor, or a low pressure gas environment.

The star formation rate from Hα is (Equation 2 in Kennicutt, 1998b): SFR ($M_\odot yr^{-1}$) $= 7.9 \times 10^{-42} L(H\alpha)$ (ergs s^{-1}). The expected SFR from the gas surface density is (Equation 7 in Kennicutt, 1998b):

Table 2.1: Comparison of Star Formation Rates in Western Tail of NGC 2782

Location	Area kpc^2	Hα SFR $M_\odot$ yr^{-1}	$\Sigma_{SFR}(H\alpha)$ $M_\odot$ yr^{-1} kpc^{-2}	$M_{HI}{}^a$ 10^8 $M_\odot$	$M_{mol}{}^b$ 10^8 $M_\odot$	$\Sigma_{gas}{}^c$ $M_\odot$ pc^{-2}	Σ_{SFR}(gas)^d $M_\odot$ yr^{-1} kpc^{-2}
HI-N	8.6	< 0.0003	< 0.00003	0.73	$< 0.086^e$	< 12.9	< 0.006
HI-mid	14.7	0.015(.002)	0.001(0.0002)	1.15	$< 0.16^f$	< 12.2	< 0.005
HI-S	19.3	< 0.0003	< 0.00002	1.16	$< 0.16^f$	< 9.4	< 0.004
W Tail	2300	0.015	0.000009	20	$< 0.4^{e,f}$	< 11.7	< 0.005

[a]Smith (1994), corrected for distance
[b]M_{mol} inferred from CO observations
[c]Includes Helium ($M_{gas} = 1.36(M_{\rm HI} + M_{H_2})$
[d]Kennicutt (1998b) Σ_{gas} includes only HI and H_2
[e]Braine et al. (2001), corrected for distance
[f]Smith et al. (1999), corrected for distance

$$\Sigma_{SFR}(gas) = 2.5 \times 10^{-4} (\frac{\Sigma_{gas}}{1 M_\odot pc^{-2}})^{1.4} M_\odot yr^{-1} kpc^{-2} \quad (2.1)$$

.

Table 2.1 compares the global and local SFR in the Western tail: tail location, area of HI clump or entire tail, Hα SFR with error, SFR per unit area from Hα ($\Sigma_{SFR}(H\alpha)$) with error, mass of HI, mass of molecular gas, total gas surface density, and SFR per unit area from gas density (Σ_{SFR} (gas)).

2.3.1 Star Formation on Global Scales

Using the entire area of Western tail of NGC 2782, the global $\Sigma_{SFR}(\mathrm{H}\alpha) = 9 \times 10^{-6}$ $M_\odot yr^{-1} kpc^{-2}$ is three orders of magnitude below the expected $\Sigma_{SFR}(gas) < 5 \times 10^{-3}$ $M_\odot yr^{-1} kpc^{-2}$. The $\Sigma_{SFR}(\mathrm{H}\alpha)$ is also three orders of magnitude lower than those typical for spiral and dwarf galaxies, but there is a significant dilution factor due to the large area of the tidal tail and low density of stars and gas therein.

The Magellanic Stream is a local example of a gas tail of presumed tidal origin with no star formation. Putman et al. (2003) measured the total HI gas mass in the Stream to be 2.1×10^8 $M_\odot$. By converting the angular size of the Stream

$(100^\circ \times 10^\circ)$ to projected physical size using a distance of 55 kpc (Putman et al., 2003), I infer an area of 940.9 kpc^2. Using the resulting gas surface density of $\Sigma_{\rm HI} = 2.2 \times 10^5$ M$_\odot$kpc^{-2}, the Magellanic Stream has an expected $\Sigma_{SFR} = 3 \times 10^{-5}$ M$_\odot$yr^{-1} kpc^{-2}, two orders of magnitude lower than the Western tail of NGC 2782.

The difference between the Σ_{SFR} values indicates a lower SFE. However, the SFR is a lower limit since there is one HII region and Hα represents star formation in the last 5 Myr. Also the SFR in the tail could be higher than inferred from Hα if it is predominately of a Taurus-Auriga type (Kenyon et al., 2008), producing few star clusters with high mass stars. If so, the color would be blue, but no Hα would be observed. To examine this further, FUV and NUV images of NGC 2782 from the GALEX All-sky Imaging Survey (AIS; Morrissey et al., 2007) were inspected. As seen in Figure 2.2, faint UV emission is detected along the Western tidal tail, indicating the presence of young stellar populations, likely dominated by B and A stars. Since there is no Hα emission (except for the single knot) the star clusters forming along the tail were likely of low mass and had a negligible probability of forming early B and O stars.

2.3.2 Star Formation on Local Scales

I also examine star formation within Western tail HI regions. Smith (1994) measured 10 massive HI clumps with masses from 3×10^7 M$_\odot$ to 1.8×10^8 M$_\odot$. Only three of these HI clumps have star cluster candidates (Mullan et al., 2011). Since only one HII region was found in the Western tail, I use the Hα detection limit as a limit for the high-mass star formation rate for the other two regions. The crosses in Figure 2.1 show the location of these HI clumps with their SFR in Table 2.1.

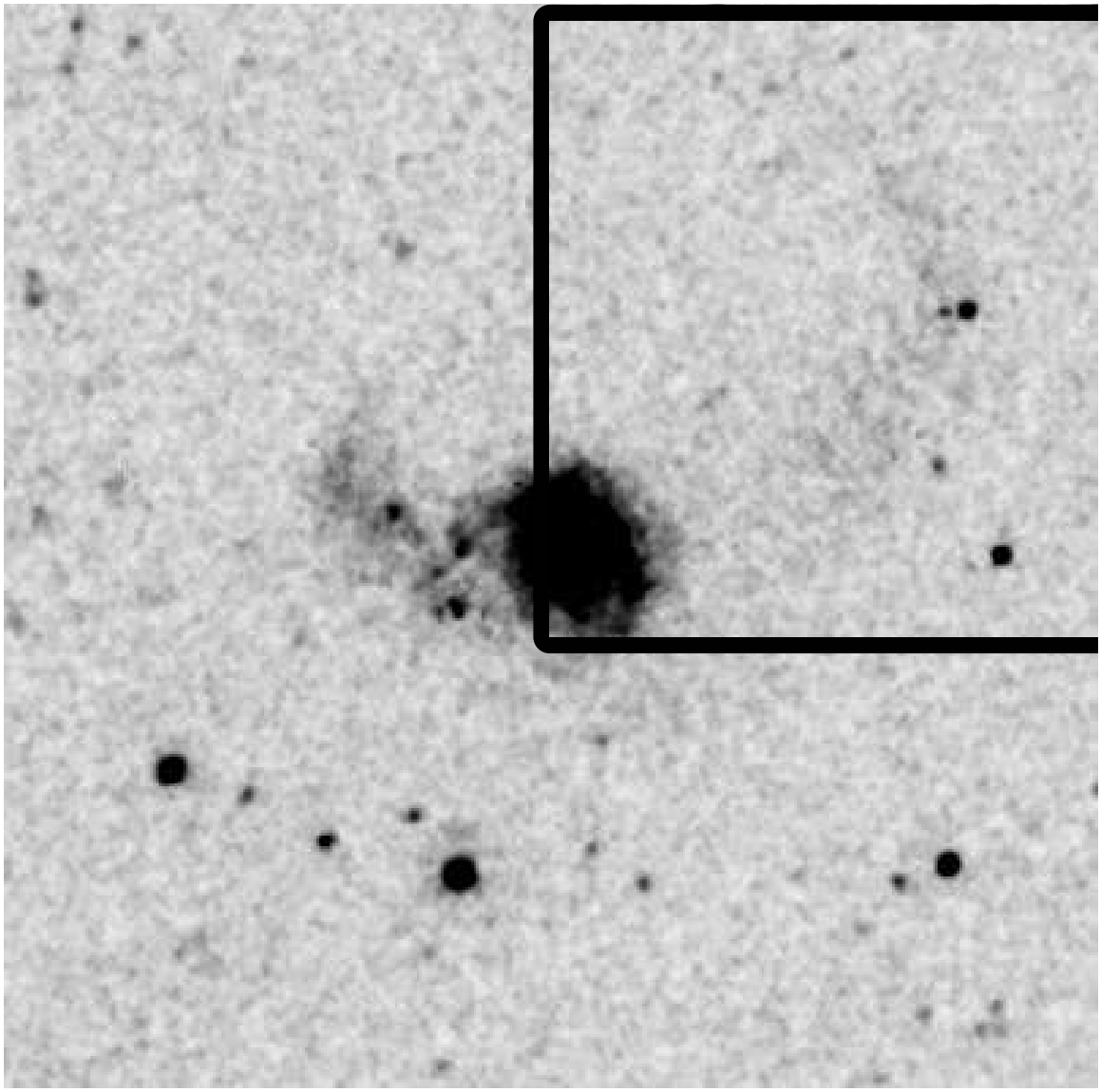

Figure 2.2: Galex composite image of NGC 2782. The box indicates the region covered by the optical image of Figure 2.1

The star formation on few-kpc scales associated with the HII region is lower than expected from the Kennicutt law. Σ_{SFR} calculated from the Hα luminosity is 0.001 ± 0.0002 M$_\odot$ yr^{-1} kpc^{-2}. Due to the non-detection of CO in the Western tail and using a standard CO to H_2 conversion factor, I are only able to establish upper limits to the SFR from the gas density of $\Sigma_{SFR}(gas) < 0.005$ M$_\odot$yr^{-1} kpc^{-2}. While follow-up spectroscopy is necessary to determine the composition of the gas in the

Western tail of NGC 2782, TDGs in major mergers are shown to have $\sim 0.3Z_{\odot}$ (Duc et al., 2000). The standard CO to H_2 conversion factor ($\alpha_{CO1-0} = 4.3$ $M_{\odot}$(K km s^{-1} $pc^2)^{-1}$) is based on observations of the Milky Way. Using galaxies with $z \leq 1$, Genzel et al. (2011) find a linear relation given by $\log \alpha_{CO1-0} = 12.1 - 1.3\mu_0$ where $\mu_0 = 12 + \log(O/H)$. For a metallicity of $0.3Z_{\odot}$ (or $\mu_0 = 8.19$), the appropriate conversion factor is $\alpha_{CO1-0} = 27.5$ $M_{\odot}$(K km s^{-1} $pc^2)^{-1}$ giving a factor of 6 higher molecular mass limit ($M_{mol} \leq 6 \times 10^7$ $M_{\odot}$) than that from the standard conversion factor ($M_{mol} \leq 9 \times 10^6$ $M_{\odot}$). This would then give a larger expected $\Sigma_{SFR}(gas) < 0.01$ $M_{\odot}yr^{-1}$ kpc^{-2} and would give an even larger difference from the measured Hα SFR. Boquien et al. (2011) use multiwavelength data of Arp 158 to study the local Kennicut-Schmidtt law in a merger. They find that star forming regions in the tidal debris follow a different Kennicutt-Schmidt law than those in the central regions of the merger, falling along a line of similar slope to Daddi et al. (2010), but offset so that the same gas density gives lower values of star formation rate. Plotting our HII region in the Western tail of NGC 2782 on Figure 6 of Boquien et al. (2011), I find it to be consistent with quiescent star formation as seen in the tidal debris of Arp 158. This may indicate that star formation in tidal debris is less efficient than that in the central regions of mergers and in normal galaxies.

However, this HII region has a normal SFE using the molecular gas limit. The depletion timescale of the molecular gas is calculated by τ_{dep,H_2} =M_{mol}/SFR. For the HII region in the western tail of NGC 2782, $\tau_{dep} < 1$ Gyr which is comparable to the molecular gas depletion timescales determined for the star forming regions in Arp 158 ($\tau_{dep} \sim 0.5 - 2$ Gyr; Boquien et al., 2011) and in tidal dwarf galaxies ($\tau_{dep} \sim 0.8 - 4$ Gyr; Braine et al., 2001). These ranges are also similar to the average gas depletion timescales in spiral galaxies. The inverse of τ_{dep} is related to the SFE. For the HII region in the western tail of NGC 2782, SFE= $(\tau_{dep})^{-1} > 9.3 \times 10^{-10}$ yr^{-1}. In contrast to the low SFE implied from the total

gas density, this HII region appears to have a similar SFE to the tidal tail regions in Arp 158 and in normal spiral galaxies based on the molecular gas upper limit but lower than dense starburst nuclei (e.g., NE region in Arp 158; Boquien et al., 2011). Bigiel et al. (2010) find very low SFE ($< 9 \times 10^{-11}$ yr^{-1}) in the outer disks of spiral galaxies using FUV and HI observations. The HII region in the western tail of NGC 2782 has a higher SFE than these outer disk regions ($(\tau_{dep,\mathrm{HI}})^{-1} = 1.3 \times 10^{-10}$ yr^{-1}) using only the HI gas mass.

Since there is a low SFE using the total gas density and a normal SFE using the molecular gas limit, this HII region may be very small and dense or something else entirely. Due to the lack of wide-spread massive star formation, using Hα as the star formation indicator likely underestimates the true nature of star formation in the Western tidal tail. This means that our SFE estimates are lower limits, particularly when combined with the upper limit on the molecular gas mass. The discrepancies between the SFE may indicate that there is a denser region of star forming gas that is too small to have been observed. Unlike the very dense regions in the central regions of mergers such as those in the models of Teyssier et al. (2010), there may still be elevated levels of star formation across mergers even out in the tidal debris regions. Star formation in mergers likely depends on local conditions at a scale of 1 kpc, which is the size of the gravitational instabilities in the ISM of mergers and the injection scale of turbulence (Elmegreen, 1993; Elmegreen & Scalo, 2004).

2.3.3 Impact on Star Formation

Tidal tails provide laboratories for star formation under conditions very different from quiescent galaxy disks. With low gas pressures and densities and small amounts of stable molecular gas they are perhaps at the edge of the parameter space open to star formation. The Western tail of NGC 2782 is HI gas rich, but CO

is not observed in the massive HI knots in the tail. This study finds an HII region in the tidal tail indicating recent star formation. Clearly, the lack of observable CO does not guarantee the absence of recent star formation. The presence of a young star cluster in a tail without detectable molecular gas requires one of two situations; either there is no CO, or it escapes detection at the sensitivity of current instrumentation.

If the molecular gas is absent, it may be because it is short-lived. This is most likely the result of a strong ambient FUV radiation field produced by the high local star formation rate. However, the Western tail does not have a high star formation rate, so this is unlikely to cause the lack of observed molecular gas.

The molecular cloud may be too small to be observed. In general H_2 is not directly detectable, so I must rely on surrogate tracers such as CO (Solomon & Vanden Bout, 2005, and references therein). At the distance of NGC 2782 an arcsecond corresponds to a physical scale of 190 pc. This is not an unusual size for molecular clouds in the Galaxy; compact clouds may be smaller still. The IRAM observations of Braine et al. (2001) had a $21''$ half power beam size for their CO(1-0) observations while the Kitt Peak 12m observations of Smith et al. (1999) had a $55''$ half power beam size. If there are only one or a few clouds at the location of their observations, then beam dilution is a major detriment to the detection of CO at the HII region and in the massive HI clouds.

Physics also works against the detection of molecular gas. If the gas is drawn from the dwarf or the outer regions of the large galaxy, it may be deficient in heavy elements. The CO to H_2 conversion factor can be different for lower metallicities, meaning a larger H_2 mass for a given CO flux. Also, CO does not form in a molecular cloud until $A_V \geq 3$, while H_2 forms at $A_V < 1$ (Hollenbach & Tielens, 1997). In a low pressure environment such as low gas density tidal debris a

substantial amount of molecular gas can can exist at low A_V that will not be detectable through CO. Theoretical models (Wolfire, Hollenbach, & McKee, 2010) show that the fraction of molecular mass in the "dark gas" (H_2 and C^+) is $f \sim 0.3$ for typical galactic molecular clouds, increasing for lower A_V and lower metallicity.

2.4 Conclusions

While the molecular gas rich Eastern tail of NGC 2782 was known to form stars, I report the detection of recent star formation in the HI rich but molecular gas poor Western tail. This is contrary to the conclusion of Braine et al. (2001), that the lack of detected molecular gas in the Western tail implies that no stars are forming there. Globally, I find that Σ_{SFR} based on our Hα observations is several orders of magnitude less than expected from the total (HI + H_2) gas density. Hα observations provide only a lower limit on current star formation rates, as GALEX observations show extended FUV+NUV emission along the tail. This indicates star formation is less efficient across the tail, forming lower mass star clusters. I find that the observed local Σ_{SFR} from Hα is $\sim$20% of that expected from the local total gas density, consistent with that observed in the tidal debris of Arp 158. The HII region has a low SFE considering the total gas density, but a normal SFE considering the low molecular gas density. This HII region in the Western tail of NGC 2782 may be a very small, dense region the molecular gas in which is not observable with current instruments or may be indicative of star formation in low metallicity and/or low pressure regimes.

Chapter 3

COMPARING STAR FORMATION IN THE TIDAL TAILS OF NGC 2782

3.1 Introduction

Major mergers (e.g., two equal mass spiral galaxies) can form in their debris ranging from large tidal dwarf galaxies (TDGs) down to star clusters (e.g., Duc et al., 2000; Weilbacher et al., 2002; Knierman et al., 2003; Mullan et al., 2011). However, the spectacular displays of major mergers (e.g., NGC 4038/9 "The Antennae"; Whitmore et al., 1999) are relatively rare compared to minor mergers (in this work, defined to be between a dwarf galaxy and spiral galaxy with a mass ratio of < 0.3). This work aims to understand how minor mergers shape galactic structure and also to examine star formation in gas that may be marginally stable.

Observations of young star clusters in tidal debris show varied results, with some tails forming many star clusters, while others only have a few star clusters scattered along the tail or only hosted in the tidal dwarf galaxy. Studies have shown a large amount of neutral hydrogen in tidal debris (Smith, 1994; Hibbard et al., 1994; Maybhate et al., 2007), but only certain regions with higher gas densities host molecular gas (Smith et al., 1999; Braine et al., 2001). Previous results (Boquien et al., 2011; Knierman et al., 2012) have also shown that star formation in tidal debris does not follow the Kennicutt-Schmidt law. This work[4] aims to compare star formation and gas properties on local and global scales using multiwavelength observations of two tidal tails with different properties in the same minor merger.

The peculiar spiral, NGC 2782, is at a distance of 39.5[5] Mpc (Mould et al., 2000). in the RC3, it is classified as SABa(rs) pec since it has a disturbed center with bright arcs. A starburst is occurring in the central regions (Devereux, 1989).

[4]This work uses the Herschel Space Observatory. Herschel is an ESA space observatory with science instruments provided by European-led Principal Investigator consortia and with important participation from NASA.

NGC 2782 has two tidal tails: an HI-rich, optically faint Western tail extending 5′ to the northwest and an Eastern tail which has a concentration of HI and CO at its base, but a gas-poor optically bright knot 2.7′ from the center (see Smith, 1994). A tidal dwarf galaxy candidate (TDGC) was discovered by Yoshida et al. (1994) in the Eastern tail near the main body of the galaxy. Their optical spectrum confirms its association with NGC 2782 and indicates that it may be metal poor, similar to other TDGs (Duc et al., 2000). CO is not detected at the location of massive HI clumps in the Western tail which led Braine et al. (2001) to suggest that the HI in the Western tail of NGC 2782 is not gravitationally bound and "has presumably not had time to condense into H_2 and for star formation to begin."

To determine the merger age and geometry, Smith (1994) constructed a restricted 3-body dynamical model of NGC 2782. This model reproduces the morphology and HI velocities which indicates that NGC 2782 may be the result of a merger between a large disk galaxy and a lower mass disk galaxy with a mass ratio of ~ 0.25 occurring ~ 200 Myr ago. However, this model does not include gas dynamics or self-gravity of the particles which could change the results. Further simulations have not been done to test this merger scenario. Merger age can also be inferred by using the maximum tail length (50 kpc) and the disk rotation speed (150 km s^{-1}; Smith (1994)) (see Section 3.1 of Knierman et al. (2003)). For NGC 2782, I infer a merger age of 50 kpc/150 km s^{-1} = 300 Myr which is close to the age from Smith (1994).

Wehner (2005) also studied the tidal debris of NGC 2782 with deep, wide-field imaging and found that the debris in the Eastern and Western plumes has colors both consistent with each other and bluer than the main disk of NGC 2782, suggesting that perhaps the two tails formed from the same dwarf companion that

[5]From NED, corrected for Virgo, Great Attractor, and Shapley, which I will use for the duration of this paper.

passed through or along the disk of NGC 2782 and was destroyed in the process. However, by examining the m_{HI}/L_B ratios for the stellar and gaseous debris, Wehner (2005) concludes that it is unlikely that all the gaseous debris in the Western plume originated in the smaller companion, as this would require the excessively large m_{HI}/L_B ratio of 6.4. More likely, a significant amount of the gaseous debris originated in the gaseous disk of the main galaxy.

NGC 2782 also has a well-behaved exponential disk at intermediate radii. Smith et al. (1994) find an $R^{1/4}$ profile within the innermost arcminute, and Wehner (2005) finds that the $R^{1/4}$ profile reemerges at higher radii, consistent with the idea that the outer stellar plumes are debris resulting from a minor merger. Mullan et al. (2011) in their V and I band Hubble Space Telescope/WFPC2 survey of tidal tails find 87 star cluster candidates in the Eastern tail of NGC 2782 and 10 candidates in the Western tail.

I obtained deep optical broadband and Hα images combined with new [CII] and CO observations and published HI and CO observations to compare local and global star formation, as determined by several different tracers, between the tidal tails in NGC 2782. Section 2 contains the observations and calibrations. Section 3 presents the results. In Section 4, I discuss the possible reasons for the differences between the tidal tails.

3.2 Observations and Reductions

I examine different tracers of star formation in the tidal tails of NGC 2782. First, I examine both tails for evidence of young star clusters using ground-based $UBVR$ images and HST/WFPC2 images to identify isolated star clusters or star cluster complexes. The HST/WFPC2 images are from the Cycle 16 program 11134 (P.I. K. Knierman) and published in Mullan et al. (2011). Next, I identify young star forming regions using Hα and [CII]. Then I examine the amount of gas available for

star formation through new and published CO observations and previous HI observations.

3.2.1 Optical images

Images in $UBVR$ and Hα were taken with the Loral 2K CCD imager at the Lennon 1.8m Vatican Advanced Technology Telescope (VATT) on Mount Graham, Arizona (see Table 1 for a log of observations and Figures 3.1 and 3.2). This imager has a $6.4'$ field of view with $0.42''$ per pixel. Images were reduced using standard IRAF[6]IRAF is distributed by the National Optical Astronomy Observatory, which is operated by the Association of Universities for Research in Astronomy, Inc., under cooperative agreement with the National Science Foundation. tasks.

3.2.1.1 Source Detection and Photometry

To select sources, IRAF-DAOFIND was used with a threshold of 4σ where σ is the standard deviation of the background. The standard deviation of the background was found by averaging several regions around the image, away from the varying background of the tail. Sources with $S/N > 3.0$ were retained for photometry due to the smoothness of the ground-based imaging.

Aperture photometry was performed on these sources using the PHOT task in the IRAF-APPHOT package. The radii of the object aperture, the inner boundary of the background annulus, and the outer boundary were 8, 13, and 18 pixels, respectively (3.4/5.5/7.6 arcsec). We retained only sources that were detected in all bands ($UBVR$) and with magnitude errors < 0.2. Photometric zero points were obtained using Landolt standard stars taken on photometric nights.

[6]IRAF is distributed by the National Optical Astronomy Observatory, which is operated by the Association of Universities for Research in Astronomy, Inc., under cooperative agreement with the National Science Foundation.

Table 3.1: Optical Observations of NGC 2782

Tail	Date	Filter	Exp. Time sec	Photometric?
Eastern Tail	Feb. 15, 2004	U	12×300	yes
	Feb. 17, 2004	U	3×900	no
	Feb. 15, 2004	B	9×300	yes
	Feb. 17, 2004	V	4×900	no
	May 12, 2005	V	2×300	yes
	Feb. 17, 2004	R	3×900	no
	May 12, 2005	R	2×300	yes
	May 12, 2005	Hα	3×1200	yes
Western Tail	Feb. 18, 2004	U	8×900	no
	May 22, 2004	U	2×600	yes
	Feb. 16, 2004	B	4×900	no
	May 22, 2004	B	2×300	yes
	Feb. 17, 2004	V	4×900	no
	May 22, 2004	V	2×300	yes
	Feb. 17, 2004	R	3×900	no
	May 22, 2004	R	2×300	yes
	Oct. 3, 2004	R	3×150	yes
	Oct. 4, 2004	R	2×300	yes
	Oct. 3, 2004	Hα	3×900	yes
	Oct. 4, 2004	Hα	2×1200	yes
	Dec. 6, 2004	Hα	3×900	no

The foreground extinction from the Galaxy was corrected using the A_B values from Schlegel, Finkbeiner, & Davis (1998) and the reddening curve from Mathis (1990).

3.2.1.2 Selection of In Tail and Out of Tail Regions

To obtain a population of background objects I identified "in tail" and "out of tail" regions. Previous studies have used various techniques to determine tail boundaries, including location of the HI contours (Knierman et al., 2003), surface brightness contours at a specific surface brightness (μ) (Schombert et al., 1990), and visual inspection (Bastian et al., 2005b). For this study, a combination of surface brightness and contour plotting methods was used. There are two areas to define for tidal debris: the inner regions of the galaxy must be excluded to prevent

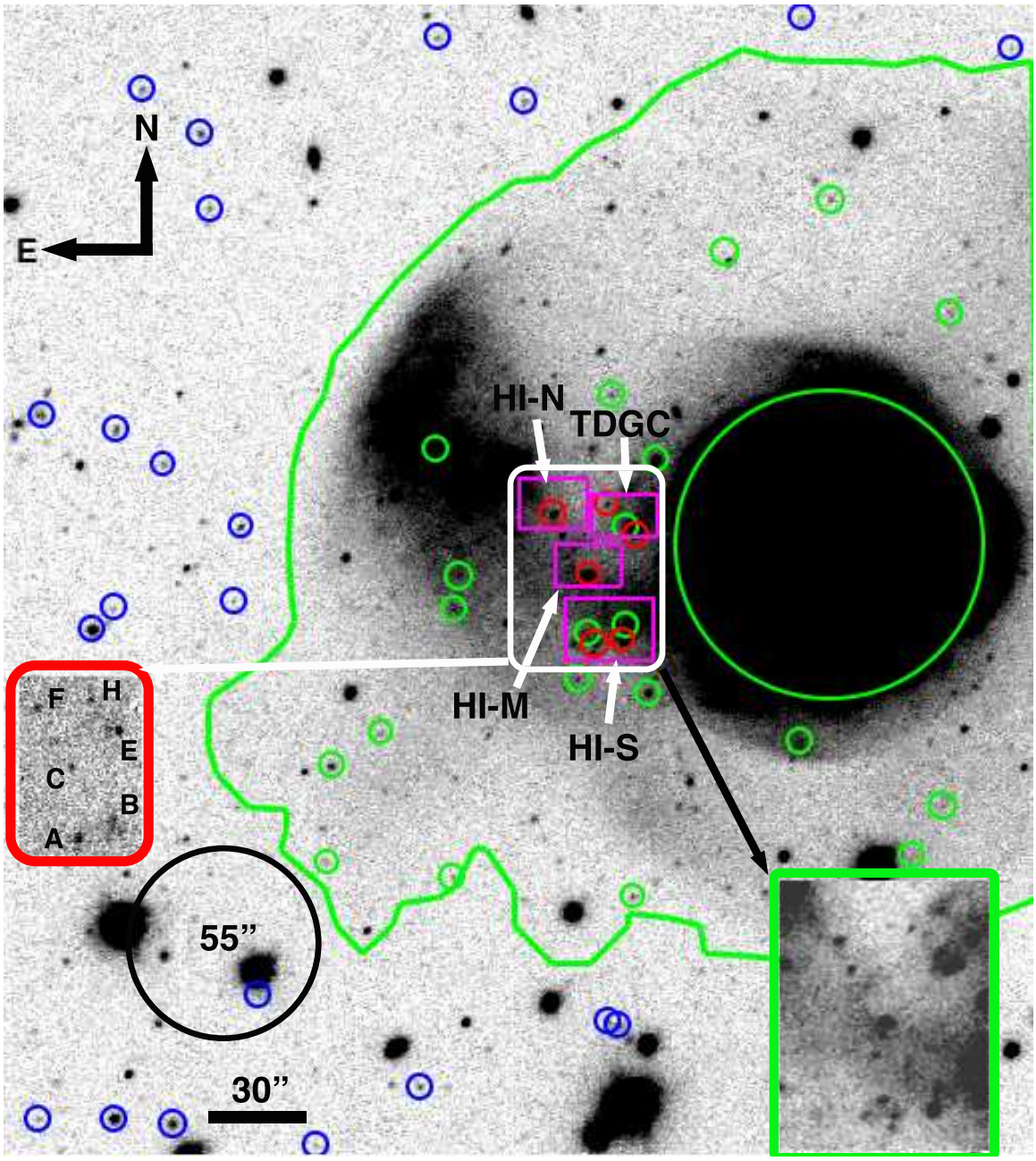

Figure 3.1: V image of Eastern tail taken at the VATT 1.8m with final star cluster candidates marked by small circles. Green indicates “in tail”, while Blue indicates “out of tail”. The large green circle indicates the area defined as the central region of the galaxy. Red circles mark the locations of Hα sources. Magenta boxes mark the locations of massive HI clouds (Smith, 1994). The inset outlined in red shows the Hα emission from the area indicated by the white box. The inset image outlined in green shows an enlargement of the region of the V image indicated by the white box. The black circle indicates the beam size of the CO(1-0) observations with the ARO Kitt Peak 12 meter telescope.

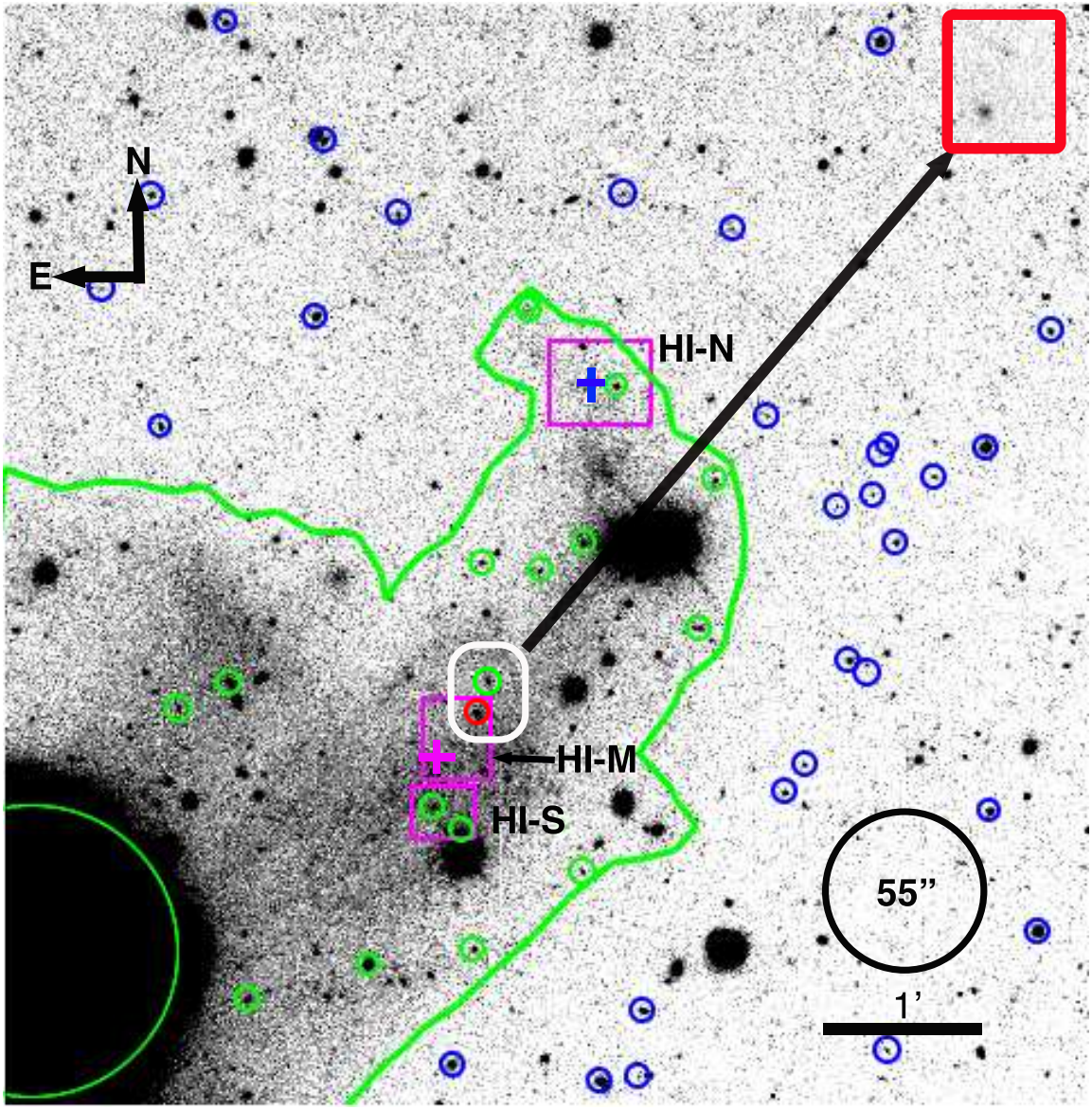

Figure 3.2: V image of Western tail taken at the VATT 1.8m with final star cluster candidates marked by small circles. Green indicates “in tail”, while Blue indicates “out of tail”. The large green circle indicates the area defined as the central region of the galaxy. Red circles mark the location of the Hα source, W235 (Knierman et al., 2012). Magenta boxes mark the locations of massive HI clouds (Smith, 1994). The crosses denote the locations where Smith et al. (1999) looked for CO. The blue cross was reobserved with more sensitive observations by Braine et al. (2001). The inset shows the Hα emission from the area indicated by the white box. The black circle indicates the beam size of the CO(1-0) observations with the ARO Kitt Peak 12 meter telescope.

contamination from star clusters formed in the dense inner starburst, and the outer extent of the debris region where the debris fades into the general sky background.

To determine where the disk of the galaxy ends and the debris begins, I considered the use of the standard D_{25} system or the isophotal diameter at the limiting surface brightness of 25 B mag arcsec^{-2}. The major and minor axes and the position angle of the D_{25} parameters were taken from LEDA[7], and assuming an ellipse, plotted on the image. Next, logarithmically spaced surface brightness contours were plotted on the image to determine where the regularity of the central galaxy region departed into the asymmetry of the debris region. The boundary between the central region of the galaxy and the tidal debris was then defined to be a combination of the D_{25} ellipse and the last regularly shaped contour.

To determine the divide between the debris region and the general background, again, a combination of contour plots and surface brightness limits was used. I first plot the Holmberg radius (Holmberg, 1958), the radius at which the surface brightness in a blue filter reaches 26.5 mag arcsec^{-2}. This contour at $\mu_B = 26.5$ mag arcsec^{-2}, followed not the central regions of this galaxy, but the outer boundary of the tidal tails and debris regions. Holmberg found that the radius at which $\mu_B = 26.5$ mag arcsec^{-2} included the outermost H II or star forming regions in a galaxy, however, recent work shows this to not always be the case (Elmegreen & Hunter, 2004). It is, therefore, not surprising that the Holmberg radius in this merger includes the tidal debris with its star formation. To ensure inclusion of all tidal debris, I plot logarithmically spaced surface brightness contours on the images. At the edges of the tidal debris, there was a rapid decline in surface brightness denoted by the small spacing of several contours followed by 2 surface brightness contours with larger spacing before the tidal debris faded into the background. The outermost contour that enclosed the tail region was chosen to represent the tidal

[7]HyperLeda database (http://leda.univ-lyon1.fr) Paturel et al. (2003)

tail. Upon inspection, this contour followed approximately the Holmberg contour, however, where they differed greatly, the contour chosen by contour spacing was preferred. Figures 3.1 and 3.2 indicate the tidal tail regions selected.

3.2.1.3 Completeness Tests

Completeness tests were conducted on the images in each band. First, a PSF was constructed using 6-10 bright, isolated stars in each image with the PSF task. Then ADDSTAR was used to add 100 stars randomly distributed across the image. Stars were added in 0.5 mag bins spanning the range from 13-26.5 instrumental magnitudes (e.g., an image with 100 stars added with magnitudes between 13 and 13.5, a second image with 100 stars added with magnitudes between 13.5 and 14). Sources were detected and photometry performed as described in Section 3.2.1.1. This procedure was run 50 times per image to produce a total of 5000 stars added randomly to each image. As seen in Figure 3.3, the completeness limit for the Eastern Tail is $V \sim 22.9$ ($M_V \sim -10.1$) and for the Western Tail is $V \sim 23.7$ ($M_V \sim -9.3$). The higher background of the Eastern tail may account for the completeness limit at a brighter magnitude.

3.2.1.4 Final Star Cluster Candidates

To select the final sample of star cluster candidates, I used the 3DEF method (Bik et al., 2003), a three dimensional maximum likelihood code which fits the spectral energy distribution (SED) of a cluster to broad band colors, to fit cluster ages, masses, and extinctions (number of data points = 4, parameters in model = 3). For each cluster, the 3DEF method uses a grid of simple stellar population (SSP) models of ages between 1 Myr and 10 Gyr, extinctions ranging from $0 \leq A_V \leq 4$ in equal steps of 0.02, and masses with a range depending on the absolute magnitude of the source. For this analysis, I adopt the models of Bruzual & Charlot (2003) with a

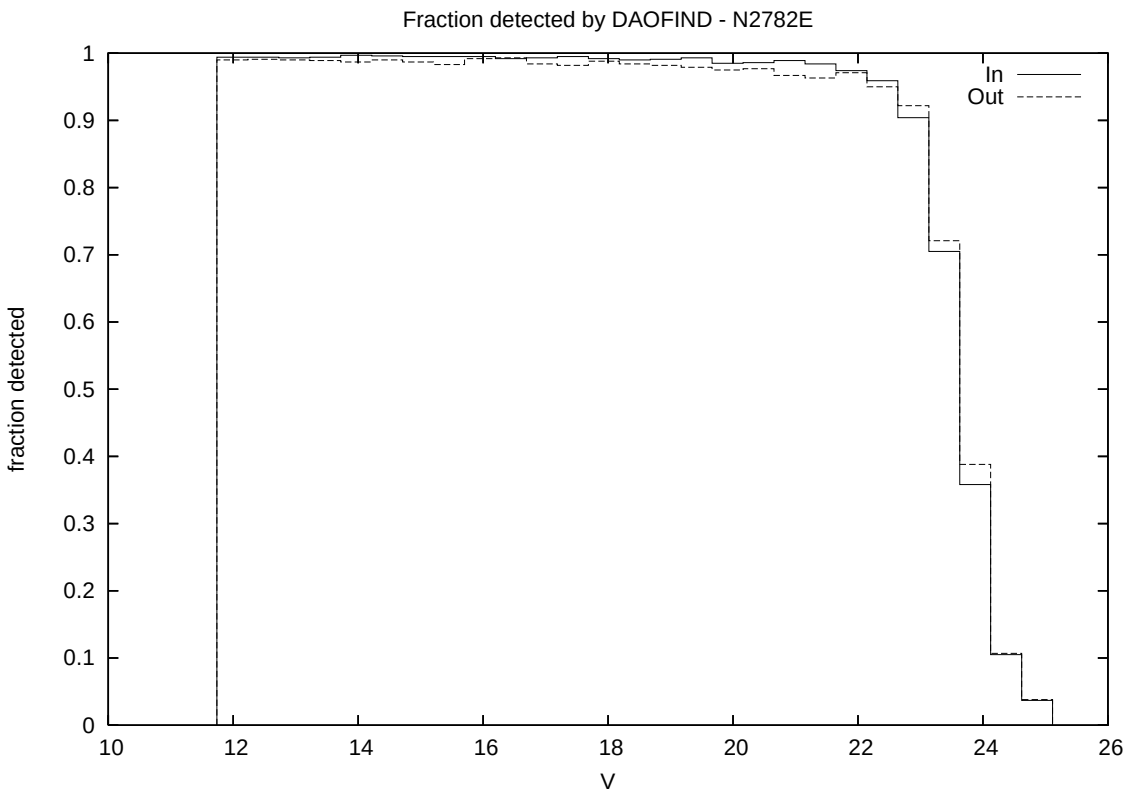

Figure 3.3: For Eastern Tail, the fraction of artificial stars recovered by DAOFIND in the V band.

metallicity of $0.4Z_{\odot}$. I assume that the metallicity of the star clusters in the tidal debris matches the observed metallicity of tidal dwarf galaxies, $Z \sim 1/3Z_{\odot}$ (Duc et al., 2000), which is similar to the metallicity of the outer regions of spiral galaxies. Table 3.2 lists the information for star cluster candidates in the Eastern tail. Tables 3.3 and 3.4 list the information for star cluster candidates in the Western tail. Table 3.3 shows properties of the star clusters such as reduced χ^2, extinction, age, and mass, and their associated errors as well as the centroid pixel values. Table 3.2 and 3.4 show star cluster photometry and errors in $UBVR$, colors, and M_B.

The errors in the magnitudes in each band were used to estimate the errors in the age, mass, and extinction. For each $UBVR$ magnitude, I add the error in the magnitude to the magnitude and run the SED fitting code - the output ages, masses, and extinctions are the upper bound on the error bar for those values. Then

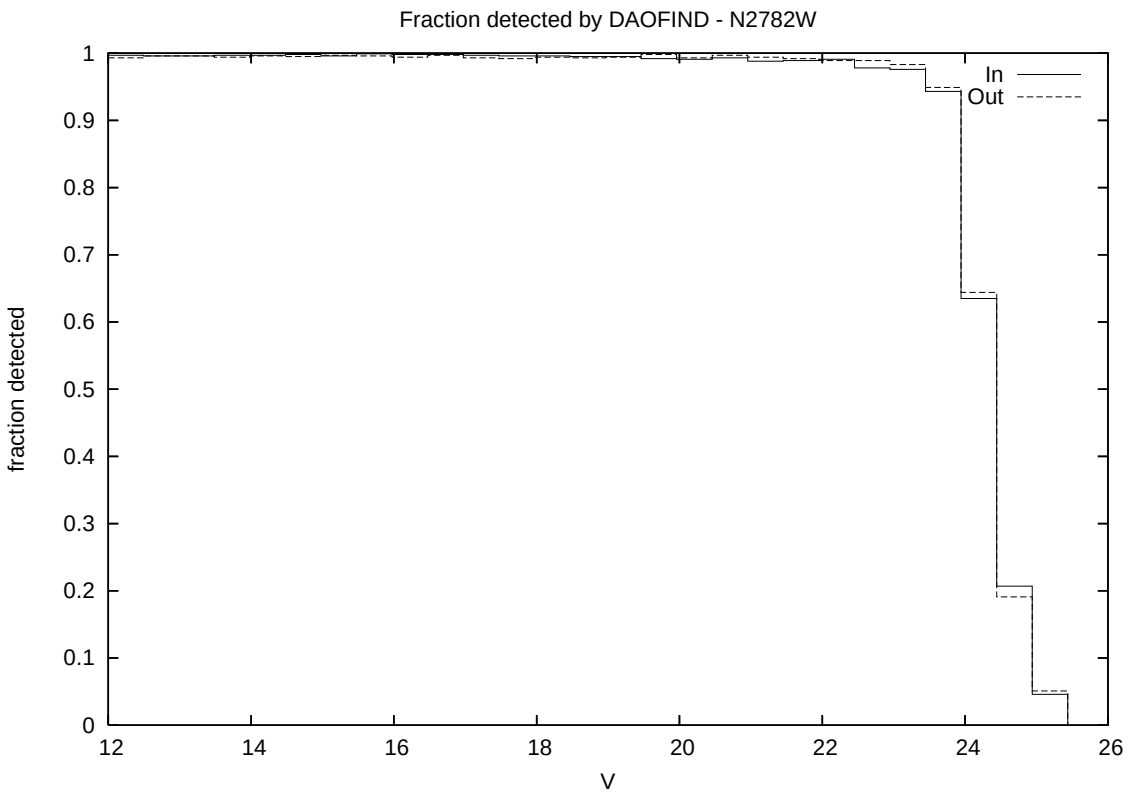

Figure 3.4: For Western Tail, the fraction of artificial stars recovered by DAOFIND in the V band.

I subtract the error in the magnitude from each $UBVR$ magnitude and run the SED fitting code - the output ages, masses, and ext. are the lower bound on the error bar for those values. For bright sources with small error bars, if the output age, mass, or extinction were the same as the data values, the upper and/or lower bounds for the errors were taken from the grid size of the models. For example, a SCC may have an output age of 6.42 with the same age given when I run both "error" models. The next highest age bin is 6.44, so this is assigned to be the upper error and the next lowest age bin, 6.40, will be the lower error. (See the star cluster candidates with their errors in age, mass, and extinction in Table 3.3.)

For the whole Eastern tail image field, out of 153 sources selected in the above method, a total of 55 had reduced $\chi^2 < 3.0$ when fit to the Bruzual & Charlot (2003) single stellar population models with 29 residing in the tail region. For the Western tail image field, out of 113 sources selected in the above method, a total of 49 had reduced $\chi^2 < 3.0$ with 18 in the tail region.

In the "out of tail" regions, 18 were fit in the Eastern tail image and 30 in the Western tail image. These represent our contaminants. Very red sources fit with large extinction are likely to be foreground stars that have similar colors. Others may be background galaxies. To estimate the number of foreground stars in our images, I use the Besacon Milky Way star count model by Robin et al. (2003). For location of NGC 2782 in the sky, the $6'$ field of view, and the range of colors and apparent magnitudes of our SCCs, I estimate there to be about 13 foreground stars. Since the Eastern tail contains about 40% of the field of view, I then expect about 5 foreground stars within the tail and 8 in the "out of tail" region. The Western tail occupies about 30% of the field of view, so I expect about 4 foreground stars in the "in tail" region and 9 in the "out of tail" region. Using the Sloan Digital Sky Survey SkyServer DR6 Search (Adelman-McCarthy et al., 2008) and the Jester et al. (2005) transformations from $UBVR$ to ugr filters, our range of color and magnitudes for the sources in the Eastern and Western tail estimate about 11 background galaxies in the Eastern tail entire field of view and about 18 in the Western tail field of view. The transformation from $UBVR$ to ugr filters is uncertain, so these numbers are only rough estimates for the background galaxies based on color and brightness. In total, I estimate about 19 foreground stars and background galaxies for the Eastern tail (close to the 18 found in the "out of tail" region) and 27 in the Western tail (close to the 30 found "out of tail"). The locations of the final star cluster candidates and the "out of tail" sources fit by the SSP models are marked on the V images in Figures 3.1 and 3.2.

Table 3.2: NGC 2782 East Star Cluster Candidate Photometry

#	X	Y	U	B	V	R	$U-B$	$B-V$	$V-R$	M_B
0	394.152	565.963	21.855 (0.069)	22.343 (0.097)	21.550 (0.087)	21.027 (0.103)	-0.488 (0.119)	0.793 (0.130)	0.522 (0.135)	-10.647
1	360.460	474.580	21.123 (0.039)	20.998 (0.035)	20.772 (0.038)	20.394 (0.070)	0.125 (0.052)	0.226 (0.051)	0.377 (0.080)	-11.992
2	398.524	507.196	21.269 (0.029)	21.282 (0.028)	21.109 (0.055)	20.521 (0.064)	-0.013 (0.041)	0.172 (0.062)	0.588 (0.084)	-11.708
3	429.452	456.452	22.053 (0.058)	22.250 (0.068)	21.736 (0.096)	22.012 (0.265)	-0.197 (0.090)	0.514 (0.118)	-0.276 (0.281)	-10.740
4	383.717	448.772	22.285 (0.085)	22.292 (0.092)	23.056 (0.305)	22.089 (0.303)	-0.007 (0.125)	-0.764 (0.319)	0.967 (0.430)	-10.698
61	196.373	192.751	23.320 (0.195)	22.979 (0.115)	22.529 (0.108)	21.918 (0.116)	0.341 (0.226)	0.450 (0.158)	0.611 (0.159)	-10.011
72	285.484	236.534	23.175 (0.147)	23.057 (0.072)	22.724 (0.118)	21.894 (0.122)	0.118 (0.164)	0.333 (0.138)	0.830 (0.169)	-9.933
86	95.453	288.121	23.745 (0.231)	23.937 (0.163)	22.978 (0.148)	21.661 (0.100)	-0.192 (0.282)	0.959 (0.220)	1.317 (0.179)	-9.053
146	380.222	357.056	23.619 (0.176)	23.474 (0.132)	22.652 (0.132)	22.100 (0.176)	0.146 (0.220)	0.822 (0.187)	0.552 (0.220)	-9.516
233	527.075	402.355	22.547 (0.091)	22.002 (0.057)	21.018 (0.063)	20.286 (0.056)	0.544 (0.108)	0.984 (0.085)	0.732 (0.084)	-10.988
248	343.433	410.918	20.778 (0.022)	20.426 (0.015)	19.831 (0.017)	19.445 (0.025)	0.352 (0.027)	0.595 (0.023)	0.386 (0.031)	-12.564
358	367.965	467.203	21.705 (0.081)	21.590 (0.067)	20.858 (0.048)	20.410 (0.079)	0.115 (0.104)	0.732 (0.082)	0.448 (0.092)	-11.400
451	508.510	508.326	23.259 (0.145)	23.299 (0.117)	22.577 (0.163)	21.743 (0.184)	-0.041 (0.186)	0.723 (0.201)	0.834 (0.246)	-9.691
506	512.762	536.482	23.581 (0.214)	23.424 (0.175)	22.092 (0.144)	21.492 (0.162)	0.158 (0.277)	1.332 (0.226)	0.600 (0.217)	-9.566
530	367.374	549.503	21.755 (0.044)	22.137 (0.059)	21.887 (0.125)	21.191 (0.136)	-0.382 (0.073)	0.250 (0.138)	0.696 (0.185)	-10.853
543	399.654	556.366	22.271 (0.091)	22.348 (0.076)	22.048 (0.129)	21.258 (0.126)	-0.077 (0.119)	0.300 (0.149)	0.790 (0.180)	-10.642
555	370.081	562.678	20.858 (0.028)	20.996 (0.033)	20.579 (0.045)	20.358 (0.080)	-0.138 (0.043)	0.417 (0.056)	0.222 (0.092)	-11.994
596	408.717	595.590	24.289 (0.389)	23.949 (0.184)	22.993 (0.187)	21.622 (0.166)	0.341 (0.430)	0.955 (0.262)	1.371 (0.250)	-9.041
611	349.476	607.032	22.658 (0.078)	22.272 (0.054)	21.382 (0.055)	20.347 (0.054)	0.386 (0.095)	0.891 (0.077)	1.034 (0.077)	-10.718
640	573.743	640.455	23.826 (0.218)	23.435 (0.105)	22.894 (0.133)	22.026 (0.137)	0.392 (0.242)	0.541 (0.170)	0.868 (0.191)	-9.555
650	221.230	646.889	23.340 (0.177)	22.784 (0.094)	21.943 (0.113)	21.266 (0.146)	0.556 (0.201)	0.842 (0.147)	0.676 (0.185)	-10.206
655	614.905	668.400	23.104 (0.122)	22.772 (0.054)	21.566 (0.047)	20.696 (0.040)	0.332 (0.133)	1.206 (0.071)	0.870 (0.061)	-10.218
665	101.749	702.029	23.494 (0.158)	23.433 (0.121)	22.704 (0.123)	21.983 (0.149)	0.061 (0.199)	0.729 (0.172)	0.721 (0.193)	-9.557
682	127.326	743.661	24.429 (0.472)	23.557 (0.159)	22.433 (0.121)	21.004 (0.071)	0.872 (0.498)	1.124 (0.200)	1.428 (0.140)	-9.433
684	619.316	749.198	23.525 (0.184)	23.915 (0.150)	22.963 (0.172)	22.324 (0.169)	-0.390 (0.238)	0.952 (0.228)	0.639 (0.241)	-9.075
690	513.713	761.758	24.085 (0.285)	23.810 (0.154)	22.902 (0.128)	22.095 (0.126)	0.275 (0.324)	0.907 (0.200)	0.807 (0.179)	-9.180
695	362.009	777.885	22.894 (0.099)	22.835 (0.059)	22.276 (0.075)	22.125 (0.125)	0.060 (0.115)	0.558 (0.095)	0.151 (0.145)	-10.155

Table 3.3: NGC 2782 West Star Cluster Candidate Properties

Number	χ^2	Extinction $E(B-V)$	Age log(yr)	Mass $\log(M/M_\odot)$	X pixel	Y pixel
97	0.1	$0.50^{0.49}_{0.51}$	$7.58^{7.54}_{7.63}$	$5.67^{5.68}_{5.66}$	501.704	266.439
101	0.6	$0.27^{0.26}_{0.21}$	$8.06^{8.01}_{8.21}$	$5.73^{5.75}_{5.70}$	498.146	270.219
120	0.0	$0.63^{0.61}_{0.64}$	$7.76^{7.70}_{7.81}$	$6.15^{6.10}_{6.16}$	421.899	338.391
152	2.5	$0.97^{0.96}_{0.98}$	$6.40^{6.38}_{6.42}$	$5.96^{5.97}_{5.95}$	334.414	421.170
172	1.3	$0.00^{0.00}_{0.01}$	$8.46^{8.51}_{8.40}$	$5.74^{5.82}_{5.70}$	451.681	477.299
182	0.2	$0.99^{0.98}_{1.01}$	$6.44^{6.40}_{6.46}$	$5.75^{5.82}_{5.74}$	541.170	494.540
185	0.7	$1.21^{1.18}_{1.25}$	$6.34^{6.32}_{6.36}$	$6.06^{6.07}_{6.05}$	489.818	501.482
204	0.0	$1.42^{1.38}_{1.46}$	$6.34^{6.36}_{6.26}$	$6.57^{6.55}_{6.65}$	348.104	552.657
226	0.5	$0.01^{0.03}_{0.00}$	$7.53^{7.49}_{7.54}$	$5.05^{5.07}_{5.01}$	536.171	599.457
227	0.9	$0.26^{0.82}_{0.28}$	$9.30^{7.86}_{9.32}$	$7.06^{6.70}_{7.08}$	764.120	600.468
234	0.0	$0.94^{0.92}_{0.96}$	$6.40^{6.42}_{6.32}$	$5.66^{5.67}_{5.76}$	810.621	623.717
235	0.6	$0.57^{0.58}_{0.64}$	$6.58^{6.60}_{6.22}$	$5.35^{5.39}_{5.80}$	545.504	626.576
282	0.0	$0.17^{0.20}_{0.15}$	$7.86^{7.76}_{7.91}$	$5.30^{5.34}_{5.25}$	584.557	710.380
299	0.1	$0.78^{0.77}_{0.75}$	$7.91^{7.81}_{8.11}$	$6.56^{6.52}_{6.60}$	558.372	730.295
331	1.2	$0.82^{0.81}_{0.83}$	$6.40^{6.44}_{6.38}$	$5.48^{5.46}_{5.45}$	452.459	767.836
398	2.4	$0.57^{0.55}_{0.52}$	$7.86^{7.72}_{8.11}$	$5.94^{5.88}_{5.97}$	548.341	836.734
412	0.2	$1.21^{1.22}_{1.20}$	$7.32^{7.26}_{7.42}$	$6.98^{6.95}_{7.01}$	641.640	850.058
448	0.6	$0.75^{0.71}_{0.81}$	$6.82^{6.84}_{6.80}$	$5.39^{5.37}_{5.41}$	749.070	880.521

Table 3.4: NGC 2782 West Star Cluster Candidate Photometry

#	U	B	V	R	$U-B$	$B-V$	$V-R$	M_B
97	23.274 (0.134)	23.411 (0.099)	22.814 (0.092)	22.290 (0.079)	-0.136 (0.166)	0.596 (0.135)	0.524 (0.121)	-9.579
101	22.967 (0.102)	23.061 (0.074)	22.610 (0.081)	22.327 (0.078)	-0.094 (0.126)	0.451 (0.109)	0.283 (0.112)	-9.929
120	23.076 (0.111)	23.016 (0.065)	22.330 (0.072)	21.690 (0.051)	0.060 (0.129)	0.686 (0.097)	0.640 (0.088)	-9.974
152	22.503 (0.080)	22.978 (0.065)	22.375 (0.067)	21.569 (0.046)	-0.475 (0.103)	0.603 (0.093)	0.806 (0.081)	-10.012
172	22.635 (0.085)	22.573 (0.061)	22.369 (0.104)	22.307 (0.140)	0.062 (0.105)	0.204 (0.120)	0.063 (0.174)	-10.417
182	23.058 (0.120)	23.488 (0.108)	22.739 (0.098)	22.066 (0.075)	-0.430 (0.161)	0.749 (0.145)	0.673 (0.123)	-9.502
185	23.621 (0.168)	23.832 (0.153)	23.045 (0.120)	22.063 (0.082)	-0.211 (0.227)	0.787 (0.195)	0.983 (0.145)	-9.158
204	23.398 (0.155)	23.429 (0.100)	22.347 (0.082)	21.309 (0.039)	-0.031 (0.184)	1.082 (0.129)	1.037 (0.091)	-9.561
226	22.376 (0.063)	22.841 (0.062)	22.883 (0.113)	22.599 (0.108)	-0.465 (0.088)	-0.042 (0.129)	0.283 (0.156)	-10.149
227	22.917 (0.134)	22.637 (0.042)	21.658 (0.040)	20.944 (0.025)	0.281 (0.140)	0.979 (0.058)	0.714 (0.047)	-10.353
234	23.163 (0.175)	23.585 (0.108)	22.918 (0.135)	22.297 (0.095)	-0.422 (0.206)	0.666 (0.173)	0.621 (0.165)	-9.405
235	21.903 (0.040)	22.492 (0.047)	22.075 (0.059)	21.741 (0.055)	-0.589 (0.062)	0.417 (0.075)	0.334 (0.080)	-10.498
282	23.171 (0.129)	23.404 (0.102)	23.143 (0.148)	22.888 (0.141)	-0.234 (0.165)	0.261 (0.180)	0.255 (0.204)	-9.586
299	23.064 (0.142)	22.793 (0.075)	21.980 (0.083)	21.192 (0.050)	0.270 (0.161)	0.814 (0.112)	0.788 (0.097)	-10.197
331	22.991 (0.112)	23.660 (0.128)	22.999 (0.113)	22.461 (0.095)	-0.669 (0.170)	0.661 (0.171)	0.538 (0.148)	-9.330
398	23.519 (0.184)	23.348 (0.109)	22.990 (0.136)	22.152 (0.085)	0.171 (0.214)	0.358 (0.174)	0.838 (0.161)	-9.642
412	22.849 (0.099)	22.556 (0.046)	21.377 (0.028)	20.245 (0.015)	0.293 (0.109)	1.179 (0.054)	1.132 (0.032)	-10.434
448	23.296 (0.173)	23.358 (0.088)	22.350 (0.063)	21.599 (0.046)	-0.062 (0.194)	1.008 (0.109)	0.751 (0.078)	-9.632

3.2.2 Hα Images

Narrow-band Hα images were also obtained at the VATT with an 88 mm Andover 3-cavity interference filter centered at 6630 Å. The FWHM of the filter is 70Å which includes the [NII] lines. Integration times for the Hα images were 3×1200 s on the Eastern tail and 2×1200 s and 6×900 on the Western tail. To subtract continuum emission, both fields were also observed with a Kron-Cousins R filter using integration times of 3×300 s. Images were reduced in a similar manner as stated above.

To create images with only the emission lines, a scaled R band image was subtracted from narrowband image after alignment using foreground stars. To determine an initial scaling factor, the ratio of integration time for individual frames is multiplied by the ratio of filter widths. If there were still strong continuum features in the galaxies, the scaling factor was varied iteratively until the continuum-dominated regions in the galaxy and the background source and foreground star residuals reached a minimum (Lee, 2006). The insets in Figures 3.1 and 3.2 show the continuum-subtracted Hα images for the regions of interest.

3.2.2.1 Calibration of Hα

Spectrophotometric standard stars from the Oke (1990) catalog were observed on each night. Aperture photometry of these standards was compared to their absolute magnitudes. Absolute magnitudes for each spectrophotometric standard star were calculated by integrating their spectral energy distribution over the filter response function. I used a standard atmospheric extinction coefficient of 0.08 mag airmass^{-1} (Lee, 2006). Zero points were calculated by comparing the absolute magnitude in each filter with the instrumental magnitude from aperture photometry. For each night, the zero points from all standards (typically 3-5) were averaged.

Due to the proximity of the [NII] doublet at λ6548,6583 to the Hα line, their contribution to the flux needs to be accounted for and removed. Also, the use of the broadband R filter for the continuum measurement means that emission line flux from that filter needs to be removed. The total flux equation (Equation A13 in Lee (2006)) is:

$$f_{tot}(H\alpha + [NII]) =$$
$$\lambda^{-2} 10^{-0.4(ZP+2.397-\kappa sec(z))} FWHM_{NB} CR(H\alpha + [NII]) \left[T_{NB}(\lambda) - T_R(\lambda)\frac{t_R}{t_{NB}}\frac{1}{F}\right]^{-1} (3.1)$$

λ: redshifted wavelength of Hα

ZP: zero point

κ: atmospheric extinction coefficient (I use 0.08 mag airmass^{-1})

$FWHM_{NB}$: width of narrowband filter in Å

$CR(H\alpha + [NII])$: count rate in continuum subtracted image

T_R: Transmission correction in R. Calculated by an average of normalized transmissions at each redshifted wavelength of Hα and [NII] lines, weighted by their relative line fluxes.

T_{NB}: Transmission correction for narrowband filter. Calculated by an average of normalized transmissions at each redshifted wavelength of Hα and [NII] lines, weighted by their relative line fluxes.

t_R: exposure time in R band filter

t_{NB}: exposure time in narrowband filter

F: scale factor applied to R band continuum image when subtracting it from narrowband image.

While T_{NB} would ideally be calculated by measuring the line ratios of Hα and [NII] lines directly from spectroscopy, in the absence of spectra for HII regions, there is a relation between metallicity and the ratio of [NII] to Hα. In Figure 9 of

van Zee et al. (1998), an empirical relation is shown between these two values:

$$12 + \log(O/H) = 1.02 \log([NII]/H\alpha) + 9.36 \tag{3.2}$$

For the metallicity of $0.4Z_{\odot}$, as used in the single stellar population models to fit the star cluster candidates, $12 + \log(O/H) = 8.06$ which gives $\log([NII]/H\alpha) = -1.3$. These numbers were also used to subtract the flux of the [NII] lines, giving a resulting flux that contains only that of Hα. If I instead use the value of $12 + \log(O/H) = 8.72$ as measured by Werk et al. (2011) in the Western tail of NGC 2782, I find $\log([NII]/H\alpha) = -0.63$. Using this value to determine our Hα flux, I find that for the Western tail region the difference between the Hα luminosity for the higher metallicity ratio and for the lower metallicity ratio is 0.1×10^{38} erg s^{-1} which is less than the error bar ($\pm 0.4 \times 10^{38}$ erg s^{-1}). I adopt the lower metallicity value for this work.

3.2.3 [CII] observations

To map the [CII] 158μm fine structure line in the tidal tails of NGC 2782, I used the PACS spectrometer (Poglitsch et al., 2010) on the Herschel Space Observatory (Pilbratt et al., 2010). The [CII] 158μm line is observed with the 2nd plus 1st order gratings. I used pointed observations with chopping/nodding and a large throw of 6′ off the source. To increase the line sensitivity, I set the line repetition factor to the maximum value of 10 for each target. To increase the total sensitivity, I repeat each observation cycle 3 times. To reach the needed depth, I observed each pointing for 3.1 hours.

I observed at one location in each tidal tail corresponding to areas of recent star formation as shown by Hα emission indicated in our narrowband images. The PACS array has a total field of view of $47'' \times 47''$ with 5×5 spatial pixels of $9.4''$

size. Each spatial pixel has 16 spectral elements. This size easily encompasses the star forming region in the Western tail of NGC 2782 (Knierman et al., 2012). The Eastern tail of NGC 2782 has a larger spatial extent of star formation; I choose to target only the area with the highest observed CO and HI.

The data were processed using the PACS spectrometer pipeline of the Herschel Interactive Processing Environment (HIPE) Version 7.3.0. The resulting PACS Rebinned Spectral Cube product was exported to a fits cube for further analysis using IDL routines. The [CII] line emission peaks at 159.123 μm for the sources in the Eastern tail. After subtracting a linear baseline, I produced an integrated intensity map (Figure 3.5) by integrating over the wavelength range from 158.997-159.249μm. Contours from 3-10σ are plotted with $\sigma = 0.0028$ Jy μm pix^{-1}. I determine σ by taking the rms of spectra outside the line area, multiplying by the square root of the number of channels integrated for the map (5 in this case), and the width of one channel, 0.063 μm. Spectra (as shown in Figure 3.6) were extracted from a single spaxel from the PACS Rebinned Spectral Cube at the locations indicated in Figure 3.5. After subtracting a linear baseline, the line intensities were summed over the same range as above and multiplied by the bandwidth. Errors in the intensity were calculated from the rms value outside the line area. To correct the amount of flux that falls outside the single spaxel, I use a flux correction of 1/0.5 at 160 μm according to Figure 7 of the PACS Spectroscopy Performance and Calibration Version 2.4 document (Vandenbussche et al., 2011). This aperture correction assumes that the source is a point source lying at the center of the given spaxel.

3.2.4 CO(1-0) observations

The Eastern tail and Western tail of NGC 2782 were observed in the CO(1-0) line in March and October 2012 using the Arizona Radio Observatory Kitt Peak 12 meter

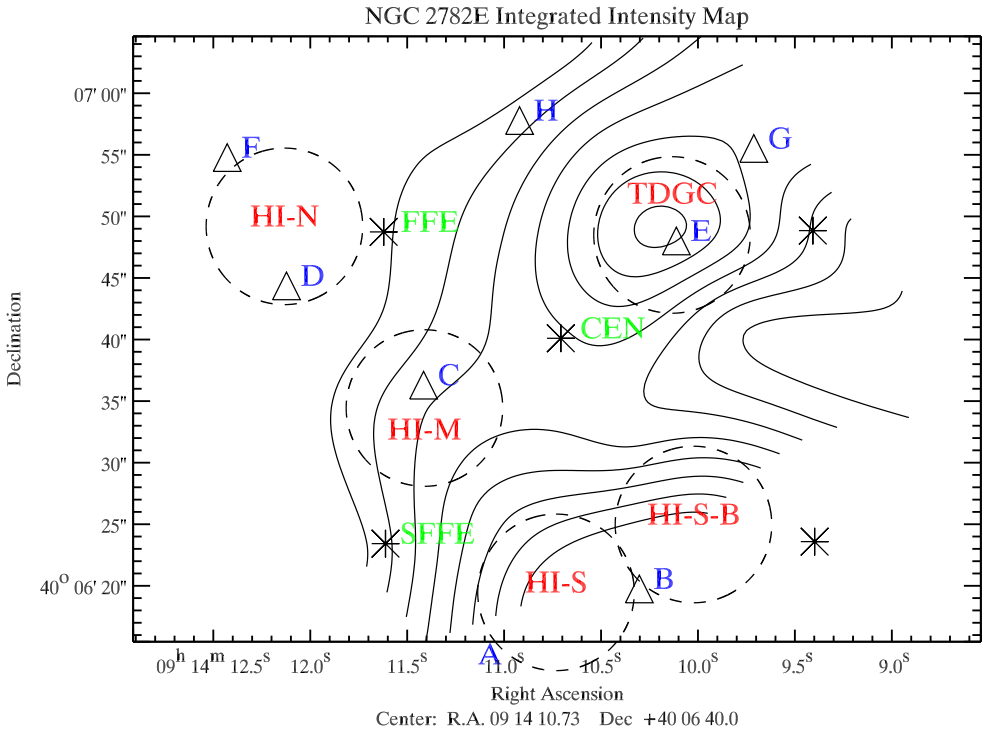

Figure 3.5: Contour of [CII] in Eastern tail of NGC 2782 from Herschel/PACS. Solid contours range from $3-10\sigma$ with $\sigma = 0.0028$ Jy μm pix^{-1}. Circles with red labels indicate position of extracted spectra shown in Figure 3.6. Triangles with blue labels mark the locations of Hα sources found here and also listed in Smith et al. (1999). Asterisks mark the locations where CO(1-0) was looked for with the Kitt Peak 12 meter telescope with the green labeled points indicating locations discussed in the text. The location labeled "CEN" was observed in this work (Figure 3.7) while all other locations were observed by Smith et al. (1999).

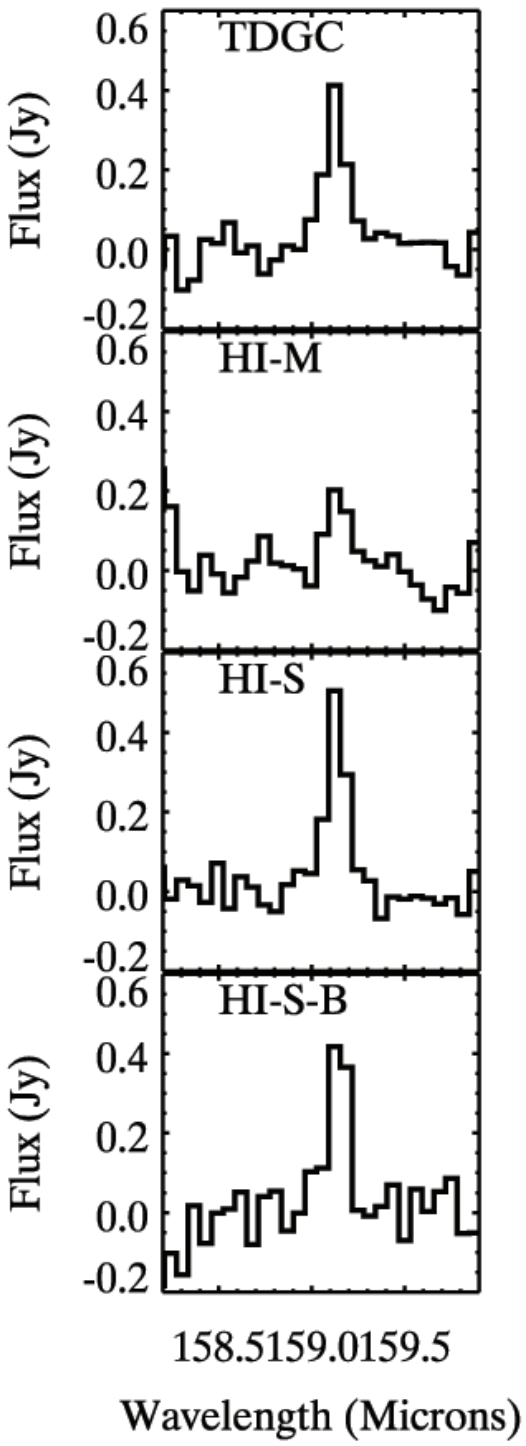

Figure 3.6: Spectra of [CII] extracted at locations in Eastern tail indicated in Figure 3.5.

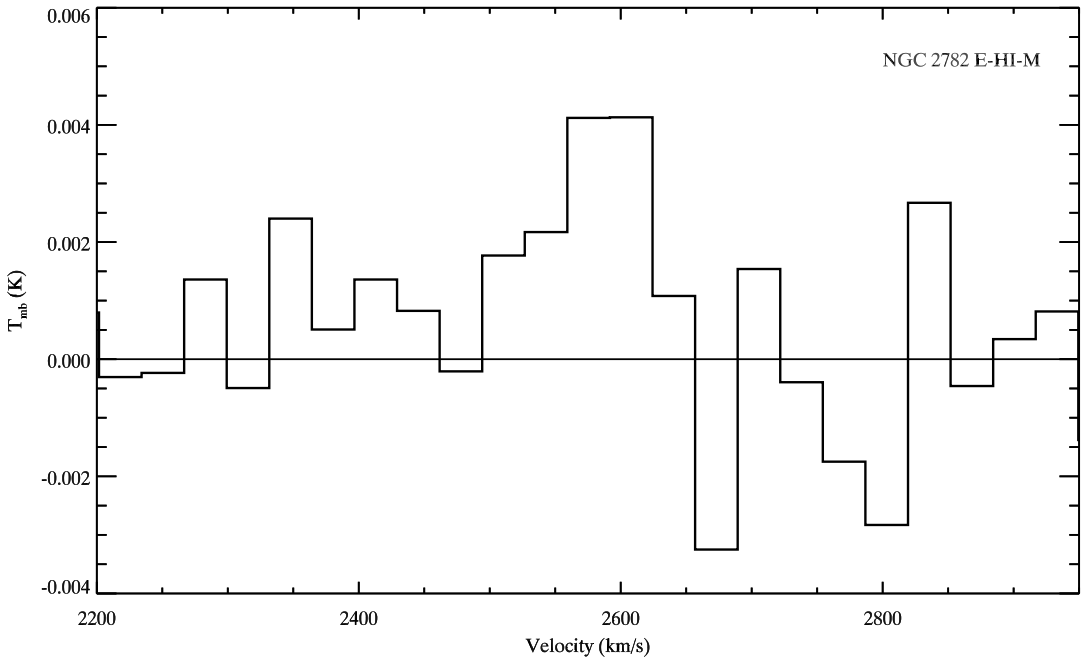

Figure 3.7: Spectra of CO(1-0) in Eastern tail of NGC 2782 from ARO Kitt Peak 12 meter telescope. The location of the observation is the same as the [CII] observation with Herschel.

telescope. I used the ALMA band 3 receiver with 2IFs (both polarizations in USB) using the MAC autocorrelator in 800MHz bandwidth mode with 2048 channels. The total bandpass is 1500 km s^{-1} wide and was centered at 2555 km s^{-1}. I observed in position switch mode with a 10′ throw in azimuth to the off position. The beam size FWHM is 55″ at 115 GHz. The system temperature ranged from 270-360K. I observed at the same locations of recent star formation in the Eastern and Western tails of NGC 2782 as our [CII] observations. For both tails, I reach an rms value of 1 mK which is deeper than the observations of these tails by Smith et al. (1999). The final summed scan for the Eastern tail location is shown in Figure 3.7.

3.3 Results

As seen in previous work (Smith, 1994; Wehner, 2005), the deep optical images presented here show that NGC 2782 has an Eastern tail stretching 20 kpc to the

northeast. This tail consists of a bright region at the tip with a fainter, yet clumpy bridge region between the main body of the spiral and the bright region at the tip of the tail. There is also a fainter extension to the southeast as well as faint debris to the north and south of the main body of the spiral. The Western tail stretches 50 kpc to the northwest. It has a faint yet clumpy structure along its length. There is a single stream stretching the full 50 kpc as well as a smaller extension to the north which only extends one-third as far.

I now examine several different tracers of star formation between the tidal tails: the young star cluster population, HII regions, and the gas properties including neutral, ionized, and molecular gas.

3.3.1 Properties of star clusters in the tidal debris of NGC 2782

The final sample of star cluster candidates include 28 sources in the Eastern tail and 19 sources in the Western tail. As seen in Figure 3.1, the majority (70%) of the star cluster candidates found in the Eastern tail are found in the bridge region. Four candidates are found in the southeast extension while 3 are found in the debris to the north and 3 are found south of the central galaxy. In the Western tail (Figure 3.2), the star cluster candidates are mostly located along the main tail with only 2 in the short tail to the north.

3.3.1.1 Overdensity of star clusters in the tails

While it is difficult to remove further contaminants to the star cluster sample without using additional observations (e.g., spectroscopy), an idea of the amount of star clusters in the tidal tails can be determined statistically by subtracting the background density from the "in tail" sample. This technique was used in Knierman et al. (2003) to determine the overdensity of star clusters in the tidal tails of major mergers. In that paper, young star clusters were selected by using $M_V < -8.5$ and

$V - I < 0.7$ since only one color was available. For this study, I again use $M_V < -8.5$, but since I are unable to match the color cut exactly, I take the Bruzual & Charlot (2003) model age of log(age)=8.5 at which $V - I = 0.7$ as our criteria. Table 3.5 gives the calculation of the overdensity of young star clusters in the tidal debris. Both the Eastern and Western tails have similar values for the overdensity of 0.005-0.006 star clusters per kpc^2. This is much lower than the value of 0.108 kpc^{-2} for the Western tail of major merger NGC 3256. Given the differing areas in the Eastern and Western tails, the expected number of actual star clusters is 14 and 10 respectively. In their HST/WFPC2 survey Mullan et al. (2011), also calculate the overdensity of these tails, but for smaller regions within one WFPC2 pointing. Their values are 0.234 and 0.016 kpc^{-2}, respectively. These values are 39 and 3 times larger than the values measured here. I suspect the difference in areas may have a large affect on this calculation so I calculate the overdensity of our star cluster candidates within area of their WFPC2 observation. I find 9 star cluster candidates within this region of the tail, and only 1 that overlaps in the "out of tail" region. This gives an overdensity of 0.02 ± 0.01 for the Eastern tail, now only a factor of ten lower than the value from Mullan et al. (2011).

3.3.2 Properties of Star Cluster Candidates

As shown in Figure 3.8, more luminous star cluster candidates are found in the Eastern tail than in the Western tail. The ranges of luminosity are $-12.6 < M_B < -9$ for the Eastern tail and $-10.5 < M_B < -9$ for the Western tail. The average M_B for the Eastern tail is -10.34, while the average M_B in the Western tail is -9.85. According to the Kolmogorov-Smirnov test, these distributions of M_B have a probability of $P = 0.019$ of being drawn from the same distribution.

Whitmore et al. (1999) use a faint end cutoff of $M = -9$ since sources fainter than that limit are likely to be bright stars at the distance of the galaxy. The

Table 3.5: Overdensity of star clusters in tails

Tail	Pixel size pc	N_{in}	Area$_{in}$ pix^2	Area$_{in}$ kpc^2	N_{in}/kpc^2	N_{out}	Area$_{out}$ pix^2	Area$_{out}$ kpc^2	N_{out}/kpc^2	Surplus
E	80.69	20	345877	2252.0	0.009(0.002)	9	475199	3094.0	0.003(0.001)	0.006(0.002)
W	80.69	17	257238	1674.9	0.010(0.002)	19	584730	3807.2	0.005(0.001)	0.005(0.003)

brighter end ($M_B = -12$) corresponds to the luminosity of HII regions in Sa/Sb galaxies (Bresolin & Kennicutt, 1997) and to an age of ~ 60 Myr in the Bruzual & Charlot (2003) models for a 10^6 $M_\odot$ star cluster. These star cluster candidates are all much more luminous than the Trapezium cluster in Orion which has $M_B = -4$. The B magnitude for 30 Dor in the Large Magellanic Cloud is $B = 9.63$ which at a distance of 50 kpc gives $M_B = -8.86$. So these star clusters are also more luminous than 30 Dor.

Since the Eastern tail has star cluster candidates with brightnesses similar to HII regions and our ground based observations may hide the extended nature of sources in the tidal tails, I examine the HST/WFPC2 images of both tails from Mullan et al. (2011). As shown in their Figure 3.7 and Figure 3.8, the brighter Eastern tail sources are extended with multiple bright clumps, but the Western tail sources remain compact and isolated. Therefore, our ground based observations of the Western tail sources are able to be treated as single star cluster candidate with one stellar population, particularly since the HST observations are only in F606W and F814W bands. However, I must treat the Eastern tail sources differently due to their extended nature.

Due to the compact and isolated nature of the Western tail sources, I continue with the 3DEF SED fitting method to determine ages, masses, and extinction for this tail. As shown in Figure 3.9, star cluster candidates in the Western tail tails have ages ranging from 2.5 Myr to 1 Gyr. The median age in the Western tail is 150 Myr. This tail has a significant fraction (90%) of star cluster candidates whose ages are less than the age of the merger ~ 200 Myr (log(age[yr]) = 8.3). Therefore, there are star clusters that formed in situ in the Western tidal tail of NGC 2782. Figure 3.9 shows the range of star cluster candidate masses in the Western tail. The Western tail has star cluster candidates ranging in mass from $10^5 - 10^{7.25}$ $M_\odot$, with a median mass of 5×10^5 $M_\odot$. The masses of the star cluster

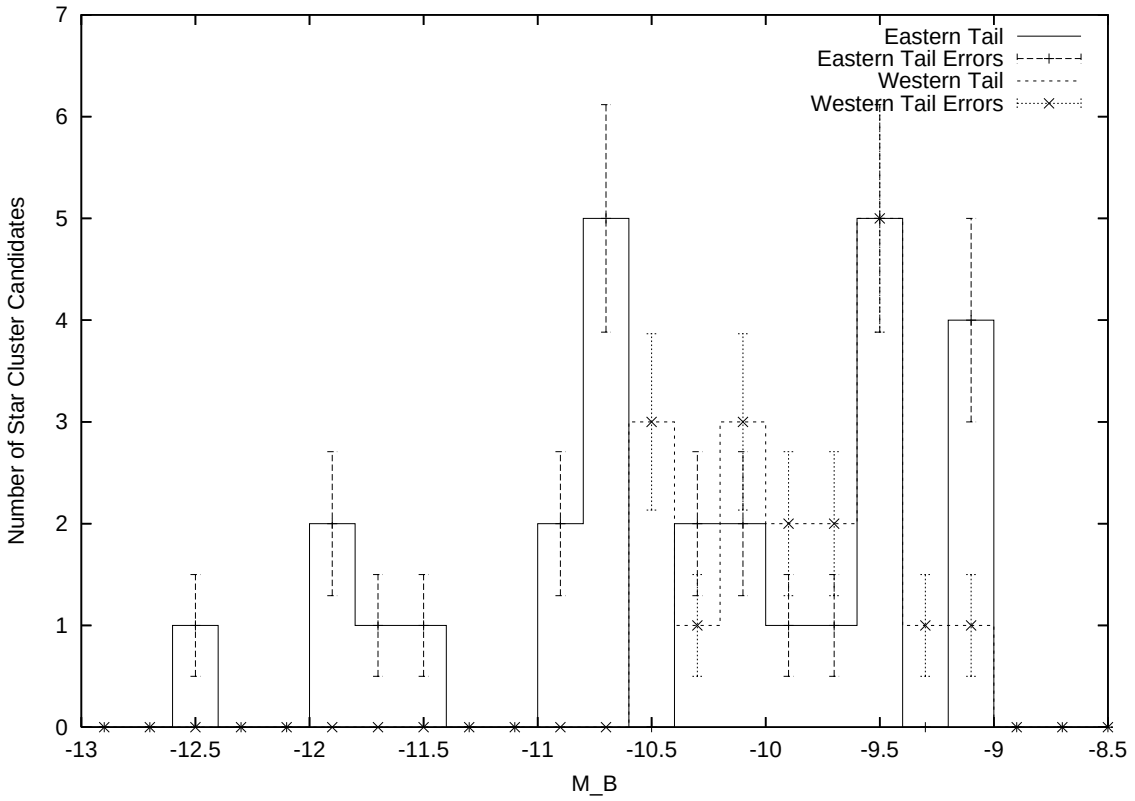

Figure 3.8: Histogram of M_B for final star cluster candidates. The solid line indicates Eastern tail candidates and the dotted line indicates Western tail candidates. Error bars represent the Poisson error for each bin: the square root of the number of star cluster candidates in the bin.

candidates in this tail are much larger than the 10^3 $M_\odot$ of the Orion cluster and the 2×10^4 $M_\odot$ mass of R136, but are on the order of masses of star clusters in central starburst of the Antennae galaxy.

3.3.3 Star Cluster Complexes in Eastern Tail

Stars often form in pairs or clusters, not in isolation, and star clusters may also form in groups. These groups, called star cluster complexes, represent one of the levels of hierarchical star formation in galaxies and are often seen in spiral galaxies. In nearby spiral galaxies, Elmegreen & Salzer (1999) find a linear relation between the brightness of a star cluster complex and its linear size. In optical and molecular observations of M51, Bastian et al. (2005a) find that star cluster complexes are

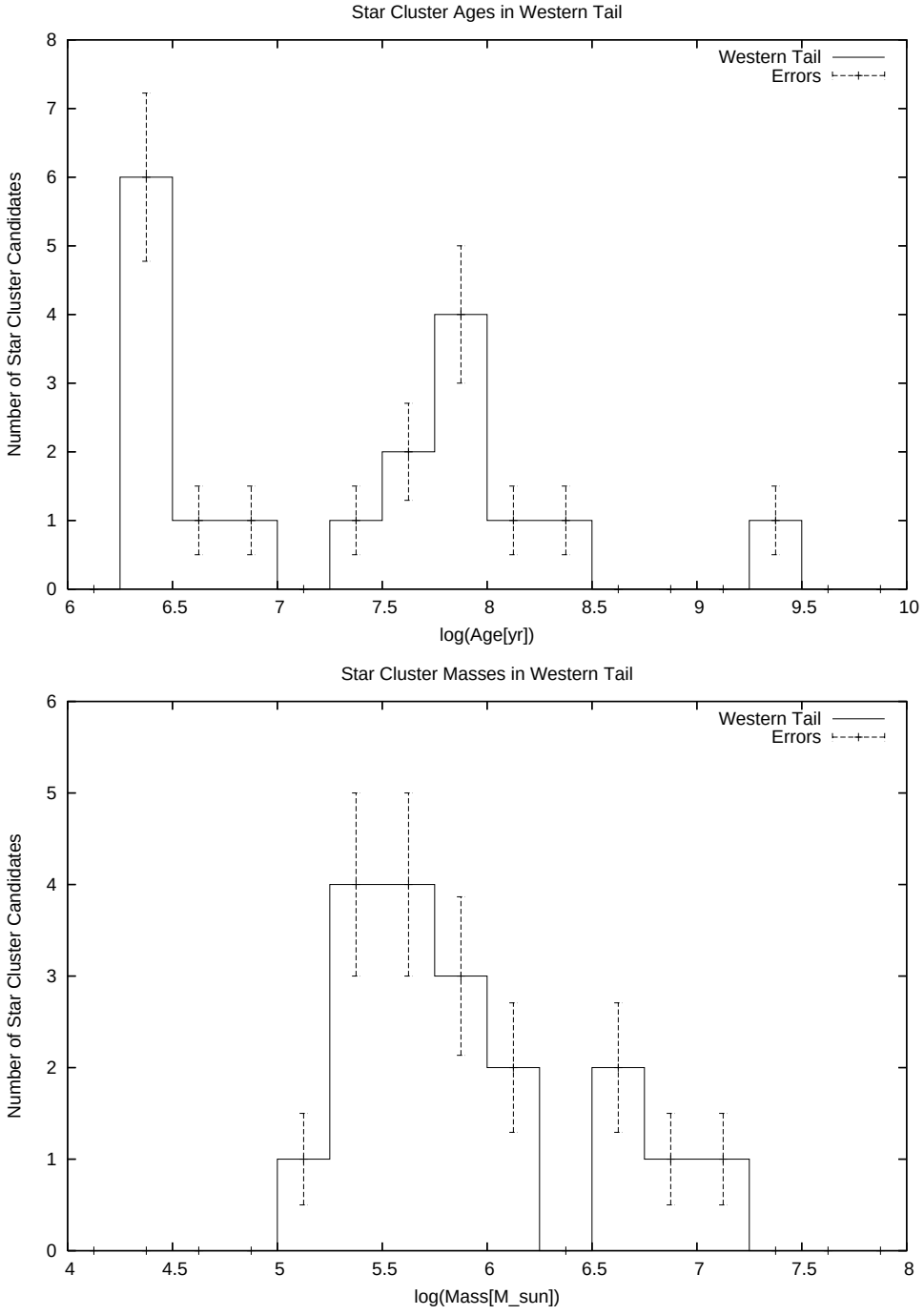

Figure 3.9: Top: Histogram of star cluster candidate ages for the Western tail of NGC 2782. Bottom: Histogram of star cluster candidate masses for the Western tail of NGC 2782. Error bars represent the Poisson error for each bin: the square root of the number of star cluster candidates in the bin.

young (< 10 Myr) and have a strong correlation between mass and size (unlike for isolated star clusters) which is similar to that found for GMCs. In studies of Hickson Compact Group galaxies, Konstantopoulos et al. (2012) find a linear relation in HCG 59, but no relation for HCG 7 (Konstantopoulos et al., 2010).

Using the HST images from Mullan et al. (2011) and the methods of Konstantopoulos et al. (2010, 2012), I find the boundaries of these extended amorphous structures by eye measured by contours which are $> 10\sigma$ above the background (see Figure 3.10). Photometry was performed on the polygonal apertures in the WF3 chip (the only one containing star cluster complexes in our tail region) using IRAF/POLYPHOT, zero points from Dolphin (2009), CTE correction for extended sources (Grogin et al., 2010), and foreground extinction from Schlafly & Finkbeiner (2011) and NED for the HST filters. I find 11 star cluster complexes in the Eastern Tail in the region between the main spiral and the putative dwarf galaxy. The size of each region was determined by taking the square root of the area contained in the polygonal aperture. Since the boundaries of the complexes were determined by eye, I estimate the error to be $\sim 10\%$ of the size of the complex. The sizes of the star cluster complexes ($0.19 < D < 0.63$ kpc) are consistent with sizes of star cluster complexes seen in nearby spiral galaxies (Elmegreen & Salzer, 1999) and in compact groups (Konstantopoulos et al., 2010, 2012). As seen in Figure 3.11, there is a linear relation between size versus luminosity (M_{V606}) for star cluster complexes in the Eastern tail. This indicates a uniform surface brightness for the star cluster complexes in the Eastern tail of NGC 2782. The properties of the star cluster complexes are shown in Table 3.6 which lists: ID number, associated star cluster candidate or HII region ID (if any), centroid pixel values, photometry for F606W and F814W bands and associated errors, $V_{606} - I_{814}$ color, size of the region as calculated above, and $M_{V,606}$. Of the 11 star cluster complexes, I find 6 of these have Hα emission associated with them

indicating ages < 10 Myr. All the complexes have blue color range of $-0.26 < V_{606} - I_{814} < 0.65$ also consistent with previous observations of star cluster complexes with HST (Konstantopoulos et al., 2010, 2012).

3.3.4 HII Regions

The Hα observations yielded a detection of one source in the Western tail (previously published in Knierman et al. (2012); Werk et al. (2011); Bournaud et al. (2004); Torres-Flores et al. (2012) and six sources in the Eastern tail (see Figures 3.1 and 3.2 for location of sources). Previously, Smith et al. (1999) detected nine Hα sources in the Eastern tail. Their observations were deeper than the ones presented here. Our detection limit for the Eastern tail is 7.7×10^{36} erg s^{-1} and for the Western tail is 3.7×10^{37} erg s^{-1}. Table 3.3.4 lists the ID number of the star cluster candidate along with its letter designation from Smith et al. (1999) in the Eastern tail, tail inhabited, B magnitude, M_B magnitude, $U-B$, $B-V$, $V-R$, Hα luminosity, and star formation rate (SFR) from the Hα luminosity following Kennicutt (1998b). One of our most luminous Hα sources, E4, is coincident with the location indicated for the tidal dwarf galaxy candidate in Figure 2 of Yoshida et al. (1994). In the Eastern tail, $L_{\mathrm{H}\alpha} = 1.8 - 7.5 \times 10^{38}$ erg s^{-1}, while the HII region in the Western tail (previously reported in Knierman et al. (2012)) has $L_{\mathrm{H}\alpha} = 19 \times 10^{38}$ erg s^{-1}. The Western tail HII region is listed in Torres-Flores et al. (2012) as System 6 which is the brightest of their young FUV sources in the Western tail. These luminosities are at least an order of magnitude less than those of the brightest HII regions in Sc galaxies ($L_{\mathrm{H}\alpha} \sim 10^{40}$ erg s^{-1}), but are more typical of HII regions in Sa/b galaxies where the brightest ones are $L_{\mathrm{H}\alpha} \sim 10^{39}$ erg s^{-1}. Both tails have HII regions fainter than 30 Dor which has $L_{\mathrm{H}\alpha} = 6 \times 10^{39}$ erg s^{-1}, but brighter than Orion ($L_{\mathrm{H}\alpha} = 10^{36}$ erg s^{-1}). In comparison with the tidal arm region of NGC 3077 (Walter, Martin, & Ott, 2006), this very nearby tidal feature has 36

Table 3.6: Properties of Star Cluster Complexes in the Eastern Tail of NGC 2782

ID	SCCID	X pixel	Y pixel	Area pixel^2	V_{606} mag	I_{814} mag	$V_{606} - I_{814}$ mag	Size kpc	$M_{V_{606}}$ mag
1	E0-A	164.75	637.25	345.5	22.284(0.036)	22.205(0.086)	0.079(0.093)	0.355(0.035)	-10.696(0.154)
2	E1-E	123.90	259.50	1192.0	20.927(0.019)	20.763(0.042)	0.164(0.046)	0.659(0.066)	-12.053(0.151)
3	E2-C	231.50	432.33	833.5	21.279(0.022)	21.057(0.047)	0.222(0.052)	0.551(0.055)	-11.701(0.152)
4	E3-F	399.20	276.60	486.5	22.323(0.043)	22.338(0.114)	-0.015(0.122)	0.421(0.042)	-10.657(0.156)
5	E4-H	240.83	200.50	98.0	23.052(0.041)	23.310(0.128)	-0.259(0.134)	0.189(0.019)	-9.928(0.156)
6	E356	151.27	235.73	1093.0	21.522(0.031)	21.083(0.054)	0.439(0.062)	0.631(0.063)	-11.458(0.153)
7	E530	76.67	547.50	824.5	21.650(0.030)	21.199(0.052)	0.451(0.060)	0.548(0.055)	-11.330(0.153)
8	E543	196.40	610.00	367.0	22.972(0.067)	22.321(0.098)	0.651(0.119)	0.365(0.037)	-10.008(0.164)
9	E555-B	71.67	599.00	869.0	20.979(0.018)	20.610(0.032)	0.369(0.037)	0.562(0.056)	-12.001(0.151)
10		181.40	136.40	224.5	23.019(0.056)	22.571(0.097)	0.449(0.112)	0.286(0.029)	-9.961(0.160)
11		226.75	655.50	392.5	23.207(0.085)	23.169(0.216)	0.038(0.232)	0.378(0.038)	-9.773(0.172)

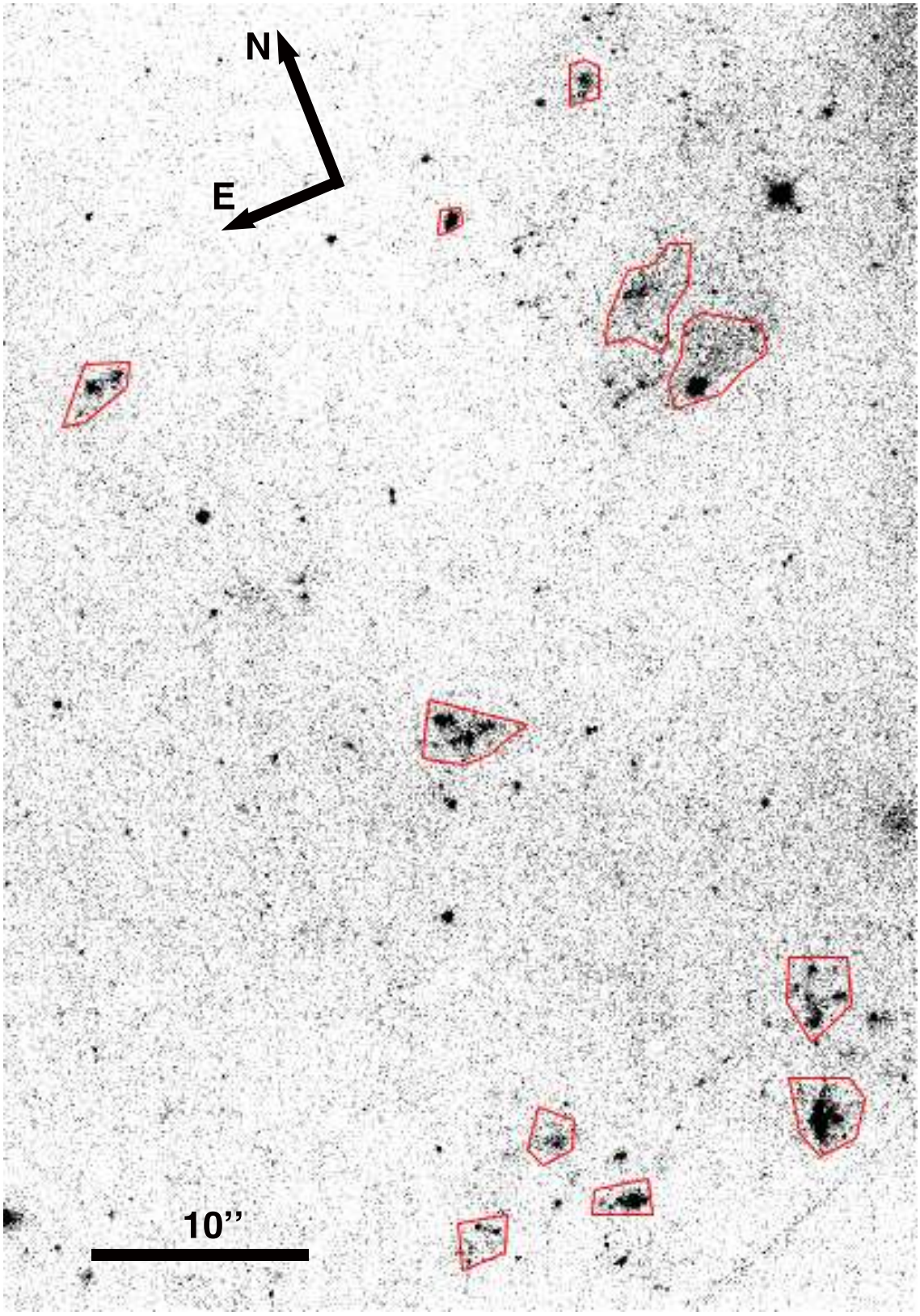

Figure 3.10: Left: HST/WFPC2 image in F606W of the Eastern tail of NGC 2782 from Mullan et al. (2011) with star cluster complexes marked in red. The area displayed here is the same as the inset in Figure 3.1.

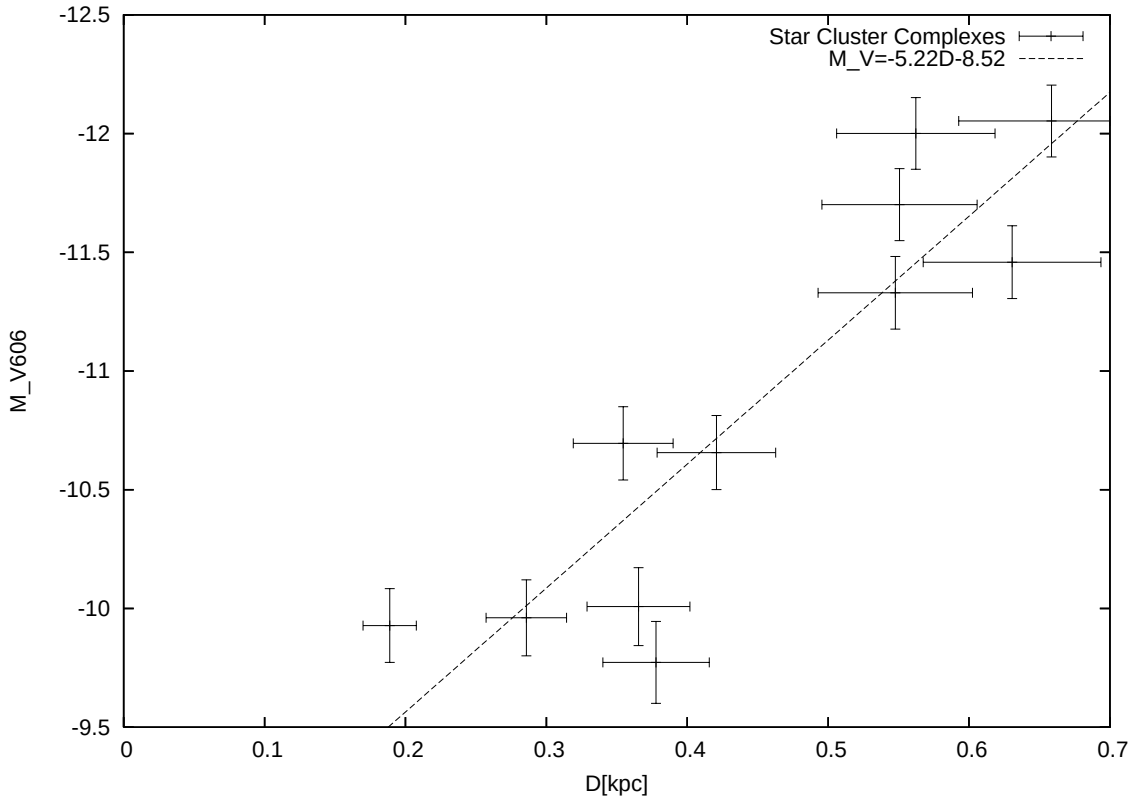

Figure 3.11: Size-luminosity diagram (D-M_{V606}) for star cluster complexes in the Eastern tail of NGC 2782. I find the star cluster complexes to follow a linear size-luminosity relation similar to complexes found in nearby spirals and in HCG 59.

HII regions with a total $L_{\mathrm{H}\alpha} = 2.9 \times 10^{38}$ erg s^{-1} which is similar to E3 and E4 and lower than W235. The Hα region in the Western tail has blue colors and a young age fit with the 3DEF models. Given their Hα emission, these 7 sources are likely to be less than 10 Myr old indicating star formation in situ in both tidal tails.

3.3.5 Comparison to other star cluster populations in tidal debris

In comparing NGC 2782 with the tidal debris of minor merger NGC 6872 (Bastian et al., 2005b), I find that both star cluster systems have similar ages ($\sim 10 - 100$ Myr). However, NGC 6872 has more luminous star clusters ($\langle M_V \rangle = -12.2$) than NGC 2782 ($\langle M_{V,East} \rangle = -11$; $\langle M_{V,West} \rangle = -10$). The difference in star formation can be seen in comparisons of Hα maps of both systems. NGC 6872 has widespread

Table 3.7: Properties of $H\alpha$ sources in Tidal Tails of NGC 2782

Number	Tail	B	M_B	U-B	B-V	V-R	$L_{H\alpha}$	SFR($H\alpha$)
		mag	mag	mag	mag	mag	10^{38}erg s^{-1}	$M_\odot$ yr^{-1}
E0-A[a]	E	20.98	-11.95	-0.49	0.79	0.52	6.5(0.9)	0.0051(0.0008)
E1-E[a]	E	21.57	-11.37	0.12	0.23	0.38	7.5(1.0)	0.0059(0.0009)
E2-C[a]	E	21.17	-11.76	0.01	0.17	0.59	1.8(0.4)	0.0015(0.0003)
E3-F[a]	E	21.60	-11.33	-0.20	0.51	-0.28	2.7(0.5)	0.0022(0.0004)
E4-H[a]	E	21.92	-11.18	-0.01	-0.76	0.97	2.7(0.5)	0.0022(0.0004)
E555-B[a]	E	20.996	-11.994	-0.138	0.417	0.222	6.0(0.9)	0.0047(0.0007)
W235	W	22.492	-10.498	-0.60	0.42	0.33	19(3)	0.015(0.002)

[a]Letter Nomenclature from Smith et al. (1999)

Hα emission along both tails (Mihos et al., 1993) which are correlated with young massive star clusters (Bastian et al., 2005b). On the other hand, NGC 2782 has only a few discrete Hα emission regions in the Eastern tail, and only one in the Western tail. NGC 6872 has a slightly younger age ($\sim$ 145 Myr) than NGC 2782 perhaps accounting for the difference in star formation in the tidal tails. There may also be differences in the progenitor galaxies; these could account for differences in star formation rate of the tidal tails. NGC 2782 is a strongly star forming galaxy while NGC 6872 has little star formation in its central regions. The NGC 6872 interaction likely stripped off gas-rich outer layers of the large spiral galaxy like the Western tail of NGC 2782 while the Eastern tail of NGC 2782 may be remnants of the smaller galaxy. The sample of minor mergers by Ferreiro, Pastoriza, & Rickes (2008) include larger structures detected by Hα emission, leading to younger and more massive structures such as HII regions and Tidal Dwarf Galaxies with very few star clusters detected.

The star clusters in the tidal tails of major merger NGC 3256 (Knierman et al., 2003) have similar ages (30-300 Myr) and luminosities ($\langle M_V \rangle \sim -10$) to those in NGC 2782. Three star clusters in the Western Tail of NGC 3256 were spectroscopically confirmed by Trancho et al. (2007) at Gemini South. From their GMOS-S spectra, they determine ages to be $\sim$ 80 Myr for two star clusters and $\sim$ 200 Myr for the third having approximately solar metallicities. The three star clusters in the Western tail of NGC 3256 have masses ($1 - 2 \times 10^5$ M$_\odot$) which are similar to the average masses of star clusters in the Western tail of NGC 2782. Using the HST/WFPC2 images of the Western tail of NGC 3256, Trancho et al. (2007) show the three star clusters to have a large size ($r_{eff} \sim 10 - 20$ pc) compared to Milky Way globular clusters or other young massive clusters ($r_{eff} \sim 3 - 4$ pc). The large size of the star clusters may mean that the GMC underwent weak compression during the star cluster formation. On the other hand, the tidal tail star

clusters may not have experienced the tidal stripping that other young clusters in the centers of galaxies have.

3.3.6 Comparing Gas Properties of the Tails

I now examine the gas properties of these two tails. Both tails have been previously observed in HI (Smith, 1994) and in CO (Smith et al., 1999; Braine et al., 2001). The Eastern tail is rich in both HI and CO while the Western tail has HI, but no detectable CO. Table 3.3.6 lists the location, area, SFR density (Σ_{SFR}) from [CII], SFR density (Σ_{SFR}) from Hα, mass of HI, molecular gas mass, total gas surface density, and predicted star formation rate density from the gas density from Kennicutt (1998b). This table includes information for the local regions within each tail as well as for the entire tail.

3.3.6.1 Neutral Hydrogen - HI

There are 3 massive HI clumps in both tails which have star cluster candidates associated with them. In the Western tail, Smith (1994) measure 10 massive HI clumps. These range in masses from 3×10^7 M$_\odot$ to 1.8×10^8 M$_\odot$. Only three of these massive HI clumps have star cluster candidates found within their bounds. Since only one HII region was found in the Western tail, I use the Hα background limit as a limit for the Hα star formation rate for the other two HI clumps. The magenta boxes in Figure 3.2 show the location of these three clumps in the Western tail. In the Eastern tail, individual clumps are not tabulated in Smith (1994), but their masses and sizes were determined by inspection of their map of HI contours. I also include a box of the area surrounding the TDGC found by Yoshida et al. (1994) even though it falls outside the HI peaks. The HI clumps in the Eastern tail have masses from $3 - 8 \times 10^8$ M$_\odot$, but only 4×10^7 M$_\odot$ for the location of TDGC. The four regions in the Eastern tail have Hα sources which provide the local Hα

Table 3.8: Comparison of Local & Global Star Formation Rates

Location	ID	Area kpc^2	Σ_{SFR}([CII]) 10^{-3} $M_\odot$ yr^{-1} kpc^{-2}	$\Sigma_{SFR}(H\alpha)$ 10^{-3} $M_\odot$ yr^{-1} kpc^{-2}	M_{HI}[a] 10^8 $M_\odot$	M_{mol}[b] 10^8 $M_\odot$	Σ_{gas}[c] $M_\odot$ pc^{-2}	Σ_{SFR}(gas)[d] 10^{-3} $M_\odot$ yr^{-1} kpc^{-2}
East								
TDGC	E1,E4	7.09	4.5(0.2)	1.1(0.1)	0.4	2.6[f]	44	51
HI-N	E3	11.8	< 0.3	0.27(0.04)	5.2	2.6[f]	82	119
HI-M	E2	7.09	2.5(0.3)	0.22(0.05)	3.1	3.69(0.09)	112	184
HI-S	E0,E555	23.6	2.9(0.1)	0.42(0.03)	8.1	3.8[f]	62	82
E Tail		3000	0.04	0.01	17	8.6	1.1	0.3
West								
HI-N		8.6		< 0.03	0.73	< 0.086[e]	< 12.5	< 9
HI-M	W235	14.7	< 1.1	1.0(0.2)	1.15	< 0.22	< 9.1	< 5
HI-S		19.3		< 0.02	1.16	< 1.5[f]	< 10.1	< 6
W Tail		2300		0.009	19	< 1.8	< 1.6	< 0.5

[a]Smith (1994), corrected for distance
[b]M_{mol} inferred from CO observations
[c]Includes helium ($M_{gas} = 1.36(M_{HI} + M_{H_2})$)
[d]From Kennicutt (1998b), Σ_{gas} includes only HI and H_2
[e]Braine et al. (2001), corrected for distance
[f]Smith et al. (1999), corrected for distance, TDGC and E-HI-N use Far-Far-East pointing while and E-HI-S uses South-Far-Far-East pointing.

luminosities. If more than one HII region resides in a box, I sum the luminosities of the regions. The total Hα luminosity for each region is presented in Table 3.3.6.3. I find that TDGC now has the highest $L_{\mathrm{H}\alpha}$ in the Eastern tail, however, the Western tail HII region remains the brightest. The magenta boxes in Figure 3.1 show the location of these four areas in the Eastern tail.

3.3.6.2 Cold Molecular Gas - CO

Smith et al. (1999) used the Kitt Peak 12 meter to look for CO(1-0) in NGC 2782. They used a grid pattern with 25″ spacing and detect CO in 5 out of 6 pointings in the Eastern tail region. These locations are shown as asterisks in Figure 3.5. Only 2 pointings (Far-Far-East and South-Far-Far-East) are located in the same region as the Herschel PACS observations. To correlate the Herschel PACS observations more accurately with molecular observations, I made new observations with the Kitt Peak 12 meter at the same location. The Eastern tail location was detected at a lower signal-to-noise (about 4σ, see Figure 3.7) than previous observations, but has the same velocity as the areas observed in the Eastern tail by Smith et al. (1999). Assuming the source fills the beam (a coupling efficiency of $\eta_c = 0.64$) and a Milky Way X_{CO}, the molecular mass observed at the same location as the Herschel PACS observations is $\mathrm{M}_{mol} = 3.69 \pm 0.09 \times 10^8$ $\mathrm{M}_\odot$. In the Western tail, Smith et al. (1999) looked for CO at two locations, the northern and southern HI clumps, but did not detect any CO(1-0) emission. The HII region in the Western tail Knierman et al. (2012) is located $\sim 20''$ away from the location where Smith et al. (1999) searched for CO(1-0), so I made deeper observations at this location. The Western tail location, coincident with the Hα source (Knierman et al., 2012), remains undetected in CO(1-0) with an upper limit of $\mathrm{M}_{mol} < 0.22 \times 10^8$ $\mathrm{M}_\odot$. Braine et al. (2001) reobserved the northern clump with IRAM, but still did not detect CO. Table 3.3.6 lists the molecular gas mass or upper limits from these pointings.

The use of the standard Milky Way X_{CO} is not without precedence for tidal debris regions even though major merger TDGs have been observed to have $\sim 0.3 Z_{\odot}$ since they are pulled from the outer regions of spiral galaxies (Duc et al., 2000). The previous observations of the tidal debris of NGC 2782 by Smith et al. (1999) use the Milky Way conversion factor for ease of comparison with other observations. In Boquien et al. (2011) and Walter, Martin, & Ott (2006), the standard Milky Way CO to H_2 conversion factor ($X_{CO} = 2 \times 10^{20}$ cm^{-2} (K km s^{-1})$^{-1}$ or ($\alpha_{CO1-0} = 4.3$ M$_{\odot}$(K km s^{-1} pc^2)$^{-1}$) was used. However, as mentioned in Knierman et al. (2012), X_{CO} has a strong dependence at low metallicities (Leroy et al., 2011; Genzel et al., 2011). At a metallicity of $0.3 Z_{\odot}$ (or $\mu_0 = 8.19$), the conversion factor is $\alpha_{CO1-0} = 27.5$ M$_{\odot}$(K km s^{-1} pc^2)$^{-1}$ and gives a factor of 6 higher molecular mass limit (M$_{mol} \leq 1.2 \times 10^8$ M$_{\odot}$) than that from the standard conversion factor (M$_{mol} \leq 2 \times 10^7$ M$_{\odot}$).

3.3.6.3 Herschel/PACS observations of [CII]

Observations of [CII] with Herschel/PACS show two major peaks in the Eastern tail (Figure 3.5), but no detection in the Western tail. The peaks in the Eastern tail correspond with the two strongest Hα sources, E0 and E1. The northern peak in [CII] (TDGC) is near E1 (the location indicated for the TDGC (Yoshida et al., 1994)) and E4. The southern peak (E-HI-S) is near the brightest Hα source, E0, and the HI peak in the Eastern tail. A secondary peak of [CII] in this area is near the Hα source E555-B. The locations where spectra were extracted are indicated in Figure 3.5 with the spectra shown in Figure 3.6. As above, the extracted spectra were summed, multiplied by the bandwidth (745.96 MHz) and the flux correction factor for a single pixel (2.0), and converted to cgs units by the conversion factor of 10^{-23} erg s^{-1} cm^{-2}. I multiply the flux by $4\pi D^2$ to calculate the luminosity. To calculate I$_{[CII]}$, I divide the flux by the circular beam size of $12'$. For each location,

Table 3.3.6.3 lists the location, coordinates, luminosity of [CII], luminosity of Hα, I_{CO} from this work or for the nearest location observed by Smith et al. (1999), $I_{[CII]}/I_{CO}$, the SFR from [CII] calculated using the relation from Boselli et al. (2002), and SFR from Hα using Kennicutt (1998b). Included in the table are limits for the regions with no strong detections.

The southern source, E-HI-S, is 1.1 times brighter than the TDGC source and has a luminosity of $15.1 \pm 0.6 \times 10^{38}$erg s^{-1}. E-HI-S is similar in brightness to its neighbor, B, though some of the [CII] flux near B could be off the array. So this observation may be a lower limit. I extract a spectrum at the location of the Hα source, E2-C or E-HI-mid, even though no peak is observed in the line intensity map. Since there is [CII] emission there at a level of 4-5σ, I detect a line with luminosity less than half the value of E-HI-S. I also extract a spectrum near the location of the northeast Hα source, E3/E-HI-N, where there is no [CII] emission detected. The Western tail has an upper limit of $< 0.6 \times 10^{38}$erg s^{-1}.

To calculate the SFR from [CII], I need to correct the line luminosity to account for contamination from the warm ionized medium. Boselli et al. (2002) cite that 2/3 of the [CII] flux comes from the neutral medium based on theoretical predictions. Based on models of HII regions, Mookerjea et al. (2011) use 70% of the [CII] from the neutral medium for their calculations which is consistent with their non-detection of the [NII] 205μm line from BCLMP 302 in M33. The first observational determination of the fraction of [CII] flux from the neutral medium is from Oberst et al. (2006). They use the first detection of the [NII] 205μm line and show that 27% of the [CII] line flux should come from the warm ionized medium, leaving 73% of [CII] to come from the neutral medium. While the tidal tails of NGC 2782 may be different from the Carina nebula observed by Oberst et al. (2006), I adopt the Oberst et al. (2006) value for our determination of SFR from [CII] emission due to the paucity of observations of the [NII] 205μm line. To calculate

SFR from [CII], I multiply the [CII] flux by 0.73 (Oberst et al., 2006) and use Eq. 3 from Boselli et al. (2002) who observe nearby late-type galaxies in Hα and [CII].

3.4 Discussion

Based on the observations described above, I find both tidal tails of NGC 2782 host young star forming regions that formed within the tidal tail. The Eastern tail has more luminous star clusters which are hosted in larger star cluster complexes whereas the Western tail has only isolated star clusters. Therefore, packaging of star formation is different between the tails. The Eastern tail also has CO and [CII] emission, whereas the Western tail has non-detections. The HII region in the Western tail is more luminous than any single HII region in the Eastern tail, so the difference between the tails is not simply that the Western tail is forming stars at a lower level than the Eastern tail. To determine what might be causing these differences between two tidal tails of the same system, I compare the following properties: ambient pressure, gas phase, amount of gas, and efficiency of star formation.

3.4.1 Ambient Pressure

The difference in star formation modes between the tails could be due to a differing initial distribution of star cluster masses. Differences in cluster initial mass function (CIMF) are difficult to determine since it is hard to find young star cluster populations that have not experienced significant evolution. A few studies have attempted determining the CIMF (Portegies Zwart, McMillan, & Gieles, 2010). The CIMF is generally described like a Schechter distribution

$$\frac{dN}{dM} = AM^{-\beta}exp(-M/M_*) \tag{3.3}$$

with $\beta \sim 2$ and M_* indicating the mass at which the change in the slope of

Table 3.9: [CII] and Hα Observations of Regions in Eastern and Western Tails

Location	HαID	RA	Dec	$L_{[CII]}$ 10^{38} erg s^{-1}	$L_{H\alpha}$ 10^{38} erg s^{-1}	I_{CO} K km s^{-1}	$I_{[CII]}/I_{CO}$[a]	SFR([CII])[a] $M_\odot yr^{-1}$	SFR(Hα)[b] $M_\odot yr^{-1}$
East									
TDGC	E1,E4	9:14:10.92	+40:06:48.8	13.4(0.6)	10(1.2)	0.39(0.06)[a]	2950	0.032(0.001)	0.008(0.001)
E-HI-N	E3	9:14:12.46	+40:06:50.6	<0.9	4.1(0.6)	0.39(0.06)[c]	<190	<0.004	0.0032(0.0005)
E-HI-M	E2	9:14:11.46	+40:06:35.6	6.3(0.7)	2.0(0.4)	0.43(0.05)	1840	0.0170(0.005)	0.0016(0.0003)
E-HI-S	E0	9:14:11.26	+40:06:20.6	15.1(0.6)	6.7(0.9)	0.57(0.08)[c]	4860	0.0347(0.001)	0.0053(0.0007)
E-HI-S-B	E555	9:14:10.66	+40:06:26.6	>14.1(0.7)[d]	6.0(0.9)	0.57(0.08)[c]	4520	>0.033(0.002)	0.0047(0.0007)
Total[e]	all	9:14:10.63	+40:06:41.6	77(2)	29(2)	0.43(0.05)	> 1148	0.125(0.003)	0.023(0.002)
West									
W-HI-M	W235	9:13:51.2	+40:08:07	<5.6	19(3)	<0.02	<35200	<0.02	0.015(0.002)

[a] 1 K km s^{-1} = 1.6×10^{-9} erg s^{-1} cm^{-2} sr^{-1} (Stacey et al., 1991)
[b] Using equation from Boselli et al. (2002) (d) Using equation from Kennicutt (1998b)
[c] Smith et al. (1999)
[d] Lower limit since source is at the edge of the array.
[e] Total of the area of the Herschel/PACS spectral observations.

the mass function occurs. For spiral galaxies like the Milky Way, $M_* \sim 2 \times 10^5$ $M_\odot$, but interacting galaxies like the Antennae show $M_* > 10^6$ $M_\odot$ (Portegies Zwart, McMillan, & Gieles, 2010). Therefore, the environment where star cluster formation occurs seems to affect the CIMF and, in particular, the value of M_*.

This possible difference in CIMF between the tails might be due to the difference in the spatial arrangement of molecular gas. Forming stars tend to destroy their parent molecular environment, leaving behind clumpy remnants of molecular material. Beam dilution may render the CO unobservable even with moderate resolution ($< 1'$) like the CO observations of the HI peaks in the Western tail Smith et al. (1999) and Braine et al. (2001). With the concentration of molecular gas in small clumps, the tail may have produced correspondingly lower mass star clusters.

A second possibility for the difference in CIMF could be due to a lower metallicity. With a lower metallicity there would be less carbon and oxygen to make CO so I may not detect it. However, why a lower metallicity environment would make lower mass clusters is an open question.

A third possibility for the difference in CIMF between the tails could be due to the environment. The ambient pressure in the Western tail could be lower than in the Eastern tail which would lower the star formation rate (Blitz & Rosolowsky, 2006), possibly making lower mass star clusters. Even for solar metallicities, when the ambient pressure is low, CO will form deeper within the dense star forming cloud.

I examine the third possibility next. The locations and masses of GMCs are likely to be regulated by the structure of the HI from which the GMC formed, particularly in galaxies which are dominated by atomic gas (Blitz & Rosolowsky, 2006). In particular, M33 shows this correlation between its GMCs and peaks in the HI gas (Rosolowsky et al., 2007).

While Braine et al. (2001) stated that the lack of CO down to sensitive limits at places of high column density HI indicated that the Western tail is not gravitationally bound and so the gas has not collapsed to form H_2 and hence new stars, the observations presented here show that new star clusters are being formed in the tail. Based upon HI peaks in the Western tail of NGC 2782, GMCs are expected to be at those locations. The largest size of the molecular cloud that one would expect to be associated with the HI clump can be estimated using the formulation for M_{char} of Elmegreen, Kaufman, & Thomasson (1993):

$$M_{char} = \pi l_{min} c_g \sqrt{\frac{\mu}{2G}} \tag{3.4}$$

where c_g is the velocity dispersion of the gas in 3-D, μ is the mass per unit length of the cloud (M/l_{max}), and l_{min} and l_{max} are the minor and major axes of the HI cloud. This equation gives the characteristic mass of a "supercloud" using the size, mass, and velocity dispersion of the HI clump. This supercloud is the overall entity which becomes self-gravitating and the GMCs collapse to form inside this supercloud by turbulent fragmentation.

Table 3.4.1 has the M_{HI}, velocity dispersion, size and resulting M_{char} for 3 HI clumps in the Eastern tail and 3 HI clumps in the Western tail. Smith (1994) measured 10 HI clumps in the Western tail, but the 3 presented here are ones with star cluster candidates at that location. The M_{char} for the Eastern Tail clumps ranges from $9.5 - 18 \times 10^8$ $M_\odot$while the Western tail is slightly smaller with a range from $6.6 - 11 \times 10^8$ $M_\odot$.

While M_{char} does not predict an exact mass for a GMC, this does indicate that similar masses of GMCs are expected in both the Eastern and Western tails. However, no molecular gas was observed in the Western tail down to a limit two orders of magnitude below M_{char}. A massive HI clump in the NW tidal tail of NGC

Table 3.10: Characteristic Sizes of HI Clumps in the Tidal Tails of NGC 2782

Location	σ_v[a] (km/s)	l_{min} (kpc)	l_{max} (kpc)	M_{HI}[a] ($10^8 M_\odot$)	M_{char} ($10^8 M_\odot$)	Observed M_{mol} ($10^8 M_\odot$)
E-HI-N	30	2.96	2.96	3.85	15.3	2.6(0.5)[b]
E-HI-M	40	1.78	2.96	2.31	9.50	3.69(0.09)
E-HI-S	40	2.96	5.92	6.02	18.1	3.8(0.5)[b]
W-HI-N	49	2.10	3.05	0.54	6.56	< 0.086[c]
W-HI-M	35	5.67	7.56	1.00	10.9	< 0.22
W-HI-S	30	3.78	3.78	0.86	8.19	< 1.5[b]
N7252 TDG	31	5.00	5.00	10	33.2	0.2

[a](Smith, 1994; Smith et al., 1999)
[b](Smith et al., 1999)
[c](Braine et al., 2001)

7252 has $M_{char} \sim 3.3 \times 10^9$ $M_\odot$. This clump, as shown in Table 3.4.1, has more HI than those in NGC 2782 and molecular gas of 2×10^7 $M_\odot$.

That the Western tail lacks molecular gas at the locations of high HI column density could be due to either its absence or its inobservability. In the less dense region of the Western tail, even a small amount of star formation could have destroyed the molecular gas there. The Eastern tail is more dense and so its molecular gas would not be destroyed as easily. If the molecular gas is not entirely destroyed by the radiation of young stars, it could exist instead in smaller clouds which would be greatly affected by beam dilution with single dish telescopes (beam sizes of $22''$ to $1'$).

3.4.2 Gas Phase

I examine whether the lack of massive star clusters and star cluster complexes in the Western tail is related to the properties of the ISM in the tidal tail. To do this, I look at various tracers of the reservoir of gas available for star formation in both tails on both local and global scales. I first compare neutral hydrogen gas to molecular gas traced by CO emission. Then I compare neutral hydrogen to ionized

gas traced by [CII] emission. Finally, I compare molecular gas traced by CO emission to ionized gas traced by [CII] emission.

Comparing the CO and HI mass ratio, I find the highest to be TDGC ($M_{H_2}/M_{HI} = 6$) the other three regions have ratios of 0.5, 1, and 0.5 for the north, mid, and south regions, respectively. In the Western tail, I find $M_{H_2}/M_{HI} < 0.2$. This indicates that there is less CO in the Western tail for the HI mass as compared to the Eastern tail on local scales.

I next compare the [CII] to HI. In Figure 16 of Stacey et al. (1991), they plot the expected [CII] line flux for given HI column densities for various phases of the ISM in the infinite temperature limit. The galaxies of their sample lie about 2 dex above the lines for "standard" HI clouds and the intercloud medium. In direct comparison to their galaxies and Galactic HII regions, the local regions in the Eastern and Western tail of NGC 2782 are deficient in [CII] by about 2 dex. The Eastern tail has an average HI column density of 6×10^{20} cm^{-2}, with a peak of 1.75×10^{21} cm^{-2} in the E-HI-S region. For a "standard" HI cloud ($n_H \sim 30$ cm^{-3}), the peak column density in the Eastern tail predicts $I_{[\mathrm{CII}]} \sim 5 \times 10^{-6}$ erg s^{-1} cm^{-2} sr^{-1} which is a factor of 1.6 larger than that observed in E-HI-S. If I consider the average HI column density for the Eastern tail, then $I_{[\mathrm{CII}]} \sim 2 \times 10^{-6}$ erg s^{-1} cm^{-2} sr^{-1} which is similar to the values observed for the Eastern tail. In the Western tail, the HI column density is $\sim 1 \times 10^{21}$ cm^{-2} and the predicted value for $I_{[\mathrm{CII}]}$ is a few times the observed upper limit for [CII].

To directly compare [CII] to CO, I determine the ratio of their intensities. Our values for $I_{[\mathrm{CII}]}$ are calculated by dividing the flux of [CII] by the beam size (a HPBW of 12″). As shown in Table 3.3.6.3, I observe the $I_{[\mathrm{CII}]}/I_{CO}$ ratio to range from 1840-4860 for those where both [CII] and CO are detected. This is at the lower end of the values for most of the normal and starburst galaxies observed Stacey

et al. (1991) and aligns more with the values for Galactic HII regions and molecular clouds. Stacey et al. (1991) found that there was a constant ratio between [CII] and CO fluxes for starburst and Galactic OB star forming regions ($I_{[\mathrm{C\,II}]}/I_{CO} = 6300$). The ratio for TDGC is 2950 and the ratio for E-HI-S is 4860. These values are a few times lower than the constant ratio. The limit for the Western tail gives a $I_{[\mathrm{C\,II}]}/I_{CO} > 35200$. Stacey et al. (1991) finds the ratio to be lower for non-OB star forming regions in the Milky Way and normal galaxies with lower dust temperatures and those ratios range from 4400 to as low as 900 which match with our observations in the Eastern tail. Our limit in the Western tail is larger than the constant ratio from Stacey et al. (1991) and is more similar to their value for 30 Dor in the LMC ($I_{[\mathrm{C\,II}]}/I_{CO} = 40,000$) which is also an area of lower metallicity than most of their other observed regions. If I compare to the more recent observations of area of the HII region BCLMP 302 in M33 Mookerjea et al. (2011), I find our values align to their range of ratios from $1000 - 70,000$ shown in Figure 12 of their erratum. For the HII region BCLMP 302 itself, the values of $I_{[\mathrm{C\,II}]}/I_{CO}$ range from $6000 - 30,000$ which are higher than our ratios for the Eastern tail, but have an upper end similar to the limit for the Western tail HII region. The HII region BCLMP 302 in M33 has a $L_{\mathrm{H}\,\alpha} = 2.2 \times 10^{38}$ erg s^{-1} which is similar to the HII regions in the Eastern tail. However, the [CII] intensity in BCLMP 302 is 28 times lower in the Eastern tail and 84 times lower than the Western tail limit.

There may be a mismatch between the CO observations and the [CII] peaks from the different beam sizes of the two instruments. PACS spectrometer has a beam with half power beam width (HPBW) of $12''$ at 159μm while the CO data are from the Kitt Peak 12 meter which has a beam with FWHM of $55''$. I instead extract [CII] spectra from the PACS array by summing the flux from the whole array to better match the CO beam and by dividing the flux by the area of the array ($47'' \times 47''$). This is indicated in Table 3.3.6.3 as "Total". Even with summing

the flux from the whole PACS array, the CO observations still have a larger beam size which means I have a lower limit on the ratio of $I_{[\mathrm{CII}]}/I_{CO} > 1148$.

In either case, it appears that the Eastern tail has a deficiency of [CII] since the $I_{[\mathrm{CII}]}/I_{CO}$ ratio is on the low end of regions previously observed. And given that this is among the first tidal tail region to be observed in [CII], having a lower value for $I_{[\mathrm{CII}]}/I_{CO}$ may not be surprising.

3.4.2.1 Non-detection of [CII] in the Western tail

Given the non-detection of CO in the Western tail, I might expect the molecular gas to be in another form. CO does not form until and A_V of 3 or more, while H_2 forms at A_V of less than 1 (Hollenbach & Tielens, 1997). In a low pressure environment like a tidal tail a substantial amount of molecular gas can exist with conditions that do not favor the formation of CO, so the CO to H_2 conversion factor is not a constant. In the low gas density environment of tidal debris a substantial reservoir of molecular gas can exist at low A_V that will not be detectable through CO. However, in this regime, [CII] will be present in higher amounts. Theoretical models for molecular clouds in Wolfire, Hollenbach, & McKee (2010) show that the fraction of molecular mass in the "dark gas" (H_2 and [CII]) is $f \sim 0.3$ for typical galactic molecular clouds. For lower A_V and lower metallicities (as in these tidal tail regions), the fraction of dark mass in H_2 increases. Given this reason, I observed the Western tail with Herschel to see if [CII] was present where CO was not.

I do not find [CII] in the Western tail at the location of the HII region at a significant level. This HII region has a higher Hα luminosity than any individual HII region in the Eastern tail, but [CII] emission is only detected in the Eastern tail. Given that Hα and [CII] emission ultimately originate from the same sources of hard UV photons with energy greater than 13.8 eV, they are expected to trace each other. In BCLMP 302 in M33, Mookerjea et al. (2011) find [CII] emission 84

times greater than the Western tail limit, even though it has an Hα luminosity 9 times less than the Western tail.

If carbon was not available to be ionized, the most likely place for it to be is in CO. However, the Western tail has no detected CO at this location. From the calculations of the characteristic mass in Section 4.2 of the paper, I expect the largest size of the molecular cloud mass to be $\sim 1 \times 10^9$ M$_\odot$, but the upper limit for this region is 0.2×10^8 M$_\odot$. (in the Eastern tail, M$_{char}$ is $\sim 3-5$ times the observed value of M$_{mol}$, so the factor of 54 between M$_{char}$ and the upper limit on molecular mass in the Western tail is significant). The lack of [CII] and CO emission would then indicate that this HII region is likely to have a low carbon abundance. However, previous emission line spectra of this HII region (Torres-Flores et al., 2012; Werk et al., 2011) from Gemini have shown that it has a metallicity greater than solar. This seems to be at odds with the non-decections of [CII] and CO in the Western tail. However, Torres-Flores et al. (2012) use nebular oxygen emission for their metallicity determination. It is possible for this to be compatible with a low carbon abundance and a very low C/O ratio. Oxygen is the most common element produced in core collapse supernovae events whereas carbon is produced in relatively small amounts. The source of most carbon in the ISM is AGB stars. If this material has been primarily enriched by recent star formation, it is possible to build up a high abundance of oxygen and alpha elements without producing a significant enhancement of carbon and also iron. The age of the Western tail is about 200-300 Myr and so in situ star formation in the tail is unlikely to have synthesized large quantities of carbon (Arnett, 1996).

Also, molecular gas may have been dissociated by a high UV flux in this region, associated with the most massive stars in the star cluster. FUV-NUV color from GALEX observations by Torres-Flores et al. (2012) show that this region show a FUV-NUV color of -0.14 mag. For a simple Salpeter IMF of $dN/dM = cM^{-(1+x)}$

with x=1.35, a $10^{5.35}$ $M_{\odot}$cluster contains 1660 stars of 8 $M_{\odot}$ or greater. Even for an extreme value of x=2.35, there are still 40 stars of 8 or more $M_{\odot}$. This provides sufficient UV flux to photodissociate H_2 out to several hundred parsecs, comparable to the size of the Orion Molecular Cloud Complex. It is therefore unlikely that molecular gas has long lifetimes unless present at high densities, as in the Eastern tail of NGC 2782.

3.4.3 Star Formation in Tidal Debris

To consider whether the difference in star formation modes between the two tails is due to the amount of gas present for star formation, in each tail I calculate the star formation rates per unit area from the Hα luminosity and also from [CII] luminosities and compare these to the predicted SFR from the gas surface density. This is done for global values of the tidal tails as well as locally over HI clumps in both tails.

3.4.3.1 Star Formation on Global Scales

Using the entire tail areas as calculated above, I find the SFR and SFR per area (Σ_{SFR}) for both tails. In Table 3.3.6, the global properties of Σ_{SFR} from [CII], from the Hα luminosity, and the total gas surface density (including both HI and molecular gas) are listed for each tail. For this calculation I use the $L_{H\alpha}$ from Smith et al. (1999) since they detected fainter Hα emission than these observations. In the Eastern tail the Σ_{SFR}(Hα) is an order of magnitude below the expected value of Σ_{SFR}(gas). In the Western tail, Σ_{SFR}(Hα) is two orders of magnitude below the expected value from the gas density.

Using the summed flux over the entire PACS spectroscopy array, as described above and equation for SFR from [CII] in Boselli et al. (2002), I calculate the Global SFR ([CII]) for the Eastern tail to be 0.125 $M_{\odot}$ yr^{-1}. If I assume that

the flux detected by the PACS pointing is the entirety of the [CII] in the Eastern tail, $\Sigma_{SFR} = 4 \times 10^{-5}$ M$_\odot$ yr^{-1} kpc^{-2}. This value is 4 times larger than the value from $\Sigma_{SFR}(\mathrm{H}\alpha)$, but still 8 times less than the expected value from the gas density. However, Boselli et al. (2002) find that the dispersion in their SFR correlation ~ 10. So a factor of 4 difference is within the scatter. They do say that [CII] line luminosity can be taken as a star formation indicator for normal late-type galaxies ($8.0 < \log L_{FIR} < 10.5$), but may be not applicable to ULIRGs. The NGC 2782 galaxy itself is a LIRG with an IRAS luminosity of 1.6×10^{44} erg s^{-1} which is at the high end of this range. However, I study the tidal tails which would have lower FIR emission than the central regions of the merger. Whether to use [CII] as a direct indicator for star formation is a matter of some debate, however, there have been recent calibrations of the SFR from [CII] for different regimes such as starbursts (De Looze et al. , 2011) and HII regions in M33 (Mookerjea et al., 2011).

The global $\Sigma_{SFR}(\mathrm{H}\alpha)$ calculated for these tidal tails is two to three orders of magnitude lower than those found in spiral galaxies as well as dwarf galaxies. Kennicutt (1998b) find that $-3.3 < \log(\Sigma_{SFR}) < -0.8$ in 61 normal spiral galaxies. The Milky Way galaxy has $\Sigma_{SFR} = 3.6 \times 10^{-3}$ M$_\odot$ yr^{-1} kpc^{-2} (Naab & Ostriker, 2006). The LMC has a global star formation rate of 0.4 M$_\odot$ yr^{-1} which gives $\Sigma_{SFR} = 1.5 \times 10^{-3}$ M$_\odot$ yr^{-1} kpc^{-2}. The SMC has a global star formation rate of 0.05 M$_\odot$ yr^{-1} which gives $\Sigma_{SFR} = 1.9 \times 10^{-4}$ M$_\odot$ yr^{-1} kpc^{-2} (Wilke et al., 2004).

The $\Sigma_{SFR}(gas)$ is similar in magnitude to values in the LMC and SMC. The Magellanic Stream is a very nearby example of a gas tail of presumably tidal origin that has no star formation associated with it. Putman et al. (2003) measured the total HI gas mass in the Stream to be 2.1×10^8 M$_\odot$. Converting the angular size of the Stream ($100^\circ \times 10^\circ$) using a distance of 55 kpc (Putman et al., 2003), I infer a size of the Magellanic Stream to be 940.9 kpc^2. Using the resulting gas density of $\Sigma_{HI} = 2.2 \times 10^5$ M$_\odot$ kpc^{-2}, the Magellanic Stream has an expected

$\Sigma_{SFR} = 3 \times 10^{-5}$ $M_\odot$ yr^{-1} kpc^{-2} which is two orders of magnitude lower than that calculated for the Western tidal tail of NGC 2782 and four orders of magnitude lower than the Eastern tail.

The difference between the Σ_{SFR} values calculated from the Hα flux and that predicted from the gas density may indicate a lower star formation efficiency (Knierman et al., 2012). However, the Hα SFR is a lower limit since it only traces massive star formation in the last 5 Myr. Also, the Hα emission may depend on the masses of the star clusters formed. If the tails only formed lower mass star clusters where few high mass stars reside, similar to the Taurus-Auriga region (Kenyon et al., 2008), there would be young, blue star clusters but a lack of widespread Hα emission. The Western tail has only one small in size HII region, but several other blue star cluster candidates. Galaxy Evolution Explorer (GALEX) All-sky Imaging Survey (AIS; Morrissey et al., 2007) images show faint UV emission along the Western tail, indicating a young stellar population, probably dominated by B and A stars (Knierman et al., 2012; Torres-Flores et al., 2012). In addition, the emission is concentrated only in specific areas in both tails rather than being spread over the tail region. This may indicate that global star formation rates from Hα or [CII] are not an accurate assessment of the total star formation in the tails.

3.4.3.2 Star Formation on Local Scales

I also examine the star formation on local scales in both tails using Hα and [CII]. Table 3.3.6.3 shows the SFR from Hα for these massive HI clumps using Kennicutt (1998b) which range from 0.0016-0.008 $M_\odot$ yr^{-1} in the Eastern tail and 0.015 $M_\odot$ yr^{-1} for the Western tail source. The Western tail source has a factor of 2-3 higher SFR than TDGC and E-HI-S the two most luminous Hα sources in the Eastern tail. Using the [CII] luminosity and the equation for SFR from Boselli et al. (2002), the range of SFR in the Eastern tail is 0.017-0.035 $M_\odot$ yr^{-1} and < 0.02 $M_\odot$ yr^{-1} in the

Western tail. The SFR is a factor of 7 larger from [CII] than from Hα for E-HI-S the most luminous [CII] source in the Eastern tail while for TDGC, SFR([CII])= 4 SFR(Hα). I expect a lower SFR(Hα) than SFR([CII]) since Hα is affected by extinction and also only traces the most recent star formation. However, in the Western tail the HII source has SFR(Hα) similar to the upper limit for the SFR([CII]). Since the Eastern tail shows a higher SFR([CII]) than SFR(Hα), the at most equal values in the Western tail, but likely lower SFR([CII]) indicates that perhaps something is happening in the Western tail to suppress [CII] emission.

These comparisons may be affected by differing areas, so I calculate the SFR per area (Σ_{SFR}) to compare regions. The local values for SFR per area from Hα are $2 - 11 \times 10^{-4}$ M$_\odot$ yr^{-1} kpc^{-2} for the regions in the Eastern tail. The TDGC region has a similar Σ_{SFR} to the Western tail Hα region ($\Sigma_{SFR} = 1 \times 10^{-3}$ M$_\odot$ yr^{-1} kpc^{-2}). The remainder of the Eastern tail sources are 2-4 times lower than the Western tail source. This seems to indicate local star formation as indicated by Hα is occuring at similar levels in each tail. The Σ_{SFR}([CII]) in the Eastern tail ranges from $2.5 - 4.5 \times 10^{-3}$ M$_\odot$ yr^{-1} kpc^{-2} and in the Western Tail is $< 1.1 \times 10^{-3}$ M$_\odot$ yr^{-1} kpc^{-2}. The TDGC region has the highest Σ_{SFR}([CII]) at 2 times the other two detected regions and this region is 4 times larger than the limit in the Western tail.

Using the total gas surface density, I find even higher expected star formation rates. In the Eastern tail, I expect Σ_{SFR} of 0.05-0.18 M$_\odot$ yr^{-1} kpc^{-2}. Due to the non-detection of CO in the Western tail, the star formation rates from the gas density are upper limits. Even so, these upper limits are lower than the Eastern tail by a factor of 10-40 ($\Sigma_{SFR}(gas) < 0.005 - 0.009$ M$_\odot$ yr^{-1} kpc^{-2}).

In summary, on local scales, I find the Western tail HII region has the highest SFR using Hα as a tracer, but has a low SFR using its upper limit in [CII]. This indicates that [CII] is suppressed relative to Hα in the Western tail.

Normalized to area, I find similar SFR per unit area in both tails using Hα as a tracer. This seems to indicate that star formation is occurring locally at similar rates in both tails. The expected SFR per area from the local gas density is higher than that observed by both Hα and [CII] indicating that there may be a lower SFE at the local level in both tails as well. Comparing the tails, the expected local SFR surface density from the observed local gas density is 14-40 times higher in the Eastern tail than in the Western tail. This indicates that there is a larger gas reservoir for star formation in the Eastern tail at least on local scales.

3.4.4 Star Formation Efficiency

Having calculated the SFR for each region, I now examine the star formation efficiency (SFE) for these local regions. Boquien et al. (2011) use multiwavelength data of major merger Arp 158 to study the local Kennicutt-Schmidt law. They find that star forming regions in the tidal debris follow a different Kennicutt-Schmidt law than those in the central regions of the merger, falling along a line of similar slope to Daddi et al. (2010), but offset so that the same gas density gives lower values of SFR. As discussed in Knierman et al. (2012), W235 is consistent with the other star forming regions in the tidal debris of Arp 158 indicating a lower SFE than in the central region of Arp 158. If I compare the Eastern tail star forming regions to the tidal debris of Arp 158, I find that for their given total gas surface density, their star formation rates from Hα lie more than 2 dex below the relation for the tidal debris of Arp 158 indicating a substantially lower SFE in the Eastern tail.

I calculate the gas depletion timescales (τ_{dep}) or the amount to time it would take for the current SFR to deplete the gas (either molecular or atomic). The SFE is the inverse of the gas depletion time. Table 3.4.4 lists region, depletion timescale of molecular gas mass vs. SFR from Hα (τ_{dep,H_2} =$\mathrm{M}_{mol}/\mathrm{SFR}_{\mathrm{H}\alpha}$), depletion timescale of neutral gas mass vs. SFR from Hα ($\tau_{dep,\mathrm{HI}}$ =$\mathrm{M}_{\mathrm{HI}}/\mathrm{SFR}_{\mathrm{H}\alpha}$), depletion

timescale of molecular gas mass vs. SFR from [CII] (τ_{dep,H_2} =M_{mol}/$SFR_{[CII]}$), and depletion timescale of neutral gas mass vs. SFR from [CII] ($\tau_{dep,HI}$ =M_{HI}/$SFR_{[CII]}$)) for the local and global regions in both tails.

The highest SFE ($\tau_{dep,H_2} < 1.5$ Gyr) is in the Western tail HII region considering the molecular gas limit and Hα SFR. This is comparable to the molecular gas depletion timescales determined for the star forming regions in Arp 158 ($\tau_{dep} \sim 0.5 - 2$ Gyr; Boquien et al., 2011) and in TDGs ($\tau_{dep} \sim 0.8 - 4$ Gyr; Braine et al., 2001). These ranges are also similar to the average gas depletion timescales in spiral galaxies. If I use the value for the CO emission assumed in the discussion of Torres-Flores et al. (2012) using an analog HII region in the tidal debris near NGC 3077, I might expect it to have molecular mass of 1.5×10^6 $M_\odot$. If I use this value for the molecular mass, $\tau_{dep,H_2} = 0.1$ Gyr, making this region similar to gas depletion timescales in dwarf galaxies (1 -100 Myr). If this molecular mass is close to the actual value, this would mean that this region is highly efficient at making stars.

Considering neutral gas and SFR from Hα, TDGC and W235 ($\tau_{dep,HI} = 5 - 7.7$ Gyr) are less efficient than normal star forming regions. But these areas are still more efficient at star formation than outer regions of spiral galaxies at r_{25} ($\tau_{dep,HI} \sim 20$ Gyr) or dwarf galaxies at r_{25} ($\tau_{dep,HI} \sim 40$ Gyr). Using the molecular gas and Hα SFR, TDGC and E-HI-S have depletion timescales of 33 Gyr and 38 Gyr similar to these less efficient regions. Bigiel et al. (2010) find very low SFE ($\tau_{dep,HI} \sim 100$ Gyr) in the outer disks of spiral galaxies using FUV and HI observations. Even less efficient than outer disk regions is the E-HI-mid region. Smith et al. (1999) also found low star formation efficiency in the Eastern tail using the ratio of $L_{H\alpha}/M_{H_2}$. Overall, our results comparing SFR(Hα) and gas mass indicate that on local scales the Western tail is more efficient at forming stars than the Eastern tail.

Considering molecular gas and SFR from [CII], the Western tail limit remains with the highest SFE, however, both the gas mass and SFR([CII]) are upper limits. In the Eastern tail, E-HI-S has the highest SFE, but with a depletion timescale of 5.6 Gyr is still less efficient than normal star forming galaxies. Considering the neutral gas, TDGC has the highest SFE ($\tau_{dep,\mathrm{HI}} = 1.3$ Gyr) indicating efficient star formation. Using [CII], the Western tail is also more efficient at star formation than most of the Eastern tail except for TDGC considering its HI mass.

Since the CO observations were taken with a large beam, I examine the Eastern tail on larger scales. Even if I consider the total molecular and neutral hydrogen for the entire Eastern tail, the SFE remains low (16-43 Gyr). For the Western tail as a whole, I sum the limits from the three CO pointings and use the total HI mass from Smith (1994). The Western tail has a low SFE considering the molecular gas mass limits and the single HII region (< 12 Gyr), but is very inefficient considering the HI mass of the tail (133 Gyr). So on global scales, it appears that the Western tail is less efficient at forming stars.

On both global and local scales, it appears the Western tail is more efficient at forming stars than the Eastern tail. The Western tail also lacks high mass star clusters and star cluster complexes which are hosted in the Eastern tail. These two points are not inconsistent. In the Eastern tail, star cluster complexes of higher mass will form many more high mass stars than isolated lower mass star clusters in the Western tail. These high mass stars provide feedback and energy into the ISM in the form of stellar winds and supernova. This feedback can suppress further star formation and have a lower SFE in the area. In addition, Smith et al. (1999) suggest that the Eastern tail formed as a "splash" region (versus a tidal region of merger debris) and may have inhibited star formation due to gas heating during the encounter. A tidally formed region such as the Western tail, would have

Table 3.11: Comparison of Star Formation Efficiencies Between Eastern and Western Tails

Location	$\tau^{a}_{dep,H_2,H\alpha}$ (Gyr)	$\tau^{b}_{dep,HI,H\alpha}$ (Gyr)	$\tau^{c}_{dep,H_2,[CII]}$ (Gyr)	$\tau^{d}_{dep,HI,[CII]}$ (Gyr)
East				
TDGC	33	5	8.2	1.3
HI-N	81	160	>70	>141
HI-M	232	200	21	18
HI-S	38	81	5.6	12
E Tail	16[e]	43	2.7[e]	7
West				
HI-N	<29[e]	>240		
HI-M	<1.5	7.7	<1.4[b]	>7.3
HI-S	<53[f]	>390		
W Tail	< 12	133	< 4[f]	> 45

[a] $\tau_{dep,H_2,H\alpha}$ =M_{mol}/SFR(Hα)
[b] $\tau_{dep,HI,H\alpha}$ =M_{HI}/SFR(Hα)
[c] $\tau_{dep,H_2,[CII]}$ =M_{mol}/SFR([CII])
[d] $\tau_{dep,HI,[CII]}$ =M_{HI}/SFR([CII])
[e]Using observations from this work.
[f]Both gas mass and SFR are upper limits.

gravitational compression and possibly enhanced star formation. Given the higher SFE in the Western tail, this may be evidence for gravitational compression in the tidal tail.

3.5 Conclusions

Tidal tails provide laboratories for star formation under extreme conditions very different from quiescent galaxy disks. With low gas pressures and densities and smaller amounts of stable molecular gas they are perhaps on the edge of the parameter space open to star formation.

The two tails of NGC 2782 are an interesting place to consider in this discussion. The Western tail is rich in HI gas, but CO is not observed in the massive HI knots in the tail, leading Braine et al. (2001) to conclude that HI "...has presumably not had time to condense into H_2 and for star formation to begin." This study finds that at least 10 star clusters have formed in the Western tail based on the overdensity of bright, blue objects in the tail. The Western tail also hosts a bright HII region which was explored in Knierman et al. (2012) while 6 additional young regions are found in FUV and NUV by Torres-Flores et al. (2012) and in Hα by Werk et al. (2011). Clearly the lack of observable CO does not guarantee the absence of recent star formation. It may play a role, however, in the properties of star clusters forming therein since the Western tail lacks high mass star clusters and star cluster complexes. The Eastern tail has a dense knot of HI and CO-rich gas at its base. Based on the overdensity calculations, at least 14 young star clusters are observed in this region of the tail. The Eastern tail also hosts several HII regions (Smith et al., 1999), of which I discover [CII] associated with five of these regions. In contrast, the Western tail Hα source shows only an upper limit on [CII] contrary to expectations based on its bright HII region and its HI column density.

I examined in turn the reasons for the differences between the two tails: ambient pressure, gas phase, SFR, amount of gas available for star formation, and efficiency of star formation.

Ambient pressure: Based on the calculation for M_{char} in local regions in the Western tail, I find that the M_{char} in the Eastern tail is only slightly larger than in the Western tail. I surmise that the relatively small difference between the predicted clump mass in the two tails indicates that the ambient pressure between the two tails is not very different. However, there is a large difference between M_{char} and the upper limit on molecular mass in the Western tail indicating that the Western tail is deficient in molecular mass (or at least, in CO).

Gas phase: I find that the Western tail has much less molecular gas mass (traced by CO) for its neutral hydrogen mass than the Eastern tail. This indicates that CO may be suppressed in the Western tail. Both tails are lower in their [CII] intensity based on their HI as compared to observations of nearby galaxies and Galactic regions. The Eastern tail HI regions are close, but still below, the expected [CII] values for "standard" HI clouds while the Western tail limit is a few times below that. I also find a lower $I_{[\mathrm{CII}]}/I_{CO}$ in the Eastern tail than studies of nearby star forming galaxies and Galactic HII regions which is in line with GMCs and normal galaxies.

SFR: Using the entire tail area, I find that the global SFR from Hα and from [CII] are much less than the SFR expected from the gas surface density suggesting that both tails have low SFE. On local scales, I find the Western tail HII region has the highest SFR from Hα, but has only an upper limit for SFR from [CII]. This indicates that [CII] emission is suppressed in the Western tail relative to Hα. Normalized to their areas, I find similar local $\Sigma_{SFR}(\mathrm{H}\alpha)$ in both tails indicating that star formation is occurring similarly on the local scale in both tails. For each local region, the expected SFR from the gas density is higher than from Hα or [CII] indicating lower SFE at the local level as well. Comparing the two tails, the expected local SFR density from the gas density in the Eastern tail is 14-40 times higher than in the Western tail.

Gas Reservoirs for SF: I examined different tracers for the reservoirs of gas for star formation in these two tidal tails and found that these tracers were not consistent. Both tails have abundant neutral hydrogen gas, but the Eastern tail has more molecular gas (traced by CO) and ionized gas (traced by [CII]). However, the Western tail has a higher local SFR and both tails have similar SFR per unit area, indicating that star formation according to Hα emission is similar in both tails. If I use [CII] emission as a SFR tracer, I find that the Eastern tail has a higher SFR than the Western tail. Looking at gas density, the Eastern tail has a higher total gas surface density than the Western tail. So I expect a higher SFR per area in the Eastern tail. That these tracers are not consistent between the tails indicates that something different is going on between the tails. In the Western tail, the non-detections in CO and [CII] compared to its HI and Hα may be due to its inability to produce detectable CO or [CII] emission. This may be due to a deficiency in carbon even though it has a high oxygen abundance, because the tail material is going through its first generation of stars and has not had enough time to build up a higher carbon abundance.

SFE: By calculating the gas depletion timescales for molecular gas and neutral hydrogen, I examine SFE in the tails. As discussed in Knierman et al. (2012), the Western tail HII region has a normal SFE when considering its molecular mass upper limit, but less efficient star formation if I consider its neutral hydrogen mass. The Eastern tail regions have a low SFE, in some cases as low as spiral or dwarf galaxies at r_{25}. I suggest that the lower SFE in the Eastern tail may be due to its more massive star clusters providing feedback to prevent further star formation. Also, the Eastern tail may have a lower SFE due to its formation mechanism as a splash region where gas heating has a higher effect. The Western tail has a higher SFE even though it has a lower local gas surface density than the Eastern tail, possibly due to its tidal formation where gravitational compression has

more of an effect and can increase star formation.

Chapter 4

STAR FORMATION IN THE TIDAL TAIL OF UGC 10214 ("THE TADPOLE")

4.1 Introduction

The centers of galaxy mergers where high gas densities cause bursts of star formation are well studied. However, a comparable mass of gas to that in the center can be in the tidal debris which can fuel star formation in these less dense environments. To help determine if star formation in tidal debris is related to gas properties, I use the methods of Knierman et al. (2013) (hereafter K13) and apply them to another merger system. In this case, I examine UGC 10214 ("The Tadpole") which is also known as Arp 188 and VV 29. The Tadpole is known for its distinctive shape which results from the minor merger of a spiral galaxy with a dwarf galaxy. The dwarf galaxy is still partially intact and can be seen to the west of the nucleus in the HST/ACS optical image shown in Figure 4.1 (Tran et al., 2003) and as a distinct velocity feature in HI 21 cm (Briggs et al., 2001). A long narrow tidal tail extends to the east and is twice as long as the main spiral galaxy's long axis. This particular tidal tail is interesting due to the location of its large star forming clump in the center of its tail. In major mergers, a large blue star forming clump is often found at the end of the tidal tail. These clumps can be dwarf galaxy sized and can earn the name "Tidal Dwarf Galaxy" (e.g., Knierman et al., 2003; Duc et al., 2000; Mullan et al., 2011). For this paper, I use a distance to the Tadpole of 134.2 ± 9.4[8] Mpc (Mould et al., 2000).

This system has been studied in many wavelengths including 21 cm (Briggs et al., 2001), HST/ACS optical (Tran et al., 2003; de Grijs et al., 2003), and Spitzer (Jarrett et al., 2006). Briggs et al. (2001) were searching for evidence of a dark halo colliding with the Tadpole, but instead discovered the normal dwarf companion

[8]From NED, corrected for Virgo, Great Attractor, and Shapley.

galaxy that now resides behind the western edge of the main spiral galaxy. They also discover the tidal tail and the main spiral galaxy to be gas rich features. The tidal tail contains about one third of the total amount of gas in the system (Briggs et al., 2001) which is a normal result for a gas rich merger (e.g., Hibbard et al., 1994). The ACS Early Release Observations of the Tadpole were taken in 2002 in F475W, F606W, and F814W. These images were examined in detail by Tran et al. (2003); de Grijs et al. (2003). Tran et al. (2003) found over 40 young star clusters in the tidal tail with ages from 3-10 Myr. The most luminous star cluster has $M_V = -14.45$ and a half light radius of 161 pc indicating that it may be a SSC, however, at the distance of the Tadpole, it may also be a superposition of several star clusters or OB associations. This SSC has an age of $\sim 4 - 5$ Myr with a mass of $\sim 6.6 \times 10^5 \mathrm{M}_\odot$ and is likely to be unbound and will not survive to become a globular cluster. A long slit spectrum of the SSC was obtained with the Echellette Spectrograph and Imager on Keck II by Tran et al. (2003). This spectrum shows strong, narrow emission lines and an observed Balmer decrement of $\mathrm{H}\,\alpha/\mathrm{H}\,\beta = 2.76$, indicating little to no reddening at the position of the SSC. de Grijs et al. (2003) find about 8 bright young star clusters in the tidal tail. They also examine the Tadpole on a pixel by pixel basis that the area of the tidal tail is very blue and corresponds to colors on the Western edge of the spiral galaxy. They also estimate the dynamical age of the tail by comparing the length of the tail (~ 110 kpc) with a typical velocity dispersion in spiral galaxies (150-300 km s^{-1}) and estimate a dynamical age for the tail of the Tadpole as $t_{dyn} \sim 400 - 800$ Myr.

Jarrett et al. (2006) took advantage of the inclusion of the Tadpole in the ELAIS N1 field of the Spitzer Wide-Area Infrared Extragalactic Survey (SWIRE) and the multiwavelength data sets provided by this survey. They used ground-based optical, near-infrared, and Spitzer Space Telescope observations of the Tadpole to examine the star formation in the main spiral and the tidal tail. Their optical data

are images in $Ug'r'i'$ and optical spectroscopy of the nucleus and the SSC found previously. The ground-based near-infrared observations were in J and K_s and the Spitzer observations span from 2-70 μm. They find an estimated mean SFR of $\sim 2-4$ M$_\odot$ yr^{-1}. The mid-IR emission in the main spiral is in a ring morphology indicating that the Tadpole may be a collisional ring system that also has a tidal tail. While there is substantial star formation in the disk of the Tadpole, the nucleus is dominated by older stars with little star formation. There are several infrared-bright "hot spots" that have strong PAH emission in the disk outside the nucleus. In the tidal tail, they study two bright clumps: the previously mentioned SSC 1, also called J160616.85+552640.6, studied in detail by Tran et al. (2003), and the secondary clump SSC 2 further along the tail from the nucleus. The locations of both clumps show strong 24 μm emission. The SSC 1 location is the brighter one and has an estimated SFR of $\sim 0.1-0.4$ M$_\odot$ yr^{-1}which is about 10% or more of the total star formation in the merger. They estimate the mass of the SSC to be $\sim (1.4-1.6)\times 10^6$ M$_\odot$ using g' and K_s fluxes using a mass to light ratio for young clusters. Also, they quote a dynamical age of the Tadpole interaction to be ~ 150 Myr which is significantly less than that from de Grijs et al. (2003).

To determine the dynamical age of the Tadpole tidal tail for this paper, I take the HI velocity dispersion for the main spiral from Briggs et al. (2001) which is half of the total width of the velocity spread in the main spiral (~ 330 km s^{-1}). I measure the tail length to be 452 pixels which equals 190$''$ and using the adopted distance measurement of 134.2 Mpc, gives a tail length of 123.5 kpc. This gives a dynamical age of 123.5 kpc /330 km s^{-1}= 370 Myr.

This paper examines SFR and SFE in local regions of the tidal tail (~ 10 kpc) and in the tidal tail as a whole. Section 2 outlines the new Hα, CO, and HI observations and reductions. Results are presented in Section 3. Section 4 discusses the implications for star formation in tidal debris.

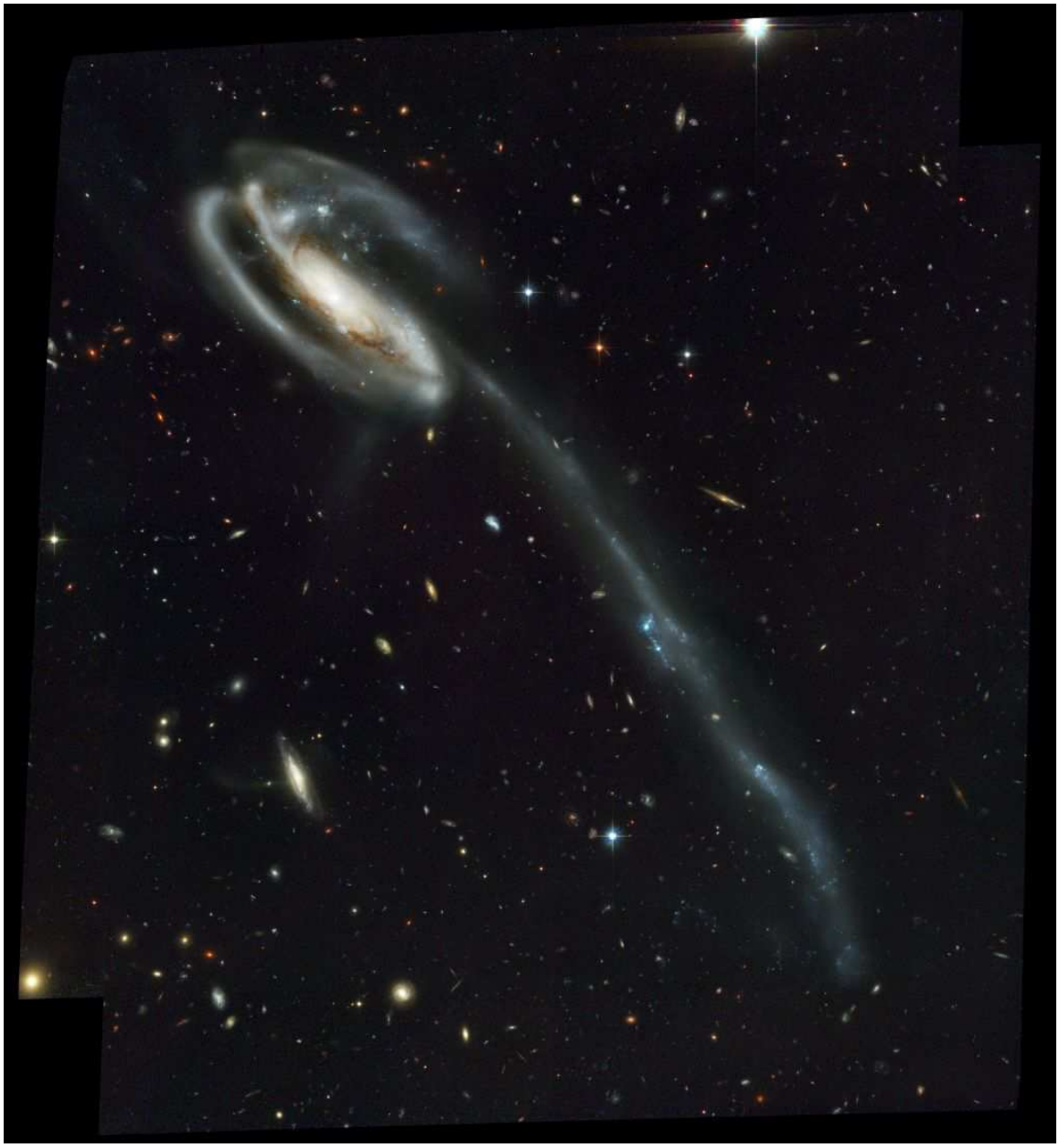

Figure 4.1: UGC 10214 ("The Tadpole") Hubble Space Telescope Advanced Camera for Surveys Early Release Observation 3 color image produced from F475W, F606W, and F814W images (Tran et al., 2003).

4.2 Observations and Reductions

To examine star formation on local scales of ~ 10 kpc and on global scales encompassing the entire tidal tail of the Tadpole galaxy, ground based Hα images were obtained. The resulting star formation rates are compared with the amount of gas available for star formation using CO and HI observations.

4.2.1 Hα Observations and Calibrations

Observations to obtain Hα images were taken with the Loral 2K CCD imager at the Lennon 1.8m VATT on Mount Graham, Arizona on May 22, 2004. This imager has a $6.4'$ field of view with $0.42''$ per pixel. Narrow-band Hα images were obtained at the VATT with an 88 mm Andover 3-cavity interference filter centered at 6780 Å. Integration times for the Hα images were 6×1200 s. To subtract continuum emission, this field was also observed with a Kron-Cousins R filter using integration times of 3×300 s. Images were reduced using standard IRAF[9] tasks.

To create images with only the emission lines, a scaled R band image was subtracted from narrowband image after alignment using foreground stars. To determine an initial scaling factor, the ratio of integration time for individual frames is multiplied by the ratio of filter widths. For this observation, the ratio of integration times is 4 (1200/300) and the ratio of filter widths is $0.068 = 81\text{Å}/1186.35\text{Å}$. This initial scaling factor then equals 0.272. I next determine the scaling factor by performing photometry of non-saturated stars in the Hα and R band images. By plotting the instrumental flux of both filters against each other (Figure 4.2), I determine a linear fit of $f(\mathrm{H}\alpha_{inst}) = 0.256 * f(R_{inst}) + 185.79$. The slope of this fit indicates the appropriate

[9]IRAF is distributed by the National Optical Astronomy Observatory, which is operated by the Association of Universities for Research in Astronomy, Inc., under cooperative agreement with the National Science Foundation.

scaling factor between the R and Hα images while the y-intercept indicates the offset between the images. I adopt the scaling factor from the ratio of stars in the image. The R band and continuum subtracted Hα images are shown in Figure 4.3.

For calibration of the Hα flux, spectrophotometric standard stars from the Oke (1990) catalog were observed. Aperture photometry of these standards was compared to their absolute magnitudes. Absolute magnitudes for each spectrophotometric standard star were calculated by integrating their spectral energy distribution over the filter response function. A standard atmospheric extinction coefficient of 0.08 mag airmass^{-1} was used (Lee, 2006). Zero points were calculated by comparing the absolute magnitude in each filter with the instrumental magnitude from aperture photometry. For each night, the zero points from all standards (in this case, 4) were averaged. These zero points had a standard deviation of 0.016 mag.

I also need to remove contamination from the [NII] doublet at λ6548,6583 in the Hα filter. In addition, emission line flux from the R filter needs to be removed.

The total flux equation (Equation A13 in Lee (2006)) is:

$$f_{tot}(H\alpha + [NII]) = \lambda^{-2} 10^{-0.4(ZP + 2.397 - \kappa sec(z))} FWHM_{NB} CR(H\alpha + [NII]) \left[T_{NB}(\lambda) - T_R(\lambda) \frac{t_R}{t_{NB}} \frac{1}{F} \right]^{-1} \quad (4.1)$$

λ: redshifted wavelength of Hα

ZP: zero point

κ: atmospheric extinction coefficient (I use 0.08 mag airmass^{-1})

$FWHM_{NB}$: width of narrowband filter in Å

$CR(H\alpha + [NII])$: count rate in continuum subtracted image

T_R: Transmission correction in R. Calculated by an average of normalized

transmissions at each redshifted wavelength of Hα and [NII] lines, weighted by their relative line fluxes.

T_{NB}: Transmission correction for narrowband filter. Calculated by an average of normalized transmissions at each redshifted wavelength of Hα and [NII] lines, weighted by their relative line fluxes.

t_R: exposure time in R band filter

t_{NB}: exposure time in narrowband filter

F: scale factor applied to R band continuum image when subtracting it from narrowband image.

T_{NB} is ideally be calculated by measuring the line ratios of Hα and [NII] lines directly from spectroscopy. Jarrett et al. (2006) has an optical spectra of the brightest tidal tail region from the Hale 200 inch, but it does not have sufficient resolution to distinguish [NII] from Hα. However, the Tran et al. (2003) reports that their Keck spectrum gives a line ratio of [NII]6583/H$\alpha = 0.0705$. Since the ratio of [NII]6583/[NII]6548 = 3, this observation indicates a total [NII]/H$\alpha = 0.094$. I adopt this value to subtract the flux of the [NII] lines, giving a resulting flux that contains only that of Hα.

4.2.2 CO(1–0) and CO(2–1) Observations

I observed the CO(1–0) and CO(2–1) at their redshifted frequencies between August and October 2005 with the IRAM 30-meter telescope on Pico Veleta. I observed the tidal tails at positions centered at RA 16:06:15.5, Dec 55:25:47 and RA 16:06:20.2, Dec 55:25:56 Dual polarization receivers were used at both frequencies with the 512 $\times$ 1 MHz filterbanks on the CO(1–0) line and the 256 $\times$ 4 MHz filterbanks on the CO(2–1). The observations were done in wobbler switching mode with a wobbler throw of 200$''$ in azimuthal direction. Pointing was monitored on nearby quasars every 60–90 minutes. During the observation period, the weather conditions were

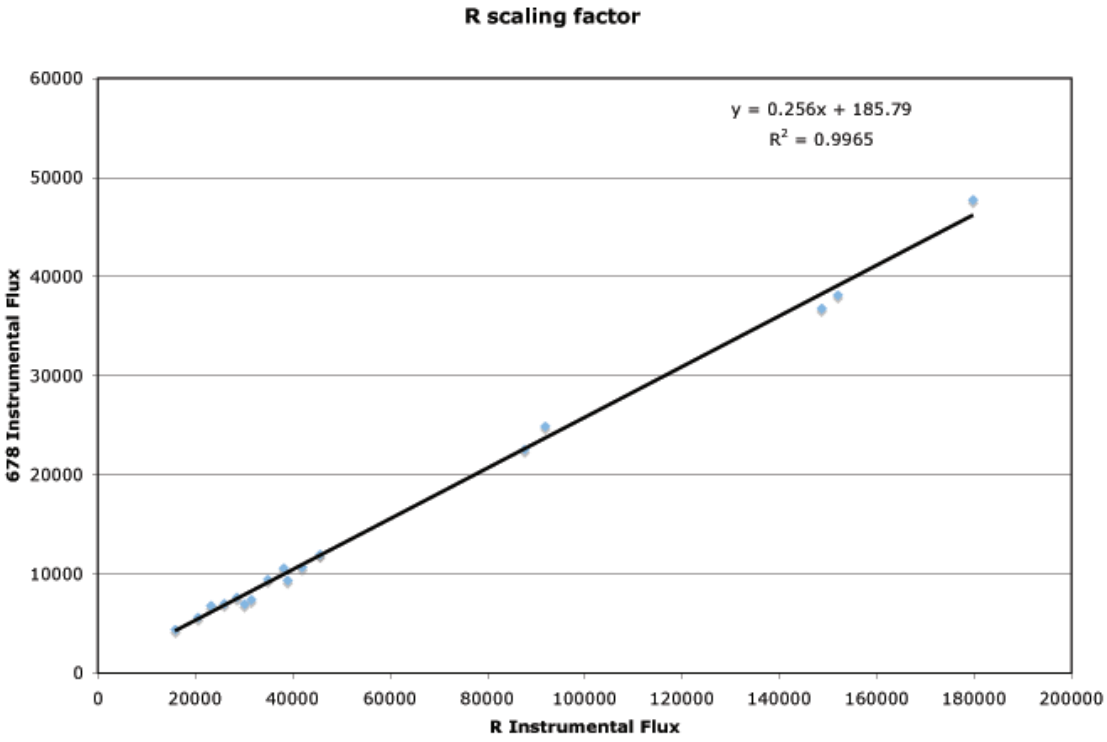

Figure 4.2: Photometry of non-saturated, isolated stars in the R and narrowband Hα images plotted as instrumental flux. The slope of the fitted line indicates the scaling factor between the R and Hα images and the y-intercept indicates the offset.

generally good (with pointing better than 4 $''$), The average system temperatures was $\sim$200 K at 115 GHz and $\sim$420 K at 230 GHz on the T_A^* scale. At 115 GHz (230 GHz), the the IRAM forward efficiency, F_{eff}, was 0.95 (0.90), the beam efficiency, B_{eff}, was 0.75 (0.54), and the half-power beam size is 21$''$. All CO spectra and luminosities are presented on the main beam temperature scale (T_{mb}) which is defined as $T_{mb} = (F_{eff}/B_{eff}) \times T_A^*$. For the data reduction, I selected the observations with a good quality (taken during satisfactory weather condition and showing a flat baseline) and summed the spectra over the individual positions and subtracted a baseline which was a constant continuum level for the CO(1–0) spectra and a linear baseline for the CO(2–1) data.

I smoothed the spectra by averaging 4 adjacent channels to a velocity

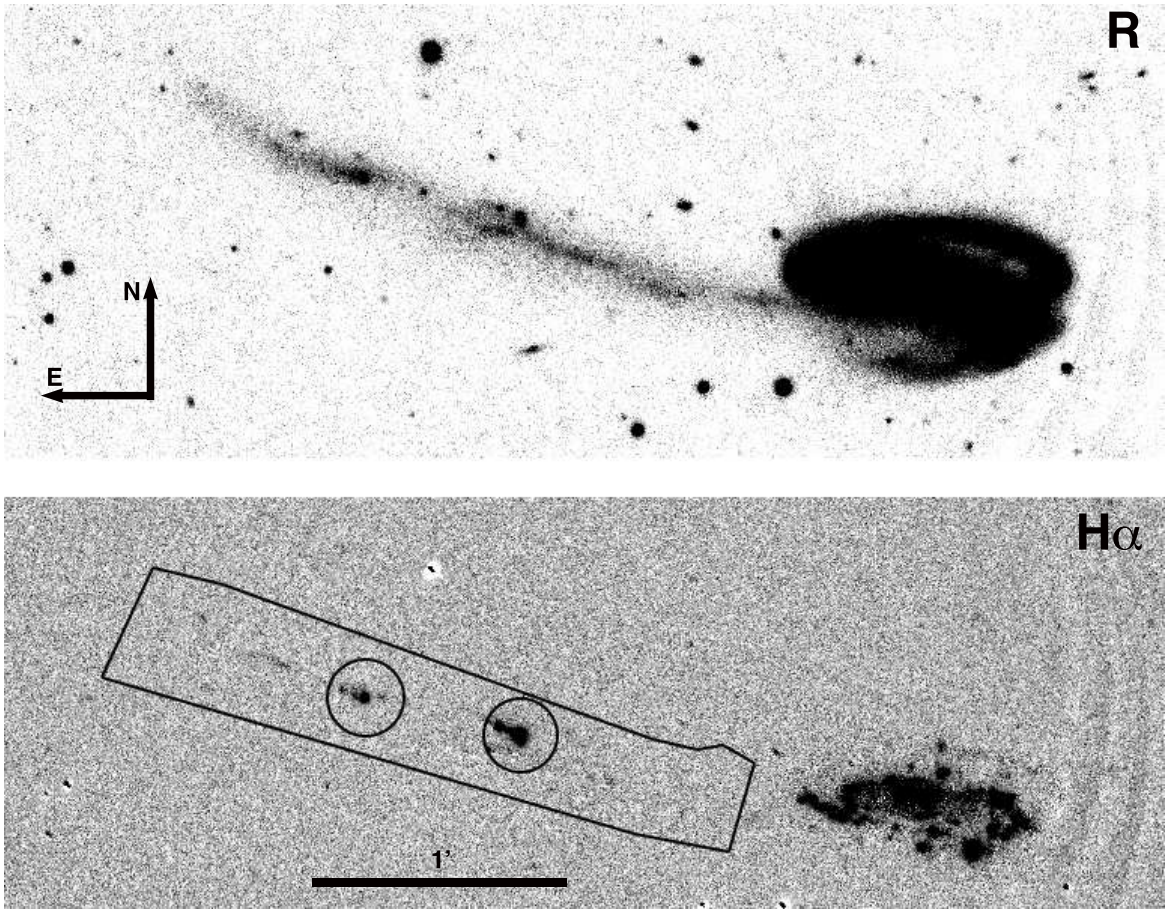

Figure 4.3: Images of UGC 10214 ("The Tadpole") taken with the 1.8m VATT. Upper: R band image with an integration time of 300 s. Lower: Continuum subtracted image showing Hα emission throughout the inner region of the main galaxy and in several knots along the tidal tail stretching to the east. The circles indicate the 21″ beamsize and positions of the IRAM CO(1-0) observations. The polygon indicates the region of the tidal tail used to determine the total Hα flux in the tail.

resolution of 10.7 km s^{-1}. I then determined the upper limit as:

$$I_{CO} < 3 \times rms \times \sqrt{\delta V \ \Delta V}, \tag{4.2}$$

where δV is the channel width and ΔV the total line width based on the observed FWHM of the HI spectral line extracted at the location of the source (see next section).

4.2.3 HI Observations

UGC 10214 was observed with the VLA C array (with a FWHM beam of 15″) on March 1, 2004. The total on-source time was 9 hours. Observations were made with the 21 cm mode tuned to a heliocentric wavelength of 9420 km/s. The narrowband correlator mode was chosen to correspond to a bandwidth of 1.56 MHz with 63 channels and a spacing of 5.3 km/s. The wide band correlator mode was chosen to correspond to a bandwidth of 6.25 MHz with 15 channels and a spacing of 88 km/s. The phase calibrator was $1634 + 627$ and the flux calibrator was $1331 + 305$.

The data were reduced using standard reduction procedures in the Astronomical Image Processing System (AIPS) (e.g., Greisen, 2003). Maps were made of the narrowband and wideband data with both natural and uniform weighting. Natural weighting provides even weighting of the uv plane and is sensitive to diffuse emission. Uniform weighting down plays the well sampled inner parts of the uv plane, emphasizing long baselines and provides better resolution. For the narrowband maps, the natural weighting produced a final beam size of $16.1'' \times 15.5''$ with a rms noise of 0.40553 mJy beam^{-1} channel^{-1}. The uniform weighting produced a final beam size of $12.8'' \times 12.5''$ with a rms of 0.56852 Jy beam^{-1} channel^{-1}. The maps were made with $4''$ pixel^{-1} and a size of 512×512. For this paper, I use the natural weighting as it is more sensitive to the diffuse emission in the tail. Since the narrowband map is not line free, the continuum subtraction was done in the image plane using different image cubes for the line-free channels.

This produced FITS cubes with x and y pixels corresponding to the RA and DEC of the image and third dimension slices for each velocity channel. Each pixel in each channel has an associated flux density in units of Jy beam^{-1}. These FITS cubes were used with IDL scripts for extraction of spectra and calculating column

densities and HI mass. Spectra of each SSC were extracted using a circular aperture with a diameter of 21″ and 11″ to match the beam sizes of the CO(1-0) and CO(2-1) observations.

To calculate the mass of neutral hydrogen in the aperture, I calculate the total the HI flux, S_i, and the average HI flux, $\langle S \rangle_i$, in the selected region for each channel. I then multiply this total flux in the region, S_i, by the channel width dv[km s^{-1}] to get the total HI flux in the region (F_i in Jy beam^{-1} km s^{-1}). I then sum the total HI flux over all channels with HI emission:

$$F = \sum_{n_{chan}} F_i \tag{4.3}$$

where n_{chan} is the number of channels with HI emission. To determine which channels had HI emission, I selected channels with greater than 1 rms above zero. I did not want to select any channels with flux density less than zero which would bias our results to lower fluxes. To convert the units of F from Jy beam^{-1} km s^{-1} to Jy km s^{-1}, I multiply by the ratio of the pixel size in square arcseconds to the beam size in square arcseconds (A_{pix}/A_{beam}). The error on this quantity is:

$$\sigma_F = \sqrt{n_{chan}}\sqrt{n_{pix}}\sigma_{1pix} dv A_{pix}/A_{beam} \tag{4.4}$$

Using the equations in Mullan et al. (2013), the HI mass in this selected region is then:

$$M_{HI}[M_\odot] = 2.36 \times 10^5 (D[Mpc])^2 * F \tag{4.5}$$

where M_{HI} is the HI mass in solar masses and D is the distance to the Tadpole in Mpc and F is in Jy km s^{-1}. The error on M_{HI} is

$$\sigma_{M_{HI}} = 2.36 \times 10^5 D \sqrt{D^2 \sigma_F^2 + F^2 \sigma_D^2} \tag{4.6}$$

where σ_D is the error in the distance measurement.

The average column density was calculated using the mean flux for each channel ($\langle S \rangle_i$) and converting it to a column density (Mullan et al., 2013).

$$N_{HI}[cm^{-2}] = 1.82 \times 10^{18} * 684977.24 * \sum_{n_{chan}} \langle S \rangle_i dv / A_{beam} \tag{4.7}$$

with an error of

$$\sigma_{N_{HI}} = 1.82 \times 10^{18} * 684977.24 * \sqrt{n_{chan}} \sigma_{1pix} dv / (A_{beam} \sqrt{n_{pix}}) \tag{4.8}$$

A contour map of integrated column density was also created by using equations 4.7 and 4.8 with $\langle S \rangle_i$ equal to the flux density value of the individual pixel for each channel and n_{pix} equal to 1 pixel. For the contour map, I integrate from channels 25-50 (or a velocity width of 137 km s^{-1}).

4.3 Results

I now examine the star formation tracer, Hα, in the tidal tail of the Tadpole. The local and global SFR are compared to the properties of the gas available for star formation in the tidal tail based on molecular gas measurements from CO(1-0) and CO(2-1) and neutral hydrogen gas measurements from the 21 cm HI line.

4.3.1 HII regions in the Tidal Tail

As shown in Figure 4.3, the tidal tail of UGC 10214 is host to multiple Hα emission regions. These regions are arranged in two bright clumps, corresponding to the

bright, blue regions in the tidal tail also examined as SSC 1 and SSC2 in Jarrett et al. (2006). In the HST/ACS images in Tran et al. (2003) (see Figure 4.4), the two bright clumps break up into multiple star clusters also found by de Grijs et al. (2003). Outside of these two bright regions, there are a few modest amounts of Hα emission, also corresponding to bright blue regions. In the bottom panel of Figure 4.4, I identify and label the 5 HII regions studied here. The labels of SSC 1 and SSC 2 are from Jarrett et al. (2006), but I also label other smaller clumps of Hα emission with letter designations. SSC 1 is in a U-shaped structure in the HST/ACS images which has a brighter northern arm. Our Hα image shows this bright northern arm to host two bright HII regions, SSC 1 and 1a, which correspond in position to the two brightest star clusters in the arm. SSC 1 shows an oval shape, which the HST image shows to be due to a fainter blue star cluster to the south. In the southern arm of the U, there is an Hα peak, labeled 1b, at the location of a blue star cluster. The Hα image shows a bright peak at at the location of SSC2 with a fainter peak to the east, labeled as 2a.

I first examine the Hα emission in the tidal tail by looking at each HII region using an aperture with a diameter of 6″ which corresponds to a size of 3.9 kpc at the distance of the Tadpole. I also extract the emission from Hα using aperture sizes more closely matched to that of the molecular gas observations (12″ and 21″). Our detection limit for the Hα image is found by taking 5 times the standard deviation of the sky background which is 7.06 counts, corresponding to a luminosity of 3.9×10^{36} erg s^{-1}. Table 4.1 lists the location, area of the aperture in kpc^2, $L_{H\alpha}$, SFR(Hα) from Kennicutt (1998b), and the star formation rate surface density, $\Sigma_{SFR}(H\alpha)$ in $M_\odot$ yr^{-1} kpc^{-2}.

On 4 kiloparsec scales (from the 6″ aperture), the brightest HII region is SSC 1 with a $L_{H\alpha} = 5.3 \pm 0.7 \times 10^{40}$ erg s^{-1} which is four times brighter than either regions 1a or 2. Using the SFR formulation from Kennicutt (1998b), this SSC 1 has

a SFR of 0.41 $M_\odot$ yr^{-1}. Taking the SFR along with the area of the aperture (11.97 kpc^2), I find $\Sigma_{SFR}(H\alpha) = 0.035 \pm 0.004$ $M_\odot$ yr^{-1} kpc^{-2}. These HII regions in the tidal tail of UGC 10214 are brighter than the HII regions of either tidal tail of NGC 2782 (Knierman et al., 2012, 2013). In particular, SSC 1 is 27 times more luminous than W235 in the Western Tail of NGC 2782. SSC 1 is as luminous as the brightest HII regions in Sc galaxies ($L_{H\alpha} \sim 10^{40}$ erg s^{-1}).

On 8 kpc scales, (from the 12″ aperture), I now examine only the SSC 1 and SSC 2 locations. For this aperture, $L_{H\alpha} = 6.7 \times 10^{40}$ erg s^{-1} in SSC 1 which is 3.7 times brighter than $L_{H\alpha}$ in SSC 2. The SFR in SSC 1 at 0.53 $M_\odot$ yr^{-1} is also almost 4 times the rate in SSC 2 (0.14 $M_\odot$ yr^{-1}). This is also the scale that was observed by Jarrett et al. (2006) in their examination of SSC 1 and SSC 2. Jarrett et al. (2006) estimates the SFR in SSC 1 at 0.23 $M_\odot$ yr^{-1}using the integrated Hα line flux from their optical spectroscopy. This value is more than half the SFR I determine based on our 12″ aperture, and it is also less than the SFR from our 6″ aperture. The Hα measurement from Jarrett et al. (2006) was made using a long slit optical spectra with a slit width of 1.5″ under poor seeing conditions (3″-4″) so they may have missed a portion of the Hα emission which I recover in our narrow band observations.

On 14 kpc scales (from the 21″ aperture), I also examine only the SSC 1 and SSC 2 locations which now encompass the majority of the Hα emission in their regions of the tail. For this aperture, $L_{H\alpha} = 8.2 \times 10^{40}$ erg s^{-1} in SSC 1 which is 3.7 times brighter than SSC 2. The SFR in SSC 1 is 0.65 $M_\odot$ $yr^{-1}$and is 3.8 times the value for SSC 2 (0.17 $M_\odot$ yr^{-1}).

On the global scale, I sum the flux in the polygonal aperture encompassing the tail (see Figure 4.3). For the entire tidal tail, I find $L_{H\alpha} = 1.6 \pm 0.2 \times 10^{41}$ erg s^{-1} and a SFR of 1.3 $M_\odot$ yr^{-1}. This tidal tail has a SFR 56 times that of the entire

Eastern tidal tail of NGC 2782 and 87 times that of the Western tail of NGC 2782. Smith et al. (1999) lists the $L_{\mathrm{H}\alpha}$ for several tidal debris regions in different mergers which range from $< 1.6 \times 10^{39}$ erg s^{-1} in NGC 4438 to 1.1×10^{40} erg s^{-1} in NGC 4676 ("The Mice"). $L_{\mathrm{H}\alpha}$ in these other tidal debris regions are lower than the $L_{\mathrm{H}\alpha}$ in the Tadpole tidal tail. By comparison, the SFR in the Tadpole tail is similar to the SFR for the entire Milky Way galaxy ($1.9 \pm 0.4 \mathrm{M}_{\odot}$ yr^{-1}; Chomiuk & Povich, 2011), which indicates that the Tadpole tidal tail is forming a larger amount of stars than is seen in other tidal tails as referenced above.

4.3.2 Molecular Gas - CO(1-0) and CO(2-1)

SSC 1 was observed with IRAM to an rms of 1.51 mK in CO(1-0) and to an rms of 2.33 mK in CO(2-1) , however no detections in either line were observed. The spectrum for these observations are shown in Figure 4.5) and Figure 4.6 where T_{mb} is plotted versus velocity offset from the heliocentric velocity of the Tadpole. Similarly, no detections for SSC 2 were made in either CO(1-0) (rms = 1.70 mK, Figure 4.7) or CO(2-1) (rms = 3.45 mK, Figure 4.8).

Using the equations in Braine et al. (2001), I find that the molecular mass is:

$$M_{mol}[M_{\odot}] = 1.36 I_{CO} X_{CO} D^2 \Omega 2 m_p \tag{4.9}$$

where I_{CO} is the average CO line intensity expressed in km s^{-1}, X_{CO} is the conversion factor between CO and H_2 (the Milky Way conversion factor is used here for consistency with prior work, see Section 4.4.5 for discussion of a different X_{CO}), D is the distance, Ω is the solid angle which the source is average over (for a Gaussian beam with θ_{FWHM} as the half power beam width ($\Omega = 1.13\theta^2_{FWHM}$), and m_p is the mass of a proton. Since I do not have a detection of CO(1-0) or CO(2-1), I use Equation 4.2 to determine the upper limit for I_{CO}. The CO(2-1) line is a higher

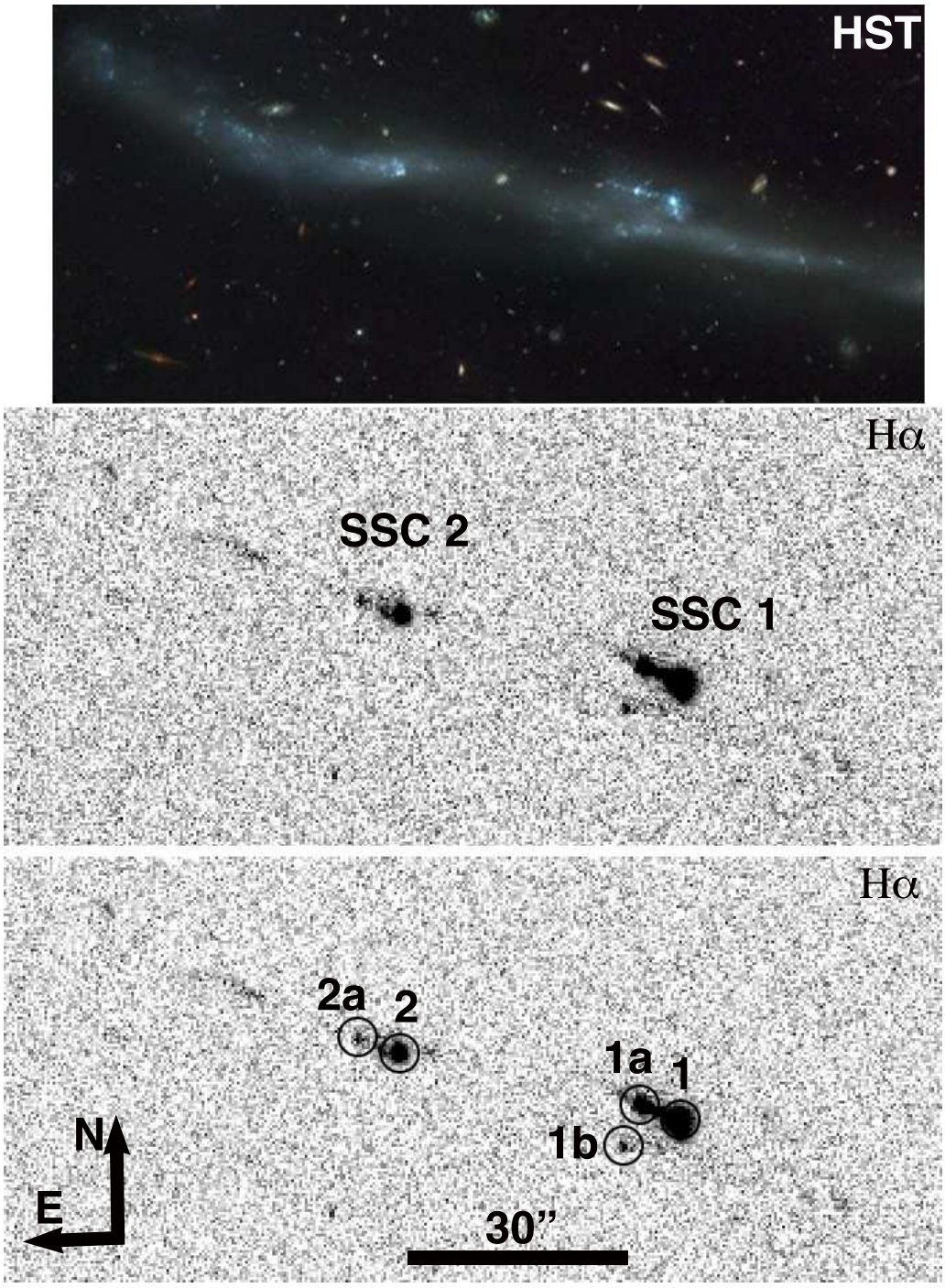

Figure 4.4: Close up of Tadpole eastern tidal tail region. Top: Tidal tail taken from HST/ACS Early Release Observation 3 color image produced from F475W, F606W, and F814W images. Center: Tidal tail from continuum subtracted Hα image as in Figure 4.3 with SSC 1 and SSC 2 labeled. Bottom: As in Center image with circles with 6″ apertures with labels.

Table 4.1: Properties of $H\alpha$ sources in Tidal Tail of Tadpole

Location	Area kpc^2	$L_{H\alpha}$ 10^{39}erg s^{-1}	SFR($H\alpha$) $M_\odot$ yr^{-1}	$\Sigma_{SFR}(H\alpha)$ 10^{-3} $M_\odot$ yr^{-1} kpc^{-2}
1	11.97	53(7)	0.41(0.06)	35(4)
1a	11.97	14(2)	0.11(0.02)	9(1)
1b	11.97	2.1(0.4)	0.017(0.003)	1.4(0.3)
2	11.97	13(2)	0.10(0.01)	8(1)
2a	11.97	2.9(0.5)	0.022(0.004)	1.9(0.3)
1	47.87	67(9)	0.53(0.07)	11(2)
2	47.87	18(3)	0.14(0.02)	2.9(0.4)
1	146.6	82(1)	0.65(0.09)	4.4(0.6)
2	146.6	22(4)	0.17(0.03)	1.1(0.1)
Tail	2318	160(20)	1.3(0.2)	0.54(0.08)

excitation line and probes a warmer gas. Braine et al. (2001) uses CO(2-1) observations for molecular gas in the tidal dwarf galaxies of NGC 7252W and NGC 4038W. For these measurements, they use the intrinsic line ratio of $CO(2-1)/CO(1-0) = 0.75$ to obtain a molecular mass and I use the same ratio here. Table 4.2 lists the location, the limit for I_{CO}, M_{mol}, FWHM of of the HI measured in the same aperture size as the CO beam, the velocity width Δv of the HI, N_{HI}, M_{HI}, and the total gas mass M_{gas}, for the two SSCs and the total tidal tail area.

From the CO(1-0) observations, the upper limit on the molecular gas mass for SSC 1 is $M_{mol} < 1.06 \times 10^8$ $M_\odot$ and is lower by a factor of 0.96 than the upper limit for SSC 2 ($M_{mol} < 1.09 \times 10^8$ $M_\odot$). The molecular gas mass upper limits from CO(1-0) are higher by a factor of 1.8 and 1.3 than the CO(2-1) upper limits for SSC 1 and SSC2. This is likely due to the smaller beam size of the CO(2-1) observations in spite of their higher rms values. The upper limits for the molecular mass from the CO(2-1) observations are $M_{mol} < 6.0 \times 10^7$ $M_\odot$ for SSC 1 and $M_{mol} < 8.1 \times 10^7$ $M_\odot$ for SSC 2. By summing the upper limits for the molecular gas mass, I estimate an upper limit for the entire tidal tail to be $M_{mol} < 2.15 \times 10^8$ $M_\odot$.

Table 4.2: Molecular and HI Gas in Tadpole Tidal Tail Locations

Location	I_{CO} K km s^{-1}	M$_{mol}$ 10^8 M$_\odot$	FWHM km s^{-1}	Δv km s^{-1}	$\langle N_{\rm HI}\rangle$ 10^{21}cm^{-2}	N_{HI} 10^{21}cm^{-2}	M$_{HI}$ 10^8M$_\odot$	M$_{gas}$ 10^8M$_\odot$
CO(1-0) 21″								
SSC1	< 0.115	< 1.06	60	82.2	0.73(0.01)	6.56(0.01)	3.6(0.3)	< 6.00
SSC2	< 0.118	< 1.09	50	60.3	0.65(0.01)	5.85(0.01)	3.2(0.2)	< 5.44
CO(2-1) 12″								
SSC1	< 0.178	< 0.60	60	82.2	0.76(0.02)	3.78(0.02)	2.1(0.2)	< 3.45
SSC2	< 0.240	< 0.81	50	60.3	0.66(0.02)	3.31(0.02)	1.8(0.1)	< 3.26
Tail		< 2.15	60	109.6	0.120(0.001)	164.0(0.1)	90(6)	< 125

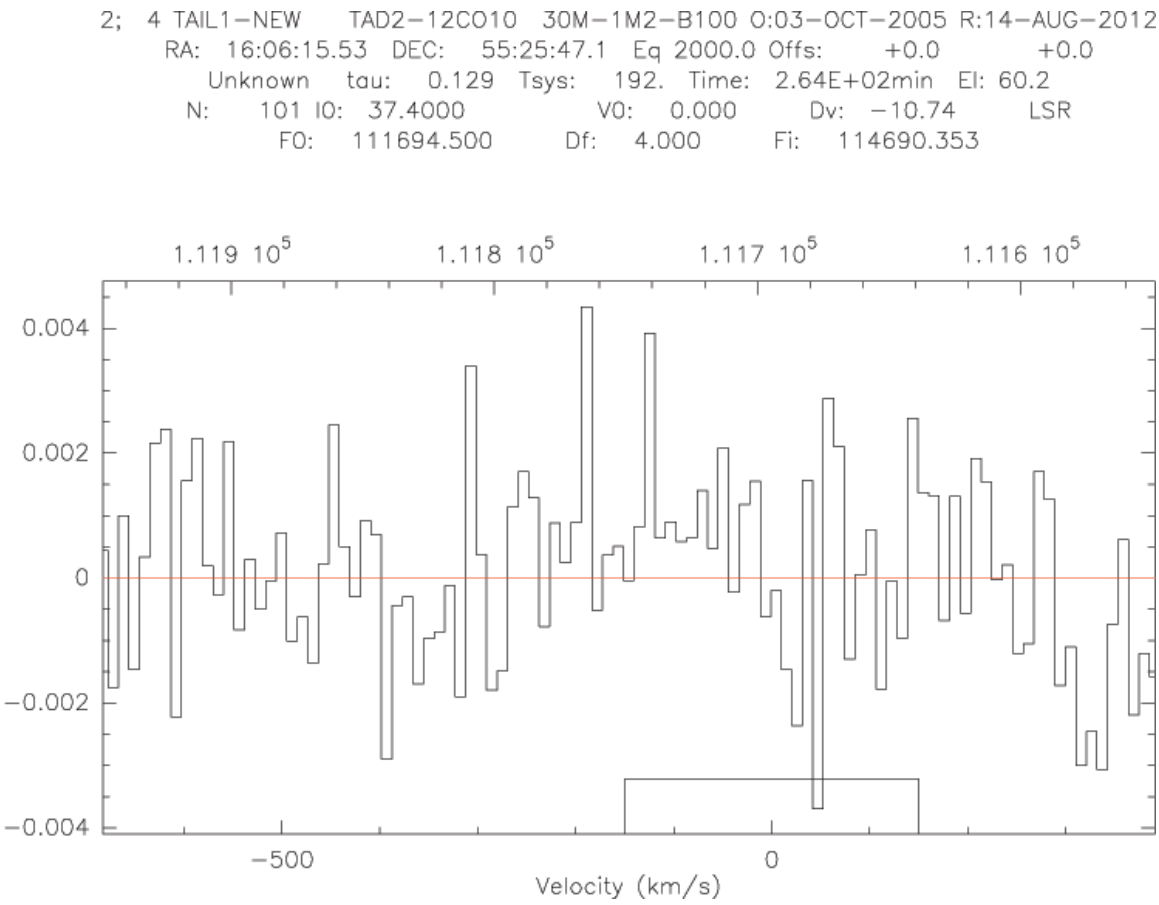

Figure 4.5: Spectrum of CO(1-0) taken with IRAM at the location of SSC 1.

The upper limits for molecular mass in the Tadpole tidal tail are one third lower than the observed molecular gas mass for clouds in the Eastern tail of NGC 2782 ($M_{mol} = 3.69 \pm 0.09 \times 10^8$ $M_\odot$, from K13). Even with the difference in beam sizes and distances between the two observations, the two observations are probing similar size molecular clouds. The beam size of the 12 meter Kitt Peak telescope is 55″ and at the distance of NGC 2782, this is probing about 10 kpc diameter clouds. With IRAM, the CO(1-0) observations are probing about 13 kpc sized clouds at the distance of the Tadpole. In the Eastern tail of NGC 2782, the molecular gas spanned a larger area than a single beam, so there is likely to not be a molecular cloud of similar size in the area of SSC 1 even with the great difference in distances between the galaxies.

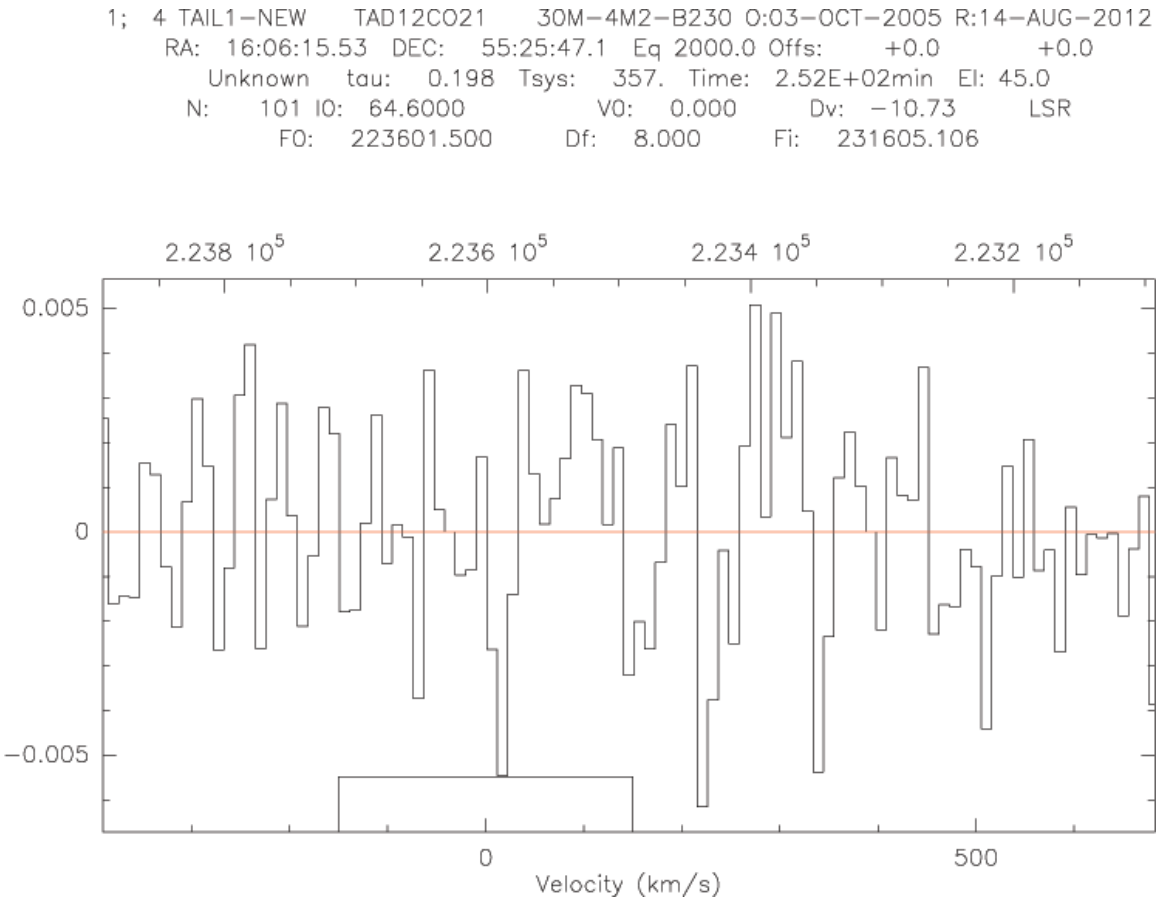

Figure 4.6: Spectrum of CO(2-1) taken with IRAM at the location of SSC 1.

4.3.3 21 cm HI

The VLA 21cm observations of the Tadpole reveal similar features to the findings of Briggs et al. (2001): the main spiral galaxy, the dwarf galaxy, and the tidal tail. I examine the tidal tail in detail here. An integrated column density map was created as above and is shown in Figure 4.9. As from equation 8, $\sigma_{N_{HI}} = 5.0 \times 10^{19}$ cm^{-2}. The contour map indicates the 5σ level of the map with the outer contour which gives a broad outline of the tidal tail region and the main spiral. A small gap is present in this map between the main spiral and the tidal tail and may just be indicative of the lack of gas at the velocities included in the map since I only integrated over velocities found in the tidal tail. In the tidal tail, there is evidence of

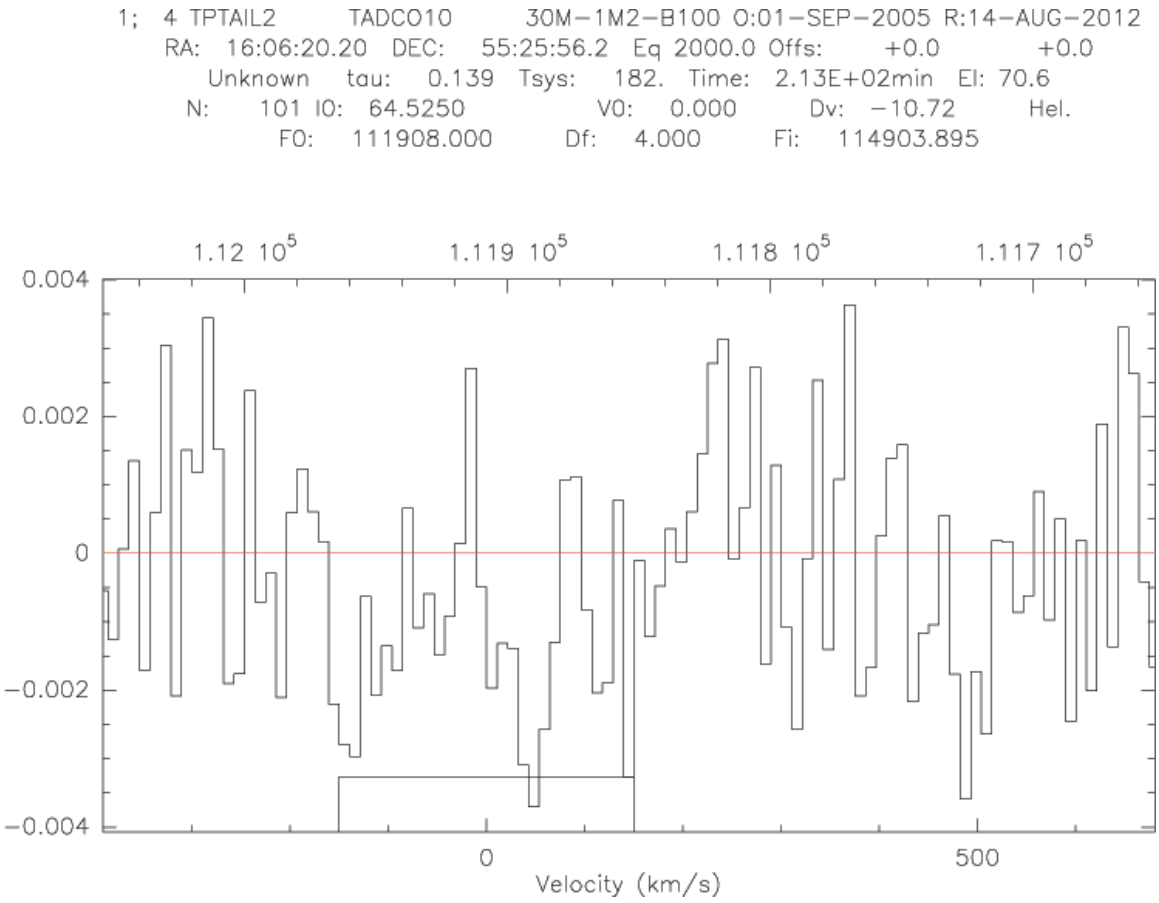

Figure 4.7: Spectrum of CO(1-0) taken with IRAM at the location of SSC 2.

two massive HI clumps. The HI clump closest to the spiral galaxy is coincident with SSC 1, while SSC 2 is at the western end of the HI clump farther to the east.

Integral spectra of HI were extracted at the locations of the two SSCs, indicated by dashed circles in Figure 4.9. The flux density in Jy beam^{-1} are plotted against the heliocentric velocity for summed pixels in the region as stated above. I plot the HI spectra from a 21″ sized aperture at the location of SSC 1 in Figure 4.10 . This shows a strong line with a fairly symmetric profile with a velocity width of 76.7 km s^{-1}. Figure 4.11 shows the integrated HI spectrum of SSC 2. This spectrum has an asymmetric profile with a velocity width of 82.2 km s^{-1}.

Table 4.2 lists the FWHM, velocity width (full width at zero intensity),

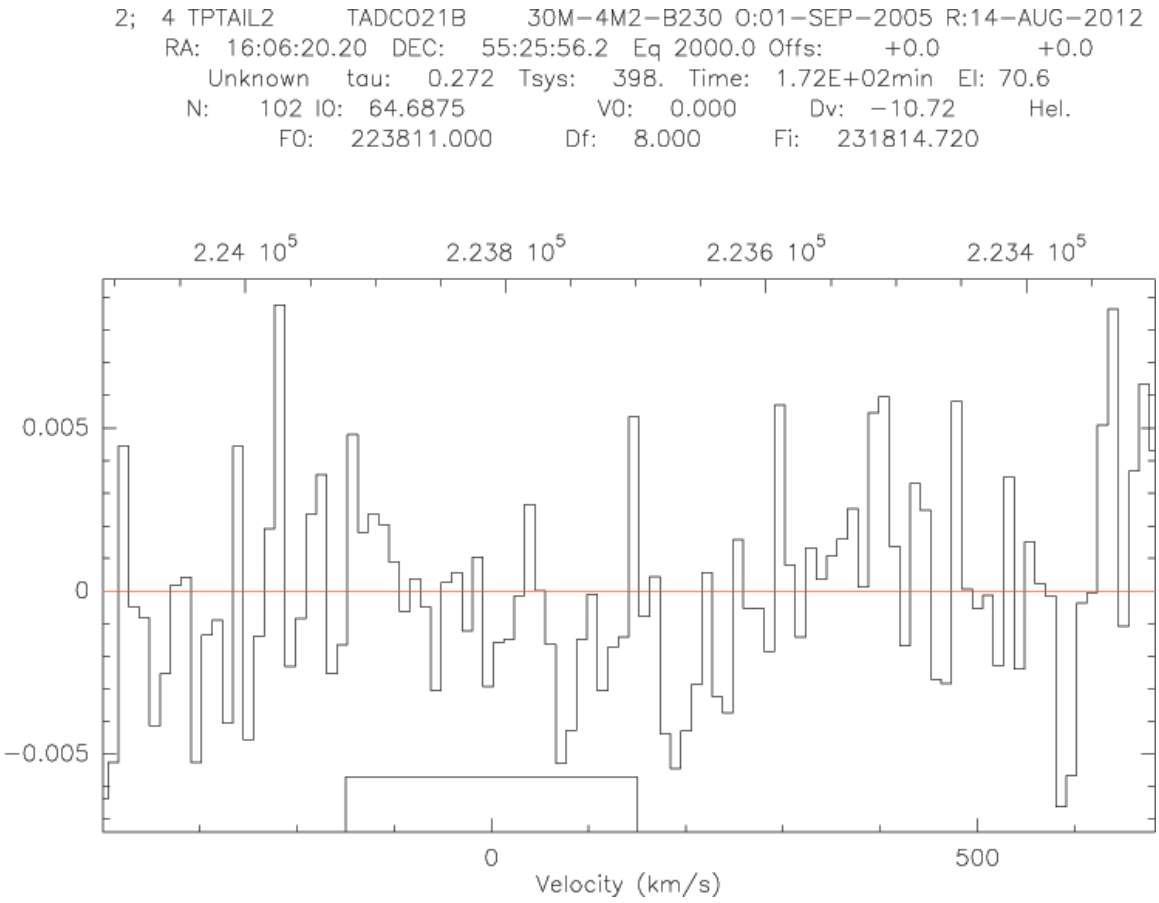

Figure 4.8: Spectrum of CO(2-1) taken with IRAM at the location of SSC 2.

average column density of HI, total column density of HI, N_{HI}, and total HI mass for a 21″ aperture and for a 11″ aperture for SSC 1, SSC 2 and the total area of the tidal tail. The average column densities at the location of SSC 1 and 2 range from $6.5 - 7.6 \times 10^{20}$ cm^{-2}. These values are larger than the threshold for finding significant amounts of star clusters in tidal tails of major mergers ($10^{20.6}$ cm^{-2} (Maybhate et al., 2007)). The range of M_{HI} for SSC 1 and SSC 2 are $3.2 - 3.6 \times 10^8$ $M_\odot$ which are similar to the HI masses in the Eastern tidal tail of NGC 2782, but a few times larger than the Western tail HI clumps of NGC 2782 which are around 10^8 $M_\odot$.

I also sum the HI flux density over the entire area of the tidal tail using a box around the tail. Figure 4.12 shows the integrated HI spectrum of the tail area.

This shows a broader spectral component with a narrow peaked component. The velocity width of the entire line is 109.6 km s^{-1}. The narrow peaked region may correspond to the narrow peak at 9401 km s^{-1} seen in single dish HI measurements by Briggs et al. (2001). The average column density in the tidal tail is 1.2×10^{20} cm^{-2} which is lower than the threshold from Maybhate et al. (2007), but not surprising since the tail is a large feature with only a few localized sites of star formation. The total amount of HI mass in the tidal tail is $9 \times 10^9 M_\odot$ which is higher than that observed in the single dish observations by Briggs et al. (2001).

4.3.4 Metallicity

Knowing the metallicity of the material in the tidal tail has implications for many of the derived properties such as the SFR and the CO to H_2 conversion factor. There are many different methods to estimate metallicity, but this section focuses on methods using optical emission line spectra taken by Tran et al. (2003) and Jarrett et al. (2006). Methods to estimate metallicity using optical emission lines trace the abundance of heavy elements, particularly oxygen, in the gas phase (see Kewley & Dopita, 2002, for a review of these methods).

The first method used to estimate metallicity in the tidal tail of the Tadpole is the ratio of the emission line intensity of [NII] to Hα. In Figure 9 of van Zee et al. (1998), an empirical relation is shown between these values as:

$$12 + \log(O/H) = 1.02 \log([NII]/H\alpha) + 9.36. \quad (4.10)$$

For a [NII]/H$\alpha = 0.094$ (from above, based on the spectrum from Tran et al. (2003)), SSC 1 has $12 + \log(O/H) = 8.3$. This metallicity, based on oxygen abundance, is converted to a more generalized metallicity through

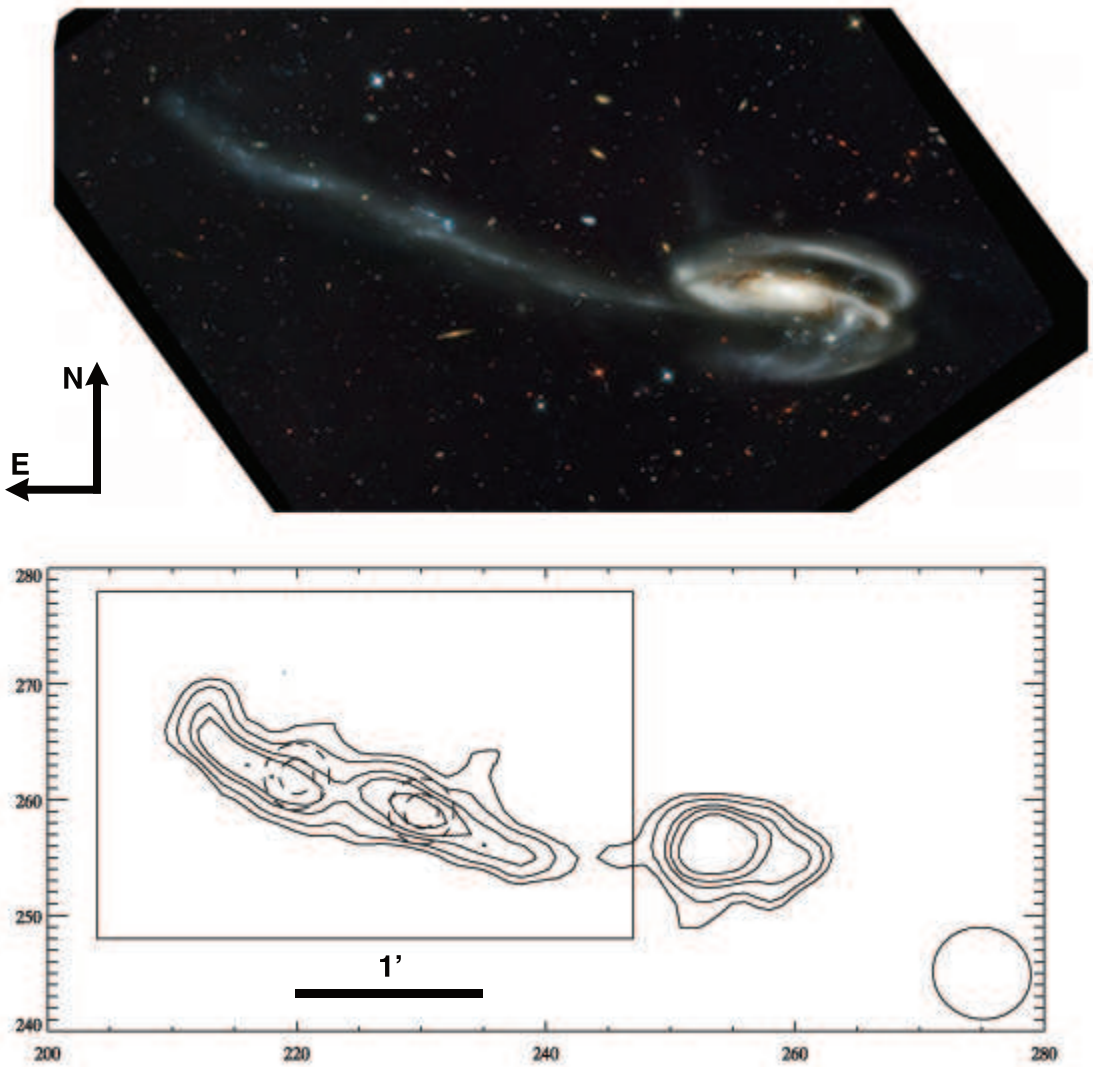

Figure 4.9: Top: This image shows the HST/ACS image of the Tadpole. Bottom: This image shows the 21 cm HI integrated column density contours for the velocity range from 9321-9458 km s^{-1}. This range only includes the velocity width of the tidal tail, but some HI from the main spiral galaxy is included as well. The contour levels are: 2.5, 3.5, 5.0, 5.6, and 7.5×10^{20} H atoms cm^{-2}. The dashed circles indicate the location of the extracted HI spectra with 11″ and 21″ apertures. The box indicates the area used for the global HI emission from the entire tidal tail. The solid circle indicates the beam size of the HI map.

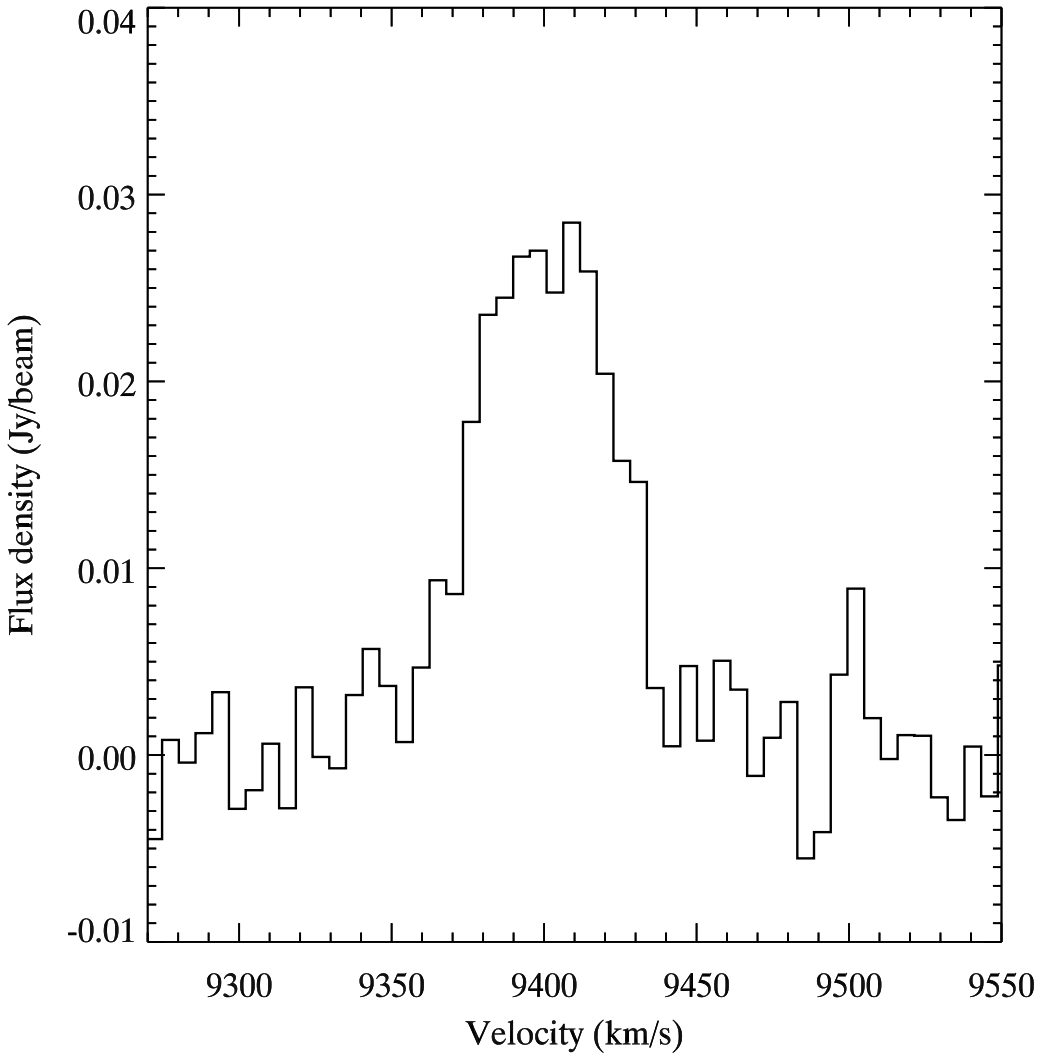

Figure 4.10: Extracted 21 cm HI spectrum at the location of SSC 1 using a 21″ aperture.

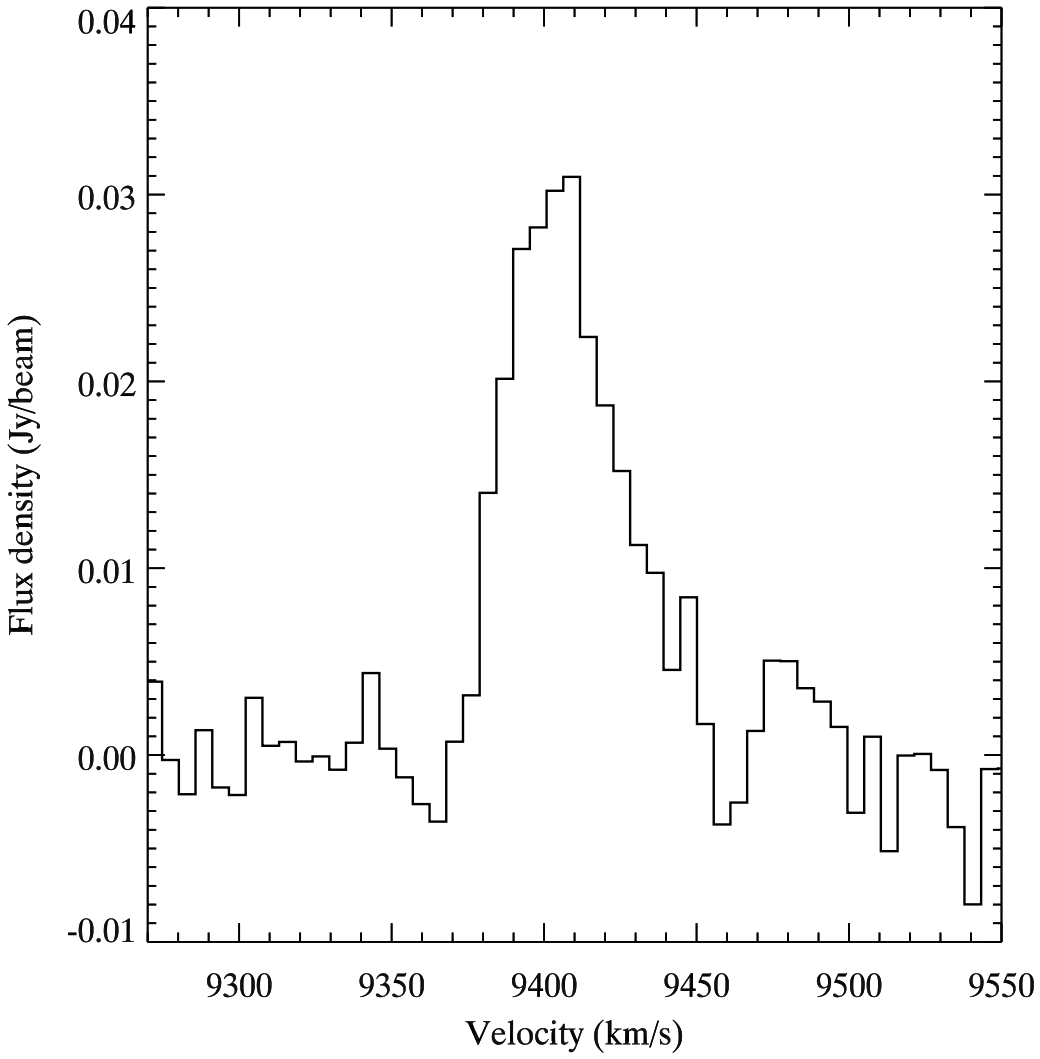

Figure 4.11: Extracted 21 cm HI spectrum at the location of SSC 2 using a 21″ aperture.

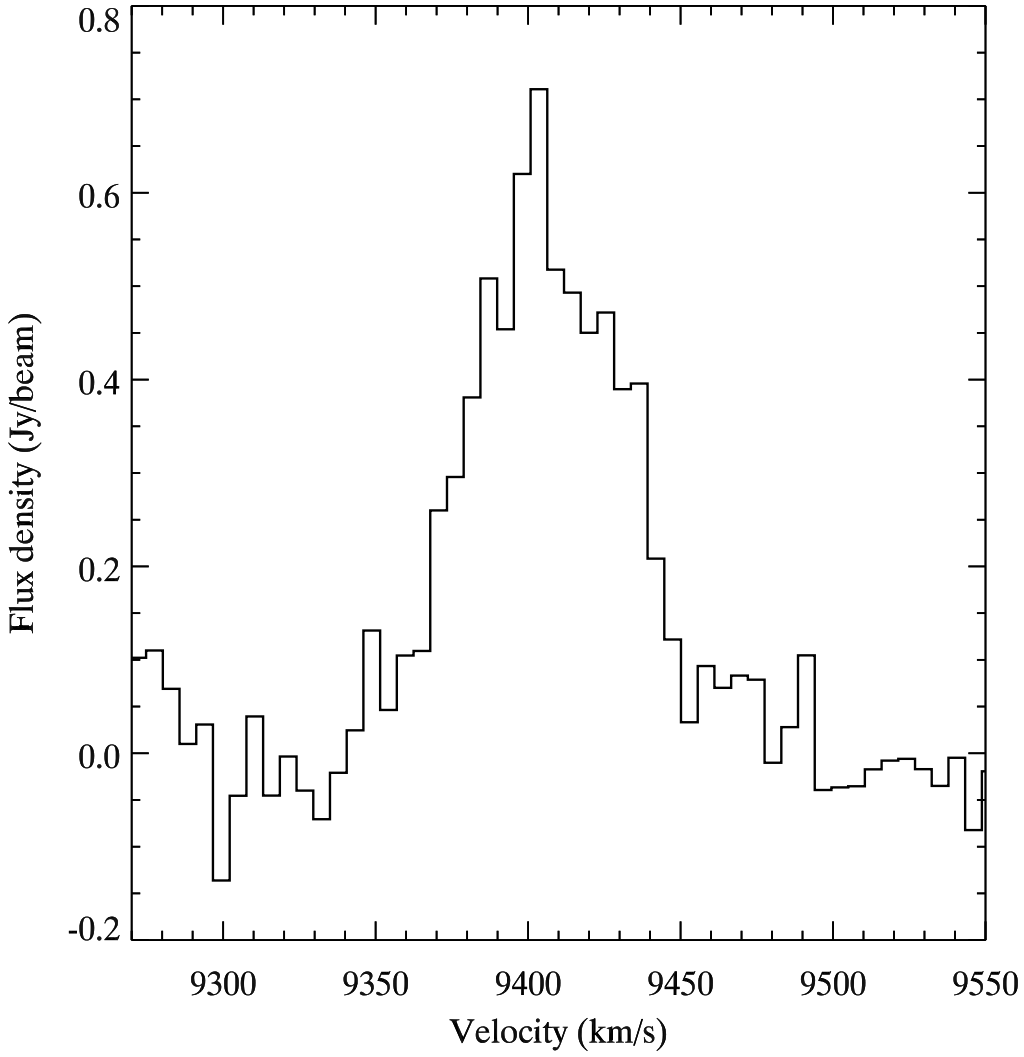

Figure 4.12: Extracted 21 cm HI spectrum of the entire Tadpole tidal tail region.

$$Z \sim 29 \times 10^{[12+\log(O/H)]-12} \tag{4.11}$$

where solar abundance is $12 + \log(O/H) = 8.72$ (Kolbulnicky & Kewley, 2004). For this massive young star cluster in the Tapole tidal tail, $Z = 0.006$, which for a $Z_{\odot} = 0.02$, indicates $Z/Z_{\odot} = 0.3$ for SSC 1. This is is similar to the metallicity of tidal tail regions observed in other systems (Duc et al., 2000).

To check this value, R_{23}, the ratio of the intensity of the oxygen emission lines to Hβ (Pagel et al., 1979), is calculated next. R_{23} is commonly used because it includes the brighter and more easily observed lines of oxygen and hydrogen. However, R_{23} is double valued with metallicity and so needs another line diagnostic (e.g., O_{23}) to help break the degeneracy. Various efforts over the years have been made to calibrate this method using empirical and/or photoionization models. Kolbulnicky & Kewley (2004) has a review of these methods. I use their Equations 8, 10, 13, and 16 to calculate the metallicity. Our initial metallicity calculation, $12 + log(O/H) = 8.3$, places SSC 1 on the lower branch of R_{23} where the ionization parameter, q, plays more of a role. Physically, the ionization parameter, or ionization state of the gas, can be thought of as the velocity of the ionization front in an HII region that is driven by the radiation field locally. The equation for the ionization parameter is

$$q = \frac{S_{H^0}}{n} \tag{4.12}$$

where the ionizing photon flux through a unit area is S_{H^0} and the local number density of hydrogen atoms is n (Kewley & Dopita, 2002). The ionization parameter, q, is calculated from Eq. 13 in Kolbulnicky & Kewley (2004) with the initial guess for the metallicity from the [NII] to Hα line ratio. The metallicity from the R_{23} method is then calculated using

$$x = \log R_{23} = \frac{I_{[OII]\lambda3727} + I_{[OIII]\lambda4959} + I_{[OIII]\lambda5007}}{I_{[H\beta]}} \tag{4.13}$$

$$y = \log O_{23} = \log(\frac{I_{[OIII]\lambda4959} + I_{[OIII]\lambda5007}}{I_{[OII]\lambda3727}}) \tag{4.14}$$

along with the equations from Kolbulnicky & Kewley (2004). Since this calculation assumes an initial metallicity to calculate q, the calculations were iterated until convergence. The metallicity for SSC 1 from the R_{23} method is $12 + \log(O/H) = 8.4$ or $Z/Z_{\odot} = 0.35$ which is remarkably similar to the value from [NII]/Hα. The ionization parameter for SSC 1, based on this method, is $q = 3.4 \times 10^7$ cm s^{-1}.

4.4 Discussion

I now compare the derived physical properties for SSC 1 and SSC 2. Specifically, I will examine star formation rates, gas available for star formation, and star formation efficiencies for these two sites of young massive star clusters in the tidal tail of the Tadpole. In addition, the global derived physical properties for the entire tidal tail of the Tadpole will be compared to tidal tails in other mergers.

4.4.1 SFR

The brightest tidal tail star cluster, SSC 1, has $L_{H\alpha}$ brighter than HII regions in Sc galaxies and indicates considerable star formation in a tidal tail region. The SFR of this region has also been studied in Jarrett et al. (2006) who examine three tracers: 24 micron flux, Hα from optical spectroscopy, and $[OIII]$ + Hβ from optical spectroscopy. Their SFR values range from 0.11 M$_{\odot}$yr^{-1}(24 micron) to 0.23 M$_{\odot}$ yr^{-1}(Hα from optical spectroscopy) to 0.39 M$_{\odot}$yr^{-1}($[OIII]$+Hβ). These are all less than our value of 0.53 M$_{\odot}$yr^{-1} at the same aperture size (12$''$). As mentioned above,

the measurements using optical spectroscopy (Hα and $[OIII]$+Hβ) may be a lower limit on the actual Hα flux for SSC 1 due to a slit width of 1.5″ under poor seeing conditions. Jarrett et al. (2006) also cautions that their SFR from 24 microns is a lower limit since they use a calibration from Calzetti et al. (2005) based on HII regions in the disk of M51 which has a different metallicity and star formation rate density than the tidal tail of the Tadpole. The SFR in this paper may be closer to the actual SFR of SSC 1, however, by using the formulation of Kennicutt (1998b), I am assuming a Salpeter IMF and solar metallicity which may not be correct assumptions for tidal tails. In addition, Hα may be affected by dust absorption. However, the Balmer decrement from optical emission lines tracing the photoionized gas from Tran et al. (2003) (Hα/H$\beta = 2.76$) indicates very little reddening (the expected Balmer decrement is 2.86). But the value from Jarrett et al. (2006) is Hα/H$\beta = 2.56$ which does indicate more reddening, but still not a lot of reddening.

To take into account any obscured star formation due to dust, I use the SFR indicator from Equation 7 in Calzetti et al. (2007) which uses both Hα and 24 microns:

$$SFR(M_{\odot}yr^{-1}) = 5.3 \times 10^{-42}[L(Ha)_{obs} + (0.031 \pm 0.006)L(24\mu m)]. \qquad (4.15)$$

This relation is empirically calibrated from observations of 220 star forming regions in the 33 nearby SINGS galaxies (which span a range of morphologies and a factor of 10 in oxygen abundance) along with integrated measurements of low metallicity starburst galaxies and luminous infrared galaxies (LIRGs). The data used for the calibration include MIPS 24 micron photometry, NICMOS Paα photometry, and ground based Hα photometry. Comparison of this relation with models suggest that it is applicable to large systems or galaxies with their energy output dominated by young stellar populations. Calzetti et al. (2007) also find that

using 24 microns alone is robust for high metallicity objects, but it deviates by factors of 2-4 for lower metallicity objects. This may explain the lower value for the SFR in SSC 1 using just 24 microns from Jarrett et al. (2006) since SSC 1 has a low metallicity. The SFR relation from Calzetti et al. (2007) assumes an IMF based on the Starburst99 (Leitherer et al., 1999; Vazquez & Leitherer, 2005) default (2 power laws with slope -1.3 from 0.1-0.5 $M_\odot$ and a slope of -2.3 from 0.5-100 $M_\odot$), continuous star formation for 100 Myr, and solar metallicity, but does take into account both unobscured and obscured star formation. Paα is less affected by dust than Hα and also traces the current SFR over a timescale of about 10-20 Myr, similar to Hα Kennicutt (1998b).

Using our value for the Hα luminosity and the 24 micron flux from Table 2 of Jarrett et al. (2006) for SSC 1 and Figure 6 of Jarrett et al. (2006) for SSC 2 (assuming a 20% error), I find a SFR of 0.39 ± 0.05 $M_\odot$ $yr^{-1}$for SSC 1 and 0.10 ± 0.01 $M_\odot$ $yr^{-1}$for SSC 2. These values are lower than our SFR using Kennicutt (1998b), but, for SSC 1, similar to the highest SFR from Jarrett et al. (2006) using $[OIII]$+Hβ.

Another SFR indicator that is widely in use is the bolometric infrared luminosity which is found to be directly proportional to the SFR in dusty starburst galaxies. However, this indicator is also subject to errors from evolved stars heating the dust in the IR, from calibrations done at sparsely sampled wavelengths or only for entire galaxies, not individual HII regions, and for assumptions of solar metallicity. The Tadpole is observed with PACS broadband photometry at wavelengths over 60-210 microns; however, SSC 1 has little dust (based on the Balmer decrement) and a low metallicity, the bolometric infrared luminosity is likely not a good SFR indicator in this tidal tail.

On a global scale, the global SFR of the entire tail (1.3 $M_\odot$ yr^{-1}) is between

$\sim 30 - 50\%$ of the global SFR of the entire Tadpole galaxy from FIR, 24 micron or 70 micron data (Jarrett et al., 2006). However, the high ratio of SFR in the tidal tail to the SFR of the entire merger may not able to be generalized to other minor mergers, since Jarrett et al. (2006) found that the nucleus of the Tadpole galaxy is not undergoing a starburst in spite of the high HI content. For example, the minor merger NGC 2782 is a luminous infrared galaxy (LIRG) undergoing a starburst (Devereux, 1989). Using Equation 4 in Kennicutt (1998b) and its far infrared (FIR) luminosity of $\sim 10^{44}$ erg s^{-1}, NGC 2782 has a total SFR of 4.5 M$_\odot$ yr^{-1} which is twice the SFR from FIR luminosity for the Tadpole.

4.4.2 Star Formation Rate Surface Density

To make a better comparison of the star formation rate between different regions in tidal tails, I compare the star formation rate per unit area, Σ_{SFR} from the observed Hα to the expected SFR per unit area from the gas density. Table 4.3 lists the tidal tail location, area of the extracted region, the star formation rate surface density based on the Hα emission $\Sigma_{SFR}(H\alpha)$, the gas surface density Σ_{gas}, and the expected star formation rate surface density from the gas surface density Σ_{SFR}(gas). These quantities are listed for aperture sizes and molecular measurements corresponding to both the CO(1-0) and CO(2-1) observations.

The Σ_{SFR}(Hα) with a 21″ aperture for the SSC 1 is 0.0044 ± 0.0006 M$_\odot$ yr^{-1} kpc^{-2} which is 3.7 times the value for SSC 2. SSC 1 is 4.4 times the value for W-HI-M in the Western tail of NGC 2782 and is 4 times the value for the tidal dwarf galaxy candidate in the Eastern tail of NGC 2782 (K13). For the smaller 11″ aperture, SSC 1 increases to $\Sigma_{SFR}(\mathrm{H}\alpha) = 0.011 \pm 0.002$ M$_\odot$ yr^{-1} kpc^{-2}.

The global star formation rate density for the entire tidal tail of the Tadpole is 0.00054 ± 0.00008 M$_\odot$ yr^{-1} kpc^{-2} which is lower than SSC 1 by a factor of more than 8. It is also a factor of 60 higher than the global star formation rate density for

Table 4.3: Comparison of Local & Global Star Formation Rates in the Tadpole Tidal Tail

Location	Area	$\Sigma_{SFR}(H\alpha)$	Σ_{gas}	Σ_{SFR}(gas)
	kpc^2	10^{-3} M$_\odot$ yr^{-1} kpc^{-2}	M$_\odot$ pc^{-2}	10^{-3} M$_\odot$ yr^{-1} kpc^{-2}
CO (1-0)				
1	146.6	4.4(0.6)	< 4.06	< 1.8
2	146.6	1.2(0.2)	< 3.71	< 1.6
Tail	2318	0.54(0.08)	< 5.37	< 2.6
CO (2-1)				
1	47.9	11(2)	< 7.2	< 4.0
2	47.9	2.9(0.4)	< 6.8	< 3.7

either tail in NGC 2782. This indicates the great amount of current star formation in the tidal tail.

4.4.3 Gas Available for Star Formation

As listed in Table 4.3, the gas density in the tidal tail regions is around 4 M$_\odot$ pc^{-2} in the 21″ aperture and around 7 M$_\odot$ pc^{-2} in the smaller 11″ aperture. These are both 11-30 times smaller than the gas density in the HI clumps in NGC 2782 (K13). This indicates that the Tadpole tidal tail had less gas available for star formation or that it has used up gas already in forming its stars.

The upper limit for the expected star formation rate per area based on the gas density is < 0.0018 M$_\odot$ yr^{-1} kpc^{-2} for SSC 1 using the 21″ aperture. For the smaller aperture, the Σ_{SFR}(gas) is < 0.0040 M$_\odot$ yr^{-1} kpc^{-2}. Since the gas densities for SSC 1 and SSC 2 are similar, their expected star formation rate per area is also similar.

By comparing the Σ_{SFR}(Hα) to the expected SFR from the gas density (Σ_{SFR}(gas)), the SFE can be estimated. For the 21″ aperture, SSC 1 has an observed Σ_{SFR}(Hα) more than twice as large as the SFR expected from the gas density. This indicates very efficient star formation for SSC 1. For SSC 2, the

expected SFR from the gas density is larger by a factor of more than 1.3 than the observed SFR per area, indicating less efficient star formation in this area.

On a global scale, the tidal tail of the Tadpole galaxy has an expected Σ_{SFR}(gas) that is almost 5 times larger than the observed $\Sigma_{SFR}(\mathrm{H}\alpha)$. This indicates that, on a global scale, the tidal tail of the Tadpole is 5 times less efficient at forming stars. However, the difference in $\Sigma_{SFR}(\mathrm{H}\alpha)$ to the expected Σ_{SFR}(gas) is much smaller than the factor of 30 between the expected Σ_{SFR}(gas) and the observed $\Sigma_{SFR}(\mathrm{H}\alpha)$ in the Eastern tail of NGC 2782 (K13), indicating that the Tadpole tidal tail is at least more efficient than the Eastern tail of NGC 2782.

4.4.4 Star Formation Efficiency

Combining the measures of gas availability and SFR, I examine the SFE for local and global regions in the Tadpole tidal tail. Previous observations have shown that star formation in tidal debris is less efficient than star formation in starburst or normal galaxies (Boquien et al., 2011), where multiwavelength data of major merger Arp 158 was used to study the local Kennicutt-Schmidt law. In addition, it was observed that the star forming regions in Arp 158 were seen to follow a different Kennicutt-Schmidt law than those in the central regions of that merger and were offset so that the same gas density resulted in a lower SFR. In NGC 2782, the HII region in the Western tail (W-HI-M) has an apparent SFE that is consistent with the star forming regions in the tidal debris of Arp 158 (Knierman et al., 2012), while the Eastern tail exhibits a SFE that is more than 2 dex lower (K13). For the Tadpole tidal tail, SSC 1 and SSC 2 lie above the relation of total gas surface density versus SFR surface density for the tidal debris of Arp 158 which indicates more efficient star formation in the Tadpole tail than in the tidal debris of that merger.

I calculate the gas depletion timescales (τ_{dep}) or the amount of time it would take for the current SFR to deplete the gas (molecular, atomic, and total). The SFE

is directly related to the inverse of the gas depletion time as it is a consumption rate. The gas depletion timescale for normal galaxies is $\tau_{dep,H_2} \sim 2$ Gyr (Kennicutt, 1998b) and for TDGs is $\tau_{dep} \sim 0.8 - 4$ Gyr (Braine et al., 2001). These ranges of gas depletion times correspond to normal SFE. A higher SFE will have $\tau_{dep} < 0.8$ Gyr and a lower SFE will have $\tau_{dep} > 2$ Gyr. Table 4.4 lists the tidal tail location, gas depletion time using molecular gas mass and Hα SFR ($\tau_{dep,H_2} = M_{mol}/SFR_{H\alpha}$), gas depletion time using 21 cm HI gas mass and Hα SFR ($\tau_{dep,HI} = M_{HI}/SFR_{H\alpha}$), and the gas depletion time using the total gas mass and Hα SFR ($\tau_{dep,tot} = M_{gas}/SFR_{H\alpha}$) for SSC 1 and SSC 2 for both apertures and the tidal tail as a whole.

SSC 1 has a gas depletion time of $\tau_{dep,H_2} < 110$ Myr from CO(2-1) and $\tau_{dep,H_2} < 160$ Myr as measured by CO(1-0), which are lower than the gas depletion times for W-HI-M in the Western tail of NGC 2782 ($\tau_{dep,H_2} < 1.5$ Gyr, K13). SSC 1 has a lower gas depletion time than the star forming regions observed in Arp 158 (Boquien et al., 2011) and in TDGs (Braine et al., 2001). However, SSC 1 is seen to be more similar to the gas depletion timescales in dwarf galaxies (1 -100 Myr) (Braine et al., 2001). The low gas depletion timescale for SSC 1 indicates that it has a SFE higher than other tidal debris or normal spiral galaxies. Instead, SSC 1 has a high SFE similar to dwarf galaxies when considering its molecular gas upper limit. SSC 1 also has a high SFE when considering its HI gas ($\tau_{dep,HI} = 400 - 560$ Myr), but a normal SFE considering its total gas mass ($\tau_{dep,tot} < 650 - 900$ Myr). SSC 2 is less efficient than SSC 1 at star formation, but with gas depletion times ranging from $< 0.6 - 3$ Gyr, it has a normal SFE similar to TDGs and normal spiral galaxies.

On global scales, the SFE calculated for the entire tail depends on the method used. Considering the upper limit to the molecular mass and Hα SFR, the tail has a low gas depletion timescale (high SFE) of $\tau_{dep,H_2} < 170$ Myr. This is similar to the SFE from SSC 1 and in dwarf galaxies. However, considering the high

Table 4.4: Star Formation Efficiencies in Tadpole Tidal Tail Regions

Location	$\tau^a_{dep,H_2,H\alpha}$ (Gyr)	$\tau^b_{dep,HI,H\alpha}$ (Gyr)	$\tau^c_{dep,tot,H\alpha}$ (Gyr)
CO(1-0) 21″			
SSC 1	< 0.16	0.56	< 0.92
SSC 2	< 0.63	1.9	< 3.2
Total	< 0.17	7.2	< 9.9
CO(2-1) 11″			
SSC 1	< 0.11	0.40	< 0.65
SSC 2	< 0.58	1.3	< 2.3

[a] $\tau_{dep,H_2,H\alpha}$ =M$_{mol}$/SFR(Hα)
[b] $\tau_{dep,HI,H\alpha}$ =M$_{HI}$/SFR(Hα)
[c] $\tau_{dep,tot,H\alpha}$ =M$_{tot}$/SFR(Hα)

gas depletion timescales from the HI gas mass ($\tau_{dep,HI} = 7.2$ Gyr) and the total gas mass ($\tau_{dep,tot} = 9.9$ Gyr), the tail has a low SFE and is less efficient at forming stars than normal spiral galaxies, but is still more efficient at star formation than the outer regions of spiral galaxies at r_{25} ($\tau_{dep,HI} \sim 20$ Gyr).

On local scales of ~ 10 kpc, it appears that the tidal tail of the Tadpole has highly efficient star formation around its super star clusters. Like the Western tail of NGC 2782, the material in this tidal tail may be experiencing gravitational compression which enhances the star formation. On global scales, however, the tidal tail indicates a high SFE via the molecular gas upper limit, but a low SFE based on the HI mass. This may indicate that the Tadpole tidal tail is deficient in molecular gas, as compared to its HI, on a global scale. This deficiency may be due to destruction of the molecular gas via UV radiation from new stars formed in SSC 1 and SSC 2, low metallicity causing the formation of less CO versus H_2, or the CO is present, but on smaller scales than observed here.

4.4.5 Variations in X_{CO}

In the calculations above, I use the value of X_{CO} based on observations of the Milky Way to calculate the upper limit for molecular mass based on our non-detections in CO(1-0) and CO(2-1). The standard CO to H_2 conversion factor ($X_{CO} = 2 \times 10^{20}$ cm^{-2} (K km s^{-1})$^{-1}$ or $\alpha_{CO1-0} = 4.3$ M$_\odot$(K km s^{-1} pc^2)$^{-1}$) is based on observations of molecular clouds in the Milky Way (Leroy et al., 2011). Using galaxies with $z \leq 1$, Genzel et al. (2011) find a linear relation given by $\log \alpha_{CO1-0} = 12.1 - 1.3\mu_0$ where $\mu_0 = 12 + \log(O/H)$. For a metallicity of $0.3Z_\odot$ (or $\mu_0 = 8.3$), the appropriate conversion factor is $\alpha_{CO1-0} = 20.4$ M$_\odot$(K km s^{-1} pc^2)$^{-1}$ giving a factor of 4.7 higher limit on the molecular mass ($M_{mol} < 5 \times 10^8$ M$_\odot$ for SSC 1 from CO(1-0)) than that derived from the standard conversion factor ($M_{mol} \leq 1.06 \times 10^8$ M$_\odot$). This higher upper limit on the molecular mass derived from the CO(1-0) measurement indicates that there may be as much molecular gas as $3 - 4 \times 10^8$ M$_\odot$, which is similar to what I see in the Eastern tail of NGC 2782 (K13) and the CO(1-0) observations of SSC 1 and SSC 2 are too shallow to detect. Despite the fact that the CO(2-1) measurements trace warmer molecular gas, the observed upper limit in this line when combined with the gives $M_{mol} < 2.8 \times 10^8$ M$_\odot$ which is still less than the molecular mass detected in the Eastern tail of NGC 2782 (K13).

Using the higher molecular gas mass upper limit from the X_{CO} for lower metallicity, I examine changes to the SFE as explored by the difference between $\Sigma_{SFR}(\mathrm{H}\,\alpha)$ and the expected $\Sigma_{SFR}(gas)$ as well as the SFE as estimated by the gas depletion timescale. For SSC 1, the higher molecular mass limit results in a larger expected $\Sigma_{SFR}(gas) < 0.0036$ M$_\odot$ yr^{-1} kpc^{-2} which is now only 0.8 times the $\Sigma_{SFR}(\mathrm{H}\,\alpha)$. Having a larger $\Sigma_{SFR}(\mathrm{H}\,\alpha)$ than from the expected $\Sigma_{SFR}(gas)$ indicates efficient star formation in SSC 1, but the difference between the two Σ_{SFR} using the new X_{CO} is less than the difference from using the Milky Way X_{CO}. For SSC 2, the

expected $\Sigma_{SFR}(gas) < 0.0034$ $M_\odot$ yr^{-1} kpc^{-2} is almost 3 times the $\Sigma_{SFR}(H\alpha)$, indicating less efficient star formation in SSC2. The difference between the two Σ_{SFR} is now greater in SSC 2. Regarding the gas depletion timescale calculations and SFE, SSC 1 still has a lower gas depletion timescale ($\tau_{dep,H_2} < 530 - 770$ Myr) considering the new molecular mass upper limit and a normal gas depletion timescale ($\tau_{dep,tot} < 1.1 - 1.5$ Gyr) considering the total gas mass upper limit. SSC 1 still has a high SFE considering molecular gas, but a normal SFE considering the total gas mass. These gas depletion timescales are closer to the values in the tidal debris of Arp 158 (Boquien et al., 2011) and TDGs (Braine et al., 2001). For SSC 2, the increased upper limit for molecular mass gives $\tau_{dep,H_2} < 2.7 - 3$ Gyr, and with total gas mass in the system gives $\tau_{dep,tot} < 4 - 5$ Gyr. Both values are similar to the observed gas depletion timescales in normal star forming galaxies, indicating normal SFE in SSC 2. The difference in SFE observed before between SSC 1 and SSC 2 still remains with SSC 1 having higher efficiency star formation and SSC 2 having normal SFE. Even with a higher molecular gas mass upper limit using a new X_{CO} for the metallicity of the Tadpole tail, our major results do not change.

4.5 Conclusions

By applying the techniques developed in the comparison of the tidal tails of NGC 2782 (K13), I examine the conditions for star formation in the tidal tail of the Tadpole galaxy. This tidal tail has two large sites of star formation, SSC 1 and SSC 2, which have been previously studied (Tran et al., 2003; de Grijs et al., 2003; Jarrett et al., 2006). In this paper, I present the first Hα narrowband images, CO observations, and VLA HI observations to examine the star formation and star formation efficiency in this tidal tail. From the Hα observations, I find 5 HII regions in the tidal tails which are grouped into two regions associated with SSC 1 and SSC 2. The HII regions in this tidal tail are more luminous than comparable

tidal tail regions in other galaxies. The global $L_{H\alpha}$ of the Tadpole tidal tail is higher than that seen in tidal debris regions in other mergers. The global SFR of the Tadpole tidal tail is comparable to the SFR of the entire Milky Way galaxy. Only upper limits for molecular gas mass were found with IRAM observations for CO(1-0) and CO(2-1). The new H I observations improve on the resolution achieved for the Tadpole by a factor of 3 (from $36''$ to $12''$). I find a higher star formation rate surface density in the Tadpole when compared to that measured in tidal tails of NGC 2782, which indicates that the Tadpole has a higher level of current star formation. However, the gas density in the Tadpole tidal tail is less than observed in the tails of NGC 2782 which possibly indicates that the gas in the Tadpole tidal tail has been depleted by its current star formation rate. For SSC 1, I measure a higher observed SFR surface density from Hα when compared with the expected SFR surface density measured from the gas density which indicates a higher efficiency of star formation. This correlates well with the gas depletion timescales in SSC 1 which have been seen to range from $< 100 - 900$ Myr depending on the particular phase of gas mass used for the calculation. Similarly, SSC 2 has gas depletion times that range from $< 0.7 - 10$ Gyr which indicates less efficient star formation mode than seen in SSC 1. With gas depletion times of < 100 Myr based on the molecular gas upper limit, SSC 1 is as efficient in forming stars as a dwarf galaxy. If I use a different CO to H_2 conversion factor appropriate for the lower metallicity of SSC 1, the derived molecular mass upper limit increases giving a less extreme SFE of $< 0.4 - 1.5$ Gyr, which still indicates efficient star formation which is as efficient as that seen in TDGs. Such high star forming efficiency may be caused by gravitational compression in the tidal tail which can increase the rate of star formation.

Chapter 5

CONCLUSIONS

This dissertation examines star formation in the tidal tails of minor galaxy mergers. Minor mergers are less severe versions of major mergers, but are more common in the universe and likely played a role in forming most large galaxies, including our Milky Way Galaxy. Vigorous star formation occurs in the centers of many mergers due to the high gas density and turbulence from the merger. Due to its brightness and visibility over cosmological distances, star formation in centers of mergers has been well studied. However, the tidal debris of mergers has not been as well studied. These areas are lower density, but have large reservoirs of gas as fuel for star formation and may have the higher turbulence of the merger. Studying tidal debris of mergers gives insight into star formation near the threshold. Unlike the outer regions of spiral galaxies, which are also studied for star formation thresholds, tidal debris gives a regime with higher turbulence, but low densities. Due to the higher frequency of minor mergers, the tidal debris of minor mergers was chosen for study. Various tracers for star formation were studied to determine the different factors that may influence star formation in tidal debris. These tracers include young star cluster populations, star cluster complexes, Hα emission, and [CII] emission. Star formation tracers can be compared to the reservoirs of gas available for star formation to estimate the star formation efficiency. To examine star formation in detail on local and global scales, multiwavelength data were needed which necessitated the careful selection of which galaxies to use for this study. The results from this study can be used to constrain models of star formation, particularly at low densities.

5.1 Star Formation in Tidal Debris of Minor Mergers

The multiwavelength data sets of the minor mergers NGC 2782 and UGC 10214 ("The Tadpole") allow examination of star formation on scales of ~ 10 kpc and smaller in both galaxies. In all three tidal tails, I find evidence for star formation occurring in situ within the tails indicating that minor mergers, like major mergers, host star formation in their tidal debris.

5.1.1 Star Clusters and Star Cluster Complexes

Young star clusters are found in all tidal tails in this study. In NGC 2782, I discover populations of young star clusters in both tidal tails. However, the distribution of star clusters and their properties are different between the two tails of NGC 2782. In the Eastern tail, the star clusters are found in clumps of multiple star clusters known as star cluster complexes. However, the Western tail hosts only lower luminosity isolated star clusters. In the Tadpole, over 40 young star clusters have been previously found along the tidal tail (Tran et al., 2003; de Grijs et al., 2003), but mostly clustered in two bright clumps in the center of the tail. The brightest of these clumps, SSC 1, has a very luminous point source which is found to be very massive and qualifies as a super star cluster.

Mullan et al. (2011) explore star cluster populations in both major and minor merger tidal tail regions using HST images. This work built on the prior study by Knierman et al. (2003) of star clusters in the tidal debris of major mergers. Comparisons of the star clusters in this thesis to their work in 23 tidal tails finds less star clusters in the Eastern tidal tail of NGC 2782 than Mullan et al. (2011) however they have a more generous definition of the tidal tail area. They find evidence for young star cluster populations in 10 out of the 23 tidal tails studied. Contrary to the (admittedly fewer in number) sample of tidal tails in major

mergers, they find tidal tails that have both TDGs and star clusters along the tail. Comparing various properties of the merging systems and tidal tails, they find that tails with the largest number of star clusters are likely to be young (< 250 Myr) and have a brighter V band surface brightness. This may be due to the strong bursts of star formation that occur soon after the periapse of the merger.

5.1.2 HII regions

Regions of Hα emission were found in all the tidal tails of this study, and generally trace the more luminous star clusters in the tails. In the Eastern tail of NGC 2782, there are several HII regions in the area between the main spiral and the remnant dwarf galaxy. These are spread over an area a little more than 10 kpc across in discrete points. In the Western tail of NGC 2782, I find one isolated HII region midway along the tidal tail. In the Tadpole galaxy, I find a total of 5 bright HII regions. These are grouped into two main areas corresponding to the two star clusters SSC 1 and SSC 2. SSC 1 has an irregular shape likely to be the result of multiple point sources blending together. The SFR of these individual HII regions ranges from the higher range of $0.02 - 0.4$ $M_\odot$ yr^{-1} in the Tadpole to 0.015 in the Western tail of NGC 2782 to the lower range of 0.002-0.008 in the Eastern tail of NGC 2782.

However, the SFRs presented here are lower limits since they are based on narrowband Hα imaging. Hα represents star formation in the last $\sim 10 - 20$ Myr. Also the SFRs in the tails could be higher than inferred from Hα if it is predominately of a Taurus-Auriga type (Kenyon et al., 2008), producing few star clusters with high mass stars. If so, the color would be blue, but no Hα would be observed. In the case of the Western tail of NGC 2782 (Knierman et al., 2012), faint UV emission is detected along the Western tidal tail, indicating the presence of young stellar populations, likely dominated by B and A stars. Since there is no Hα

emission in the Western tail of NGC 2782 (except for the single knot) the star clusters forming along the tail were likely of low mass and had a negligible probability of forming early B and O stars.

5.1.3 Possible Tidal Dwarf Galaxies

There are two tidal dwarf galaxy candidates (TDGCs) in this work, the TDGC in the Eastern tail of NGC 2782 and SSC 1 in the Tadpole. TDGs have similar luminosities as dwarf galaxies ($-18 < M_B < -14$, $10^8 < L_B < 10^{10}$ $L_\odot$), but higher average metallicities ($Z \sim 0.3 Z_\odot$), blue colors, and high SFR ($10^{39} < L_{H\alpha} < 2 \times 10^{40}$ erg s^{-1} Braine et al., 2001). TDGs have HI masses ranging $0.5 - 6 \times 10^8$ $M_\odot$. Some TDGs have been measured to be gravitationally independent (Duc et al., 2000).

TDGC in the Eastern tail of NGC 2782 was found serendipidously by Yoshida et al. (1994) using optical spectroscopy and R band imaging of NGC 2782. Using the velocity of the Hα line, TDGC is estimated to have a dynamical mass of $\sim 4 \times 10^8$ $M_\odot$. It has a blue color ($V - I = 0.3$, but is fainter than most TDGs ($M_{V606} = -13$) and is small with a diameter of ~ 1.3 kpc. It has star formation on the low end of TDGs with $L_{H\alpha} = 10^{39}$ erg s^{-1}. Also, it has a lower HI mass (2.6×10^8 $M_\odot$) than other TDGs. Yoshida et al. (1994) find an enhanced [OIII] λ5007 to Hβ ratio which indicates low metallicity, but they only detect 3 lines in their spectrum which lessens the ability to determine metallicity. Even though Yoshida et al. (1994) called it a TDG, it seems to be at least a very low mass TDG. It does not seem to be dynamically different than other parts of the Eastern tail in the HI data (Smith, 1994; Smith et al., 1999). More careful consideration of HI data at this location in the Eastern tail of NGC 2782 may shed more light on this question.

While the super star cluster SSC 1 itself may not be a TDG candidate, the entity studied over a 21″ aperture at the location of SSC 1 is worth consideration. The scale measured by 21″ at the distance of the Tadpole is 13. 7 kpc which could encompass a dwarf galaxy. SSC 1 has an HI mass of $\sim 4 \times 10^8$ $M_\odot$which is on the lower end of the TDG HI masses. However, this HI mass only encompasses 21″ and inspection of Figure 4.9 shows that the clump of HI at the location of SSC 1 is larger in size than 21″, so the HI mass would increase. The g' luminosity is 3.8×10^8 $L_\odot$which is also on the lower end of the luminosity for TDGs. The metallicity determination of SSC 1 shows a metallicity similar to other TDGs but it has a higher SFR. Tran et al. (2003) find that SSC 1 is not likely to be a bound object, but this is on the smaller scale of the HST observations. Jarrett et al. (2006) find a higher mass for SSC 1, but inconclusive results on whether SSC 1 is gravitationally bound. These data will help to find a more correct mass, and the velocity dispersion of the HI line will also help with determining whether SSC 1 is gravitationally bound. In summary, SSC 1 is of similar brightness, color, and metallicity to other TDGs. It may be smaller than most TDGs, but it has very high SFR.

5.1.4 [CII] emission

This work presents the first detection of [CII] in the Eastern tidal tail of NGC 2782. The [CII] is coincident with the brightest HII regions. The Western tail of NGC 2782 has a non-detection of [CII] even though its HII region is brighter than any in the Eastern tail. This indicates that [CII] emission is suppressed relative to Hα in the Western tail. This lack of [CII] in the Western tail together with the non-detections of CO and the higher than solar abundance of oxygen (Torres-Flores et al., 2012) indicates that perhaps the Western tail has a high oxygen to carbon ratio and is undergoing its first generation of star formation.

The SFR using the [CII] emission for the Eastern tail regions ranges from

0.02-0.03 $M_{\odot}yr^{-1}$which is higher than that found from the Hα emission. However, the SFR equation for [CII] that I use here is based on star forming galaxies, not individual HII regions in tidal debris. There may be metallicity effects or differences at lower pressures or gas densities that could affect the SFR based on [CII]. These results may help calibrate star formation rates based on [CII] observations in regions which are different than star forming galaxies where many of the calibrations are based. Future results from Herschel observations of [CII] in HII regions in galaxies of various metallicities and types are eagerly anticipated.

5.2 Gas Reservoirs for Star Formation on Local Scales in Tidal Debris

I examine several tracers for the reservoirs of gas for star formation in the tidal tails and find that these tracers are not consistent. All three tails have abundant neutral hydrogen gas as traced by the 21 cm line of hydrogen. However, only the Eastern tail of NGC 2782 has detected molecular gas and ionized gas (though there are no observations of [CII] in the Tadpole). One might expect the Western and Eastern tails of NGC 2782 to have similar molecular gas masses due to their similar SFR surface density from Hα. The Tadpole tidal tail has larger SFR surface densities than in the tails of NGC 2782, so one might expect it to have detected molecular gas. The detection limit for CO (1-0) is less than the detected molecular gas in the Eastern tail of NGC 2782 which indicates that there is a lack of molecular gas in the Tadpole (or, at least, a lack of CO). This lack of CO may be due to its low metallicity ($Z = 0.3Z_{\odot}$).

Examining the gas surface density, I find that the Eastern tail of NGC 2782 has a higher Σ_{gas} than the Western tail. That it does not also have a higher SFR per area indicates that something different is going on between the Eastern and Western tails of NGC 2782. Due to the non-detections in CO and [CII] compared to its HI and Hα, the Western tail of NGC 2782 may be unable to produce detectable

CO or [CII] emission. This may be due to a difference in the ratio of carbon to oxygen, since it has a high oxygen abundance from previous spectra. This could be because the Western tail material is going through its first generation of stars and has not had time to build up a higher carbon abundance.

The Tadpole tidal tail has a gas surface density that is 11-30 times smaller than in the tails of NGC 2782, but it has a higher SFR density than NGC 2782. The expected star formation rate from the gas density is much higher than the observed SFR from Hα in the NGC 2782 system, but the two values are more similar in the Tadpole. This could indicate that star formation is less efficient in the tidal tails of NGC 2782, but more efficient in the Tadpole. Also, I measure star formation via Hα which traces only very recent (< 10 Myr) star formation and with massive enough stars nearby. This means that our SFR values are only a lower limit and, for NGC 2782, there may be star formation on smaller scales which did not produce enough massive O and B stars that would cause Hα emission. The examination of the GALEX images supports this since there is FUV and NUV emission along the tidal tails which can come from lower mass B and A stars.

The HI column density in tidal tails of mergers was studied on local scales by Mullan et al. (2013). They found that tidal tails in minor mergers have more relatively high column density than tidal tails in major mergers. They also study the velocity gradients of the HI gas and find that major mergers generally drive gas to higher velocity gradients on 10 kpc scales. However, their sample has twice as many major mergers than minor ones, so small numbers may be at fault. Examination of the Tadpole galaxy using similar methods as Mullan et al. (2013) would be informative since it is a minor merger with ample star formation in its tail.

5.2.1 The Possibility of Dark Gas in Tidal Debris

Based on the non-detections of CO(1-0) in the Western tail of NGC 2782, one might expect the molecular gas to be in another form. The stability diagram for CO also gives a clue as to how molecular gas can go undetected. CO does not form until and A_V of 3 or more, while H_2 forms at A_V of less than 1 (Hollenbach & Tielens, 1997). In a low pressure environment like a tidal tail a substantial amount of molecular gas can exist with conditions that do not favor the formation of CO, so the CO to H_2 conversion factor is not a constant. In the low gas density environment of tidal debris a substantial reservoir of molecular gas can exist at low A_V that will not be detectable through CO. However, in this regime, [CII] will be present in higher amounts. Theoretical models for molecular clouds in Wolfire, Hollenbach, & McKee (2010) show that the fraction of molecular mass in the "dark gas" (H_2 and [CII]) is $f \sim 0.3$ for typical galactic molecular clouds. For lower A_V and lower metallicities (as in these tidal tail regions), the fraction of dark mass in H_2 increases. Given this reason, I observed the Western tail with the Herschel Space Observatory to see if [CII] was present where CO was not.

I do not find [CII] in the Western tail at the location of the HII region at a significant level. This HII region has a higher Hα luminosity than any individual HII region in the Eastern tail, but [CII] emission is only detected in the Eastern tail. Given that Hα and [CII] emission ultimately originate from the same sources of hard UV photons with energy greater than 13.8 eV, they are expected to trace each other. This indicates that the molecular gas in the Western tail of NGC 2782 does not have significant amounts of CO or [CII]. However, this region may have significant amounts of molecular gas in the form of H_2. Unfortunately, H_2 is difficult to directly detect. The molecule has no dipole moment to produce detectable radio emission, and can only be detected through electron transitions. In general H_2 is

not directly detectable, so I generally rely on surrogate tracers such as CO. The $CO(1-0)$ spectral line at 2.6 mm probes the cold ($\sim$ 5K, $N_{H_2} \approx 10^{21} cm^{-2}$) molecular gas component. Although such observations allow inferences of a molecular gas mass, they are rather insensitive to the highly energetic molecular environment where stars have recently formed. In order to probe this hot ($\sim$ 2000 K) component and gain a better understanding of the feedback mechanisms between the young stars and gas within these regions, 2.12μm H_2 emission at the edges of molecular clouds can be observed with narrow band filters.

The 2.12μm H_2 line can be excited by either UV radiation from nearby young massive stars or via shocks from dramatic events such as supernova or merging gas clouds in a galaxy merger. Studies of star forming regions of normal and starbursting galaxies show that H_2 emission from fluorescence traces the amount of star formation activity (Pak et al., 2004). Davies et al. (1998) also detect H_2 in Blue Compact Dwarf Galaxies using a Fabry-Perot etalon. They see emission from the bright centers as well as some diffuse emission in a tidal tail shape from a possible galaxy merger. Spitzer Space Telescope observations of Stephan's Quintet, a compact group of galaxies, show very high levels of H_2 emission aligned with tidal debris where star formation occurs at a high rate (Appleton et al., 2006). These H_2 lines occur in the $5-38\mu$m range and result from shocks in the intergalactic medium, not UV radiation from stars. Though these are longer wavelength lines, one would expect to also see the 2.12μm H_2 line from this region. I can observe this and other compact groups for evidence of this emission excited due to shocked gas which may be the more common excitation mechanism in these systems. Shocks also occur in the tidal debris of major merger NGC 4676 ("The Mice"). Barnes (2004) suggested that the observed properties of the merger matches the models including shock-induced star formation in the merger as opposed to density-dependent star formation. Subsequent observations of star clusters in NGC

4676 show the ages of the star clusters to be consistent with the shock-induced star formation model (Chien et al., 2007). Deep observations of these shocked regions of NGC 4676 may show the 2.12μm H_2 line. Observing the 2.12μm H_2 may give insight into how much dark gas is in these tidal debris regions.

5.3 SFE on Local Scales in Tidal Debris

One proxy for SFE is the gas depletion time (τ_{dep}) or the amount to time it would take for the current SFR to deplete the gas (molecular, atomic, or total). The SFE is then the inverse of the gas depletion time. Other work finds gas depletion times measured using molecular mass and SFR based on FUV and 24 micron observations to range from 0.5-2 Gyr in the star forming regions of the major merger Arp 158 (Boquien et al., 2011). TDGs were found by Braine et al. (2001) to have $\tau_{dep} \sim 0.8 - 4$ Gyr using molecular gas and Hα emission. TDGs have similar gas depletion times to average spiral galaxies. For our tidal tails, I find short gas depletion times ($< 100 - 900$ Myr) in the Tadpole tidal tail region SSC 1 indicating efficient star formation. SSC 2 in the Tadpole has gas depletion times ranging from $< 0.6 - 3$ Gyr, it has a similar SFE to TDGs and normal spiral galaxies. W235 in the Western tail of NGC 2782 has a higher star formation efficiency considering its molecular gas limit (< 1.5 Gyr), but a low star formation efficiency considering its HI mass (7.7 Gyr). The HII regions in the Eastern tail of NGC 2782 all have very low SFE (12-200 Gyr) except the tidal dwarf galaxy candidate (TDGC) when considering its HI mass and its SFR from [CII] and Hα (1.3 Gyr and 5 Gyr, respectively). A tidally formed region such as the Western tail of NGC 2782 or the Tadpole, would have gravitational compression and possibly enhanced star formation. Given the higher SFE in SSC 1 or W235, this may be evidence for gravitational compression in the tidal tail. I examine this further in the next section.

5.4 Comparison with Star Formation Laws

To directly compare our HII regions in tidal tails of minor mergers to star forming regions in other mergers and in other galaxies, I plot our data onto plots from other studies of star formation. First, I compare our tidal tail regions to star forming regions in Arp 158 which is an intermediate stage merger. Boquien et al. (2011) use multiwavelength data of major merger Arp 158 to study the local Kennicutt-Schmidt law. They first use the mass of molecular hydrogen, H_2, and the star formation rate from FUV and 24 microns for individual regions in Arp 158 (including the nuclei of the merging spirals and regions in the tidal debris) as compared to the Kennicutt-Schmidt Law for spiral galaxies (from Bigiel et al., 2008, see dashed line in Figure 5.1). For Arp 158, they find that the tidal debris regions C3 and C5 follow the same Kennicutt-Schmidt Law for molecular hydrogen gas as in spiral galaxies. The tidal debris region C2 lies above the line, having more star formation per area than expected based on its H_2. Comparing our regions to theirs (see Figure 5.1), I find that Σ_{H_2} for W235 in the Western tail of NGC 2782 and SSC 1 and SSC 2 the Tadpole have comparable values to C5 and C2 in the tidal tails of Arp 158. For these sources, our Σ_{H_2} is an upper limit since I have non-detections in CO(1-0) and CO(2-1). I also indicate the upper bound of our determinations of Σ_{H_2} based on a larger $X_{CO} = 9.4 \times 10^{20}$ cm^{-2} (K km s^{-1})$^{-1}$ corresponding to a metallicity of $0.3Z_{\odot}$. SSC 1 in the Tadpole lies above the relation for spiral galaxies and the sources in Arp 158 indicating that it is more efficient at forming stars. This holds for both the CO(1-0) and CO(2-1) observations and different beam sizes. This also holds even for the different CO to H_2 conversion factor, though it does lie closer to the line, but still above it. For both CO observations and aperture sizes, SSC 2 in the Tadpole lies above the relation considering a Milky Way X_{CO}, indicating that it has more efficient star formation than in a spiral galaxy, but less efficient than SSC

1. However, for a higher X_{CO} for a lower metallicity, SSC 2 lies just below the line, indicating slightly less SFE than in a spiral galaxy. W235 in the Western tail of NGC 2782 is consistent with the values for C5 in Arp 158 indicating a similar SFE as in spiral galaxies. For a lower metallicity X_{CO}, W235 lies below the line indicating a less efficient star forming region. The HII regions in the Eastern tail of NGC 2782 have a similar Σ_{H_2} to the nuclear regions of Arp 158 and the tidal tail region C3, but they lie well below the Kennicutt-Schmidt relation for molecular hydrogen indicating a very low SFE. The clear separation of the Eastern tail of NGC 2782 from the other tidal tail regions indicates that something very different is happening there.

Next, I compare the total mass surface density from HI, H_2, and He to the SFR surface density. Boquien et al. (2011) find that star forming regions in the tidal debris of Arp 158 follow a different Kennicutt-Schmidt law than those in the central regions of the merger, falling along a line of similar slope to Daddi et al. (2010), but offset so that the same gas density gives lower values of SFR. Using our total mass surface densities from HI and CO upper limits (or detections in the case of the Eastern tail of NGC 2782) and SFR from Hα emission, I plot our HII regions as compared to the regions in Arp 158 (see Figure 5.2). For this comparison, I have a lower bound to the total gas density based on the assumption that the total gas mass is equal to just the mass of HI. In Figure 5.2, the upper limits are denoted by arrows where the terminus of the arrow demarcates the lower bound of the gas density from the HI observation. The upper end of the arrow (or line segment) then indicates the total gas density if the molecular gas mass is determined using a larger X_{CO} corresponding to a metallicity of $0.3Z_{\odot}$. SSC 1 in the Tadpole again lies above the Kennicutt-Schmidt laws for Arp 158 (both quiescent and starburst), now determined for total gas surface density. SSC 1 also lies above the Daddi et al. (2010) relation for quiescent galaxies, but below the Daddi et al. (2010) relation for

starburst galaxies. This indicates a higher SFE for SSC 1 than in normal spiral galaxies and perhaps at least in one starburst galaxy, Arp 158. If I consider the total gas density using the larger X_{CO}, SSC 1 lies close to the line for starbursts from Boquien et al. (2011). W235, as mentioned previously, is consistent with the star formation in the tidal tail region C5 in Arp 158, which lies below the line from Daddi et al. (2010). This indicates a less efficient star formation than in normal spiral galaxies. The HII regions in the Eastern tail of NGC 2782 again lie well below the other tidal tail regions indicating a very low SFE. Again, the total gas surface density for these regions is similar to the nuclear regions of Arp 158, but with very suppressed star formation. Even considering the total gas density, something different is going on with the Eastern tail of NGC 2782.

Finally, I compare the Kennicutt-Schmidt Law for HII regions in many different types of galaxies as well as integrated observations of galaxies to our regions in minor merger tidal debris. Figure 6 from Renaud et al. (2012) is presented in Figure 5.3. This figure shows the total gas surface density for local and global regions in normal, spiral, and dwarf galaxies at low and high redshift versus their SFR density. These observations are compared to analytical models using physically motivated parameters. Of particular attention to our sample is the small cyan stars representing the Arp 158 observations from Boquien et al. (2011) and a new sample of tidal debris and outer regions in nearby major mergers (Duc et al., 2012). Our magenta stars from the Tadpole and the Western tail of NGC 2782 overlap with the upper part of the cyan stars. This indicates a similar star formation law as those regions in major mergers. This region at around 10 $M_{\odot}pc^{-2}$ and 0.003 $M_{\odot}yr^{-1}kpc^{-2}$, is also occupied by normal spiral galaxies from Kennicutt (1998b) and Bigiel et al. (2008) as well as the lower bound of HII regions in M51 from Kennicutt et al. (2007). The HII regions in the Eastern tail of NGC 2782 have a star formation rate law which is similar to the SMC (Bolatto et al., 2011). This

may indicate that both the SMC and the Eastern tail of NGC 2782 have repressed star formation given their relatively high gas density. The SMC observations included inferred H_2 from HI maps and infrared observations to get a dust to gas ratio and SFR from Hα.

The analytical models of Renaud et al. (2012) describe the relation between the surface density of gas and the surface density of SFR as observed over regions within galaxies and galaxies as a whole and over several galaxy types. The parameters of the model are the gas density probability density function (PDF) and a local star formation law. The PDF represents the turbulence in the ISM. The local star formation law has a threshold from the beginning of supersonic turbulence and regulation by stellar feedback. They find that this threshold translates to a break in SFR at low surface densities for all scales (regions in galaxies and galaxies as a whole). They also find that turbulent regulation explains the 1-2 Gyr gas depletion timescales in nearby spirals. For more dense and more turbulent systems as in high redshift galaxies and Milky Way molecular clouds, a more shallow relation between gas surface density and SFR surface density is seen. Another area that needs more study is the low surface density gas with star formation. Renaud et al. (2012) find that regions in Boquien et al. (2011) and in Duc et al. (2012) have much higher SFR surface densities for their very low total gas surface densities. Additional observations of molecular gas and HI in tidal debris can probe these areas.

As compared to the models of Renaud et al. (2012), the region of W235 lies near the model line tracing spirals which has a Mach number of 1, a thickness of 100 pc, and a volume density threshold for star formation of 100 cm^{-3}. SSC 1 lies closer to the model line tracing low-z mergers which has a Mach number of 2, a thickness of 200 pc, and a volume density threshold for star formation of 10 cm^{-3}. The HII regions in the Eastern tail of NGC 2782 are less than the model for the SMC which has a Mach number of 2, a thickness of 500 pc, and a volume density threshold for

star formation of 100 cm^{-3}. Since the SMC has a low metallicity (~ 0.2 Z$_\odot$), there are less metal lines available to cool the ISM, leading to less efficient ISM cooling, so the transition to supersonic turbulence happens at a higher density. In the case of the SMC, cold gas is less abundant possibly due to metallicity effects or increased heating from UV radiation from star formation. In the Eastern tail of NGC 2782, I suspect that feedback from stars forming in higher mass star cluster complexes or possibly its formation as a "splash" region (versus a tidal region of merger debris) may have inhibited star formation. In a splash region, shocks may occur providing gas heating during the encounter which can inhibit star formation. Feedback from new stars can also heat the gas and suppress new star formation. Further observations of the metallicity of the HII regions in the Eastern tail of NGC 2782 as well as the Kennicutt-Schmidt law in other tidal debris regions can help to sort out the parameters that affect star formation in these environments.

5.5 Future Work

Several avenues for exploring how star formation proceeds in the tidal debris of minor mergers are yet to be explored completely. In particular, only two systems out of fifteen minor mergers were explored in this work. Further study can be done on additional minor mergers individually and on the sample as a whole. Additional work can be done on star formation in tidal debris, gas properties on local scales, and TDG formation.

5.5.1 Star Formation

Future work looking for young star clusters, star cluster complexes, and HII regions in tidal debris of minor mergers includes examination of existing ground based images in $UBVR$ for 13 additional minor mergers and of ground based Hα images for 7 of those minor mergers. This sample of minor mergers spans a range of

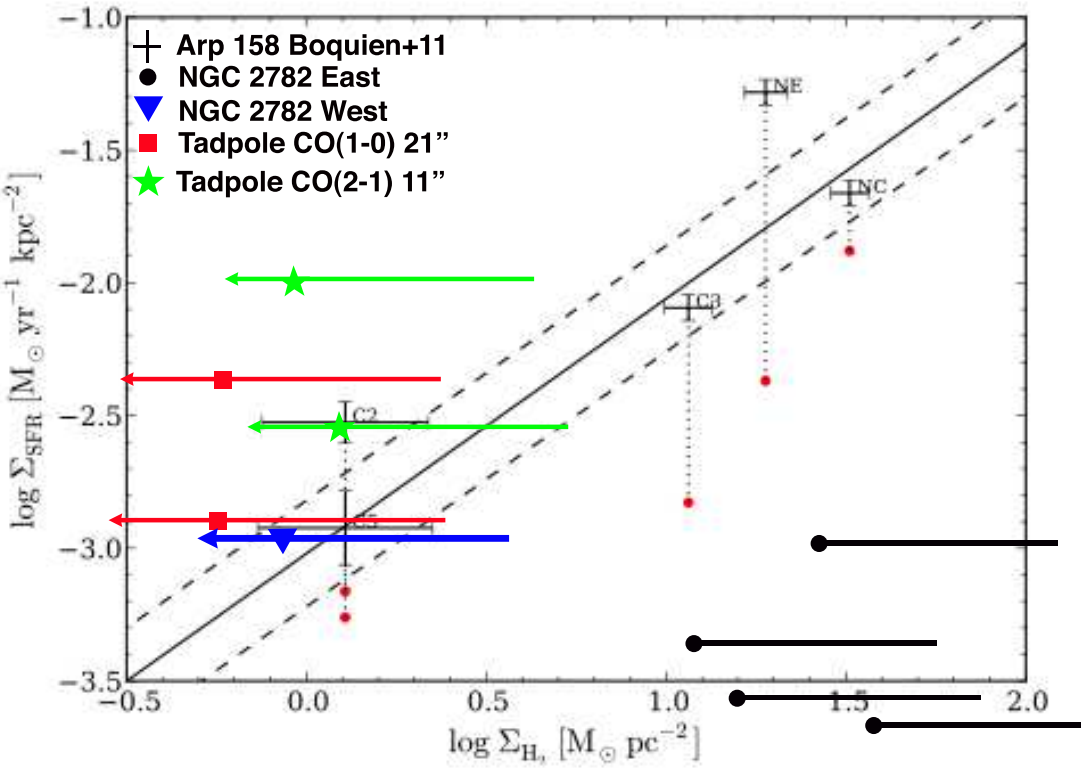

Figure 5.1: Figure 5 from Boquien et al. (2011) which plots the SFR density versus the H_2 (no He is included) gas surface density for regions in the merger Arp 158. The regions from this thesis are over plotted as described in the legend. The arrows indicate upper limits for non-detections of CO(1-0). The upper end of the arrows indicates the molecular hydrogen surface density with a larger X_{CO} corresponding to a metallicity of $0.3Z_{\odot}$. The solid line indicates the Kennicutt-Schmidt Law for H_2 in spiral galaxies (Bigiel et al., 2008).

interaction stages, mass ratios, and distances. Using these ground based images of minor mergers can help to pinpoint areas for examining in detail with future HST observing programs of minor mergers. The high resolution images of HST are the best way to determine whether a point source observed from the ground to be a star cluster candidate is a star cluster or a star cluster complex. Ground based imaging alone cannot accomplish this at the distances of these minor mergers. The use of more sophisticated stellar population models which have emission lines included can also be compared to the SEDs using photometry of star cluster candidates in these

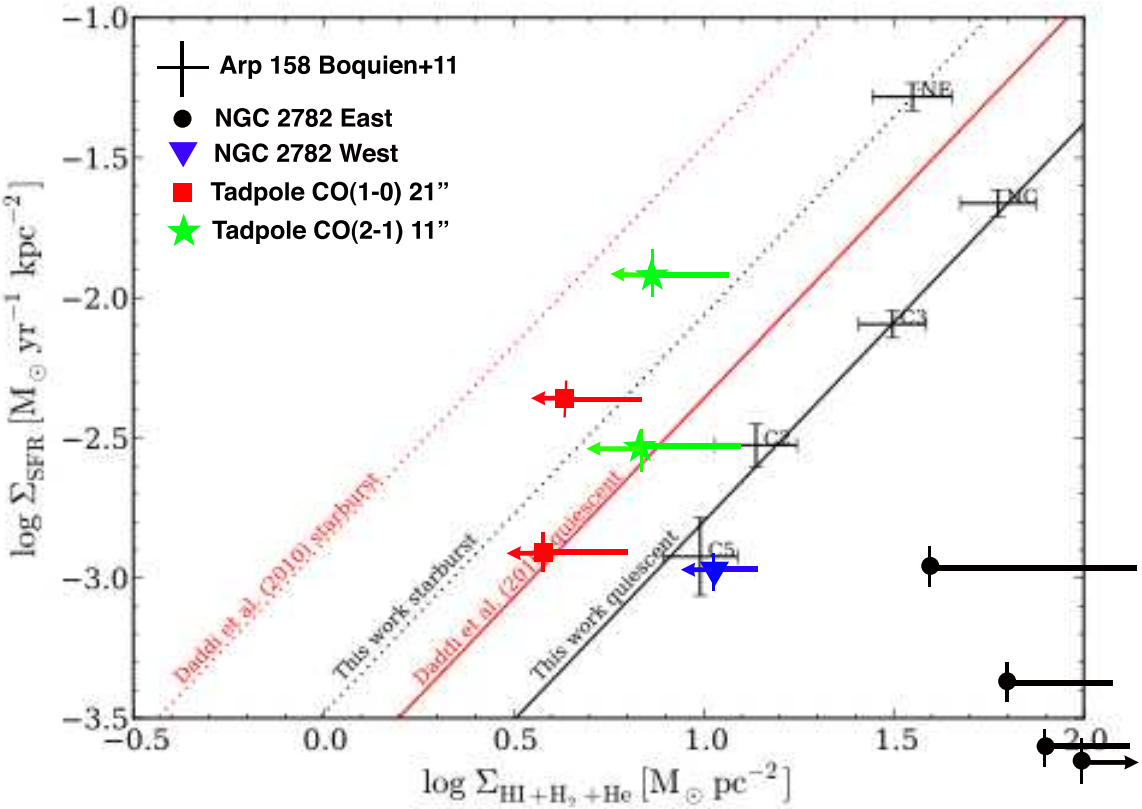

Figure 5.2: Figure 6 from Boquien et al. (2011) which plots the SFR density versus the total gas surface density for regions in the merger Arp 158. The regions from this thesis are over plotted as described in the legend. The arrows indicate upper limits for non-detections of CO(1-0) and the terminus of the arrow demarcates the lower bound of the gas density from the HI observation. The upper end of the arrows indicates the total gas density if the molecular gas mass is determined using a larger X_{CO} corresponding to a metallicity of $0.3Z_{\odot}$.

images. This will enable better determinations of ages, masses, extinctions, and metallicity of star clusters and star cluster complexes. Careful modeling and subtraction of the background light in the tidal tails will be necessary for correct SEDs as well.

Further examination of HII regions in minor merger tidal debris as well as in the main interacting galaxies can be done with existing ground based narrowband Hα images for 7 additional minor mergers. These observations can then be used to

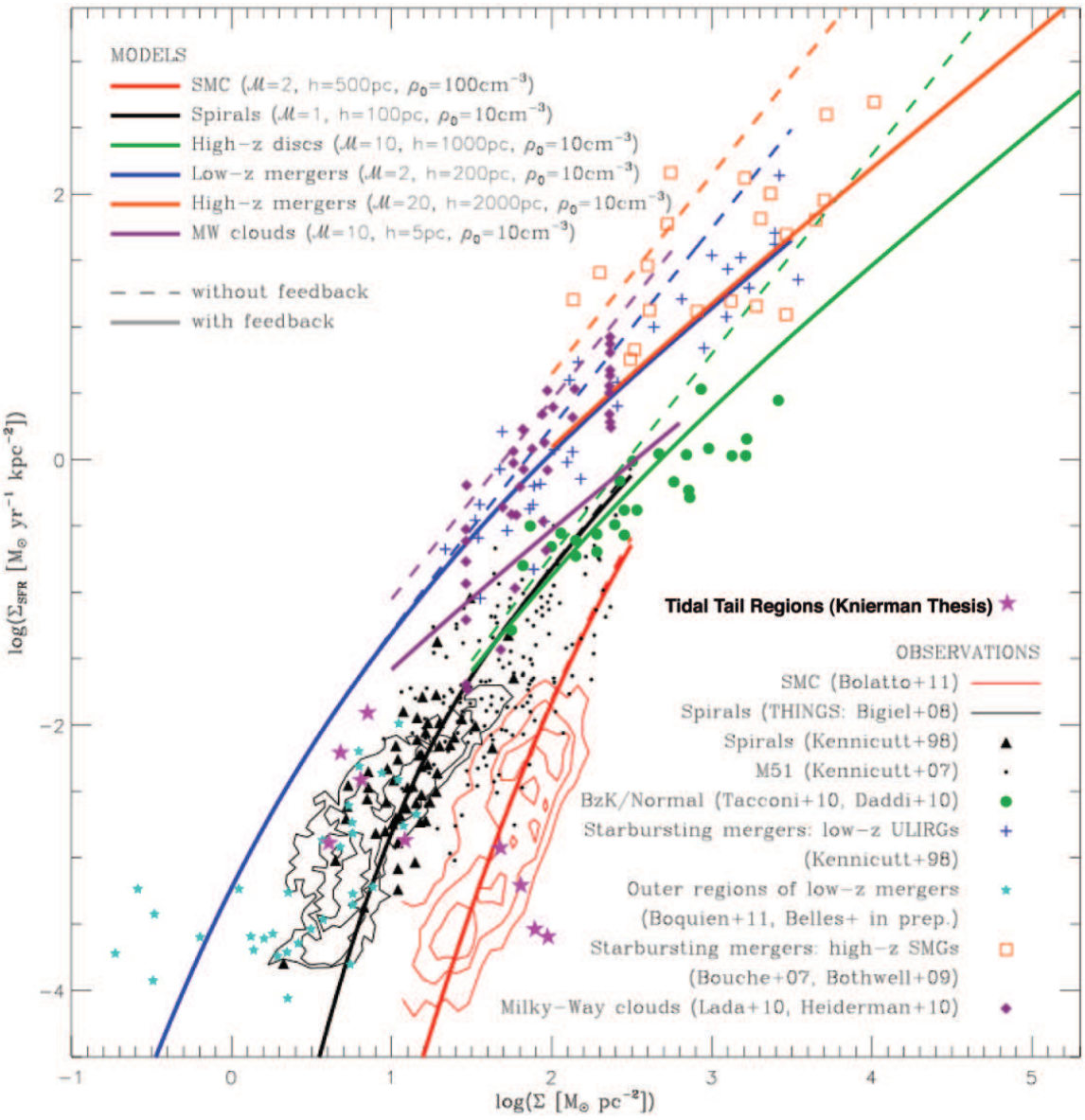

Figure 5.3: Figure 6 from Renaud et al. (2012) which plots the SFR density versus the total gas surface density for local and global regions in normal spirals, mergers, and dwarf galaxies. The regions from this work are over plotted with magenta stars.

determine the SFRs for local and global properties of the tidal debris and the minor merger as a whole. Early work on this sample (Knierman, 2010) examining 6 mergers (including NGC 2782, presented here), shows a weak trend of increased Hα luminosity (and, thus, SFR) with merger stage. However, the second highest Hα luminosity was from UGC 260 which is an early stage merger, indicating perhaps that individual merger properties are more important. If I add the Tadpole, its SFR is higher than all of those and it is a late stage merger, also indicating that the individual properties of the merger itself (e.g., gas content, gas density, pressure) are more important determinations of star formation than just the stage of the merger. Mullan et al. (2011) found that the age of the tail was not strongly correlated to the number of excess star clusters in the tail, also indicating more complex factors influencing star formation in tidal tails.

Additional studies of SFR in minor mergers can be done using UV observations. Archival data exists for some of the minor merger sample in FUV and/or NUV with GALEX and some minor mergers have archival UV imaging with HST. UV studies of star formation are often plagued by extinction considerations, however, tidal tails are generally thought to have less dust than the central regions of mergers giving UV a better chance at giving a more correct SFR. Also, while Hα emission generally probes star formation on relatively short timescales (< 10 Myr), UV emission can probe longer timescales (up to 100 Myr) and down to lower mass stars (B and A stars versus just O and B stars with Hα). These observations will help to determine better ages for young star clusters and better age and mass determinations for star clusters and determining whether TDGC and SSC 1 are tidal dwarf galaxies.

5.5.2 Molecular Gas

To determine a more complete picture of the gas properties in minor mergers, additional CO and HI observations are needed. In my sample of minor mergers, most published CO observations are only of the central regions. While I have taken previous observations with the ARO 12 meter submillimeter telescope (Knierman et al., 2013), its beam size is $\sim 1'$, making it useful for only the closest galaxies in my sample. IRAM has a beam size of $21''$, which is better than the ARO 12 meter, but is still very large compared to optical observations. To study star formation efficiency on smaller scales within tidal debris, a higher spatial resolution for CO(1-0) observations is needed to better match the Hα and [CII] data in NGC 2782 and the Tadpole as well as for the other sample galaxies. Rather than single dish submillimeter observations, observations with arrays such as ALMA, CARMA, or Plateau de Bure Interferometer (PdBI) are needed. CARMA has an angular resolution of a few arcseconds for CO(1-0) and access to the northern skies where NGC 2782 and the Tadpole reside. PdBI has $\sim 1''$ resolution, high sensitivity, and access to northern skies which would make it ideal for comparing to optical observations. Most ideal for tidal debris is ALMA which has very high spatial resolution ($< 0.1''$) and high sensitivity. However, ALMA is located in the Southern Hemisphere and can only observe more southern objects ($\delta < +40°$). However, many of the minor mergers in the larger sample are able to be observed with ALMA. By examining the molecular gas on smaller scales, some results in this work may be affected. For example, the Eastern tail of NGC 2782 has a very low SFE based on the observations presented here. However, the molecular gas detections are for a $55''$ beam which is much larger than the individual HII regions in the Eastern tail of NGC 2782. By having a better match between the scales sampled for each observation, the SFE can be determined with more accuracy.

5.5.3 Turbulence in Tidal Debris

The relationship between turbulence and star formation is a complicated one for any environment. Sometimes turbulence can help star formation, but other times it can suppress star formation. One outstanding question in tidal debris is how turbulence can affect star formation. Using velocity dispersions and line of sight velocities from VLA HI maps of mergers, Mullan et al. (2013) study the kinematics and turbulence in tidal debris and how it relates to star cluster formation. Their study uses a pixel by pixel approach to determine the line of sight velocity dispersion, v_{los}, and (squared) velocity dispersion, σ^2_{los}. These values are calculated by using the first and second moments, respectively, of the velocity-intensity distribution. The dynamical state of the gas is then determined from the kinetic energy density, $\Sigma_{KE} = \alpha\Sigma_{M_{HI}}\sigma^2_{los}$. For an isotropic velocity distribution, $\alpha = 3/2$, however, this assumption may not hold for tidal tails which have streaming motions in the tidal tails along with projection effects and inclination angle to consider. The transition between turbulent and thermal gas is at $\sigma_{los} \sim 10$ km s^{-1}. Mullan et al. (2013) also determine the line of sight velocity gradient across the plane of the sky, $dv_{los}/dr_{\perp}$ using the root mean square of the velocity gradient between the local pixel and neighboring pixels. For comparison, the value of the shear in the Milky Way near the sun is $dv_{los}/dr_{\perp} = 15$ km s^{-1} kpc^{-1}. Both tails of NGC 2782 have high column densities and kinetic energy density, but very few star clusters are in the Western tail. Further exploration of the local turbulence measures between the tails of NGC 2782 may lead to increased understanding of the cause for different star formation morphology in the two tails. Mullan et al. (2013) suggests that minor merger tidal debris have a higher kinetic energy density than tidal debris in major mergers, however, with only a couple minor mergers this is a tentative result. My sample of minor mergers can help to confirm this result with larger numbers. Many

of my sample mergers have archival VLA HI observations, and I will apply for EVLA time to complete the sample.

5.5.4 Formation of TDGs

There are two main hypotheses on TDG formation: a top-down scenario and a bottom-up one. In the top-down scenario, gas clouds are pulled out from the outer regions of the parent galaxy which then collapse to form a dwarf galaxy sized object at the end of the tidal tail (Elmegreen, Kaufman, & Thomasson, 1993). The bottom-up scenario consists a stellar component pulled out of the parent galaxy which then has gas falling into it to form new stars (Barnes & Hernquist, 1996). Observationally, these are different because the top-down scenario will have only a young stellar population, but the bottom-up scenario will have both an old and young stellar population. Whether TDGC has an old population with its young population is best found by using near-infrared imaging with optical imaging. Images taken with PISCES in JHK_s on the Bok 90-inch are available and can help determine whether there is a significant old population in TDGC. SSC 1 has been studied in near-infrared 2.2 microns in Jarrett et al. (2006) who determine that there is not a significant population of old stars indicating that SSC 1 likely formed via a top-down scenario. This is different than the 13 TDGs in the major mergers of Weilbacher et al. (2000) who found that TDGs in their sample had an old population along with the young population. This may indicate that TDGs in minor mergers may be formed via top-down scenarios, but major merger TDGs are formed via bottom-up formation. However, the TDGs in the major merger NGC 7252 have large HI masses indicating perhaps formation from gas cloud instabilities and a top-down scenario (Hibbard et al., 1994). Further work on more minor mergers with TDGs will help to determine whether the strength of the merger has a role in TDG formation or if individual system properties are more important.

5.6 Contribution of Tidal Tails to Star Formation

The total amount of star formation in minor merger tidal debris is examined to determine what its contribution is to star formation as a whole. To estimate the total amount of stars formed in the tidal debris of minor mergers, I take a bracketing approach, estimating an upper bound and a lower bound. In the first approach, I consider the mass of star clusters formed in the tidal debris. Even though these star clusters may or may not persist as separate entities over long timescales, the stars within them do contribute mass to their merger or the IGM. As a very generous upper bound for the stellar mass created in minor merger tidal debris, I take the mass of SSC 1 from Jarrett et al. (2006) using 2.2 micron images as 1.6×10^6 $M_\odot$, and assume that all star clusters in tidal debris are the same mass as SSC 1. This is an unrealistic value as most star clusters in the tidal debris are lower mass, but this gives us a maximum possible value. I also assume that the value from Tran et al. (2003) of ~ 40 star clusters in the tidal tail of the Tadpole is the same for all tidal tails in minor mergers. Using these values, I find a total mass in star clusters of 6.4×10^7 $M_\odot$. As a lower bound, I consider the mass of W235 from SED fitting in Knierman et al. (2013), 2.2×10^5 $M_\odot$. For the Western tail of NGC 2782, an overdensity of 10 star clusters is found in the Western tidal tail which gives lower bound on the total mass in star clusters in a tidal tail in a minor merger of 2.2×10^6 $M_\odot$.

The mass of star clusters formed in major merger tidal debris can be estimated in a similar manner. In the tidal tails of major merger NGC 4676 ("The Mice"), de Grijs et al. (2003) find about 40 star clusters with characteristic masses of 3×10^6 $M_\odot$. For the tidal tails of the Mice, the total mass in young star clusters is 1.2×10^8 $M_\odot$, assuming all star clusters are the same mass. This value for the total mass in young star clusters from major mergers is almost twice the value

calculated as the maximum value for minor merger tidal debris. Even though these estimates are very crude, this may indicate that more young star clusters and more massive star clusters are found in major mergers which is not surprising since major mergers have more material available for star formation.

Merger rates from various observational methods are synthesized together with a formulation to account for the visibility of mergers over time (Lotz et al., 2011) . They find that the merger rates differ based on the criteria for selection of the parent galaxies at different redshifts. They find that the minor merger rate at $z \sim 0.7$ is three times the major merger rate. The minor merger rate does not evolve strongly with lower redshift, as opposed to the major merger rate.

Kaviraj et al. (2013) use HST/WF3 observations of massive galaxies at $z \sim 2$ in the GOODS-S ERO to find that, contrary to expectation, major mergers account for only $\sim 27\%$ of the star formation at that redshift. On the other hand, $\sim 55\%$ of the star formation comes from late type galaxies which may come from minor mergers. If I assume that all of the star formation in late type galaxies at $z \sim 2$ comes from minor mergers and that the typical minor merger at this redshift is similar to the Tadpole galaxy (where 30-50% of the total star formation is occurring in the tidal tail), then 17-28% of all star formation at $z \sim 2$ comes from tidal debris in minor mergers. However, it is unlikely that all of the late type galaxies are star forming because of a minor merger. To determine what fraction of massive galaxies may be having a minor merger, I use the minor merger rate per galaxy from Lotz et al. (2011) calculated for $z \sim 2$, $R_{gal} = 0.8 - 1$, using the age of the universe at $z = 2$ as 3.3 Gyr (Wright, 2006). Using this rate, I find that between 14-28% of the total star formation at $z \sim 2$ may be due to star formation in tidal tails like in the Tadpole galaxy. Of course, not every minor merger may behave like the Tadpole, so this is an upper limit to the contribution to star formation at this redshift.

Since major mergers are less common, what are their contributions to the star formation at $z \sim 2$? Using NGC 4676 (The Mice) and Hα observations in Hibbard & van Gorkom (1996), they find that 31% of the total Hα luminosity is in the tidal debris which, translated to a SFR using Kennicutt (1998b), indicates that 34% of the total current star formation is in the tidal debris. This is similar to the lower bound for the Tadpole. Using the major merger rate at $z \sim 2$ from Lotz et al. (2011) ($R_{gal} \sim 0.6$) and the fraction of star formation due to major mergers at that redshift (27%), I find that the tidal debris of major mergers may account for $\sim 16\%$ of star formation at that redshift. This value is at the low end of the fraction of star formation from minor merger tidal debris as calculated above.

Due to the higher frequency of minor mergers, they may account for more star formation than major mergers, particularly at higher redshifts. Even if major mergers may form more stars in their tidal debris, the higher merger rate from minor mergers can compensate for the lower SFR in tidal debris. This indicates the importance of studying minor merger tidal debris since it can contribute to star formation on cosmic scales, even more than major mergers.

Adelman-McCarthy, J. K., et al. 2008, ApJS, 175, 297

Appleton, P., et al. 2006, ApJ, 639, 51L

Arnett, D. 1996, Supernovae and Nucleosynthesis, Princeton University Press, Princeton

Arp, H. C. 1966, Atlas of Peculiar Galaxies (Pasadena: CalTech)

Arp H. C., Madore B. F., 1987, A Catalogue of Southern Peculiar Galaxies and Associations 2 volume set, Arp, H. C. & Madore, B. F., ed.

Barker, M.K., Ferguson, A. M. N., Cole, A. A. et al. 2011, MNRAS, 410, 504

Barnes, J. E. 1988, ApJ, 331, 699

Barnes 1998, in Galaxies: Interactions and Induced Star Formation, ed. R. C. Kennicutt, Jr., F. Schweizer, J. E. Barnes, D. Friedli, L. Martinet, & D. Pfenniger (Berlin: Springer-Verlag), 275

Barnes, J. 2004, MNRAS, 350, 798

Barnes, J. E., & Hernquist, L. 1996, ApJ, 471, 115

Barth, A. J., Ho, L. C., Filippenko, A. V., & Sargent, W. L. W. 1995, AJ, 110, 1009

Bastian, N. et al. 2005a, A&A, 431, 905

Bastian, N. et al. 2005b, A&A, 435, 65

Bica, E. & Schmitt, H. R. 1995, ApJS, 101, 41

Bigiel, F., Leroy, A.K. Walter, F. et al. 2008, AJ, 136, 2846

Bigiel, F., Leroy, A., Walter, F., Blitz, L., Brinks, E., de Blok, W.J.G., & Madore, B. 2010, AJ, 140, 1194

Bik, A., Lamers, H.J.G.L.M, Bastian, N., Panagia, N., & Romaniello, M. 2003, A&A, 397, 473

Blitz, L. & Rosolowsky, E. 2006, ApJ, 650, 933

Bolatto, A., Leroy, A.K., Jameson, K., et al. 2011, 741, 12

Boquien, M., Lisenfeld, U., Duc, .-A., Braine, J., Bournaud, F., Brinks, E., & Charmandaris, V. 2011, A&A, 533, 19

Boselli, A., Gavazzi, G., Lequeux, J. & Pierini, D. 2002, A&A, 385, 454

Bournaud, F., Duc, P.-A., Amram, P., Combes, F., Gach, J.-L. 2004, A&A, 425, 813

Braine, J. et al. 2001, A&A, 378, 51

Bresolin, F. & Kennicutt, R.C. 1997, AJ, 113, 975

Briggs, F. H., et al. 2001, A&A,380, 418

Bruzual, A. G., & Charlot, S. 1993, ApJ, 405, 538

Bruzual, G., & Charlot, S. 2003, MNRAS, 344, 1000

Bullock, J. & Johnston, K. 2005, ApJ, 638, 585

Calzetti, D. et al. 2005, ApJ, 633, 871

Calzetti, D., Kennicutt, R.C., Engelbracht, C.W., et al. 2007, ApJ, 666, 870

Cen et al. 2005, ApJ, 635, 86

Chien, L.-H., Barnes, J., Kewley, L., Chambers, K. 2007, ApJL, 660, 105

Chomiuk, L. & Povich, M.S. 2011, AJ, 142, 197

Conselice, C. et al. 2000, AJ, 119, 79

Daddi, E., Elbaz, D., Walter, F., et al. 2010, ApJL, 714, 118

Davé, R. & Oppenheimer, B. 2007, MNRAS, 374, 427

Davies, R., Sugai, H., & Ward, M. 1998, MNRAS, 295, 43

de Grijs, R., Lee, J. T., Mora Herrera, M. C., Fritze-v. Alvensleben, U., & Anders, P. 2003, New Astronomy, 8, 155

De Looze, I., Baes, M., Bendo, G., Cortese, L., & Fritze, J. 2011, MNRAS, 416, 2712

Devereux, N. A. 1989, ApJ, 346, 126

Dolphin, A. 2009, PASP, 121, 655

Duc, P.–A., Belles, P.-E., Brinks, E., & Bournaud, F. 2012, in Molecular Gas, Dust, and Star Formation in Galaxies, IAU Symposium No. 292, eds. T. Wong & J. Ott, 323

Duc, P.–A., & Mirabel, I. F. 1994, A&A, 289, 83

Duc, P.–A., & Mirabel, I. F. 1998, A&A, 333, 813

Duc, P.–A., & Mirabel, I. F. 1999, in Galaxy Interactions at Low and High Redshift, IAU Symposium No. 186, eds. D. Sanders & J. Barnes, 61

Duc, P.-A., Brinks, E., Springel, V., Pichardo, B., Weilbacher, P., & Mirabel, I. F. 2000, AJ, 120, 1238

Duc, P.-A., Bournaud, F., & Masset, F. 2004, A&A, 427, 803

Duc, P.-A., Bournaud, F. & Boquien, M. 2006, Proceedings of "Triggered Star Formation in a Turbulent ISM". Eds. B. Elmegreen & Palous

Elmegreen, B.G. 1993, ApJ, 419, L29

Elmegreen, Bruce G. 2007, ApJ, 668, 1064

Elmegreen, B. G., & Efremov, Y. N. 1997, ApJ, 480, 235

Elmegreen, B.G. & Hunter, D.A. 2004, AJ, 128, 2170

Elmegreen, B. G., Kaufman, M., & Thomasson, M. 1993, ApJ, 412, 90

Elmegreen, B.G., & Scalo, J. 2004, ARA&A, 42, 211

Elmegreen, D. E., Chromey, F.R., McGrath, E. J., Ostenson, J. M. 2002, AJ, 123, 1381

Elmegreen, D.E., & Salzer, J.J. 1999, AJ, 117, 764

Feldmeier, J., Ciardullo, R., Jacoby, G., & Durrell, P.R. 2004, 615, 196

Ferguson, A. M. N. 2007, in "From Stars to Galaxies: Building the Pieces to Build up the Universe" ASP Conf. Series, Ed. Vallenari, A., et al., Vol. 374, 239

Ferreiro, D. L., Pastoriza, M. G. & Rickes, M. C. 2008, A&A, 481, 645

Gallagher, S. C., Charlton, J. C., Hunsberger, S. D., Zaritsky, D. & Whitmore, B. C. 2001, AJ, 122, 163

Genzel, R., Tacconi, L.J., Combes, F., et al. 2011, ApJ, 746, 69

Greisen, E. W., 2003, in Information Handling in Astronomy – Historical Vistas, Heck, A. ed., Kluwer Academic Publishers, Dordrecht, Astrophysics and Space Science Library, 285, 109.

Grogin, N.A., Lucas, R.A., Golimowski, D., & Biretta, J. 2010, HST WFPC2 Instrument Science Report, 3, 1

Guhathakurta, P., & Reitzel, D. B. 1998, in ASP Conf. Ser. 136, Galactic Halos, ed. D. Zaritsky (San Francisco: ASP) 22

Harris, J. 2007, ApJ, 658, 345

Hernquist, L. & Mihos, J. C. 1995, ApJ, 448, 41

Hibbard, J. E., Guhathakurta, P., van Gorkom, J. H., & Schweizer, F. 1994, AJ, 107, 67

Hibbard, J. E., & Mihos, J. C. 1995, AJ, 110, 140

Hibbard, J. E., & van Gorkom, J. H., 1996, AJ, 111, 655

Hibbard, J. E., van Gorkom, J. H., Rupen, M. P., & Schiminovich, D. 2001, in ASP Conf. Ser. 240, Gas and Galaxy Evolution, eds. J. E. Hibbard, M. P. Rupen and J.H. van Gorkom (ASP, San Francisco), 659

Hollenbach, D.J., & Tielens, A.G.G.M. 1997, ARA&A, 35, 179

Holmberg, E. 1941, ApJ, 94, 385

Holmberg, E. 1958, Lund Obs. Medd. II, 136, 1

Holtzman et al. 1992, AJ, 102, 691

Holtzman et al. 1995, PASP, 107, 1065

Horellou, C., & Koribalski, B. 2007, A&A, 464, 155

Hopkins, P., Cox, T.J., Hernquist, L., Narayanan, D., Hayward, C.C., Murray, N. 2013, MNRAS, 430, 190

Hunsberger, S. D., Charlton, J. C., & Zaritsky, D. 1996, ApJ, 462, 50

Huxor, A. P., et al. 2005, MNRAS, 360, 1007

Ibata, R. A., et al. 1997, AJ, 113, 634

Iglesias-Páramo, J., & Vílchez, J. M. 2001, ApJ, 550, 204

Jarrett, T.H., Polletta, M., Fournon, I.P., et al. 2006, AJ, 131, 261

Jester, S., Schneider, D. P., Richards, G., Green, R., Schmidt, M., et al. 2005, AJ, 130, 873

Jog, C. J., & Solomon, P. M. 1992, ApJ, 387, 152

Jogee, S. Kenney, J. D. P., & Smith, B. J. 1998, ApJ, 494, L185

Kaviraj, et al. 2013, MNRAS, in review, astro-ph, 1210.4160

Kennicutt, R.C. 1989, ApJ, 344, 685

Kennicutt, R. C. 1998a, in Induced Star Formation, Galaxies: Interactions and Induced Star Formation (Berlin: Springer)

Kennicutt, R.C. 1998b, ARA&A, 36, 189

Kennicutt, R. C., Calzetti, D., Walter, F., et al. 2007, ApJ, 671, 333

Kenyon, S. J., Gńomez, M., & Whitney, B. A. 2008, Handbook of Star Forming Regions, Volume I, ed. B. Reipurth, 405

Kewley, L. & Dopita, M. 2002, ApJS, 142, 35

Knierman, K. A., Hunsberger, S. D., Gallagher, S. C., Charlton, J. C., Whitmore, B. C., Kundu, A., Hibbard, J. E., & Zaritsky, D. 2003, AJ, 126, 1227

Knierman, K., 2010, Galaxy Wars: Stellar Populations and Star Formation in Interacting Galaxies, ASP Conference Series, Vol. 423. Edited by B. Smith, N. Bastian, S.J.U. Higdon, and J. L. Higdon. San Francisco: Astronomical Society of the Pacific, 342

Knierman, K. A., Knezek, P. M., Scowen, P., Jansen, R., & Wehner, E. 2012, ApJ, 749, L1

Knierman, K.A., et al. 2013, ApJ, in review (K13)

Kolbulnicky, H. & Kewley, L. 2004, ApJ, 617, 240

Konstantopoulos, I.S., Gallagher, S.C., Fedotov, K., Durrell, P.R., Heiderman, A., Elmegreen, D.M. et al. 2010, ApJ, 723, 197

Konstantopoulos, I.S., Gallagher, S.C., Fedotov, K., Durrell, P.R., Tzanavaris, P., Hill, A.R., et al. 2012, ApJ, 745, 30

Kregel, M. & Sancisi, R. 2001, A&A, 376, 59

Kroupa, P. 1997, New Astronomy, 2, 139

Kroupa, P., Theis, C., & Boily, C. M. 2005, A&A, 431, 517

Krumholz, M.R., & McKee, C. 2005, ApJ, 630, 250

Krumholz, M.R., & Tan, J. 2007, ApJ, 654, 304

Lada, C. J., & Lada, E. A. 2003, ARA&A, 41, 57

Larsen, S. S., & Richtler, T. 1999, A&A, 345, 59

Larsen, S.S. & Richtler, T. 2000, A&A, 354, 836

Lee, J. 2006, Ph.D. Thesis, University of Arizona

Leitherer, C. et al.1999, ApJS, 123, 3

Leroy, A.K., Bolatto, A., Gordon, K., et al. 2011, ApJ, 737, 12

Lotz, J. et al. 2011, ApJ, 742, 103

Mackey, A. D., et al. 2006, ApJ, 653, L105

Majewski, S. R., et al. 2003, ApJ, 599, 1082

Mathis, J. S. 1990, ARA&A, 28, 37

Maybhate, A., Masiero, J., Hibbard, J. E., Charlton, J. C., Palma, C., Knierman, K., & English, J. 2007, MNRAS, 381, 59

Meurer, G. R., Heckman, T. M., Lietherer, C., Kinney, A., Robert, C., & Garnett, D. R. 1995, AJ, 110, 2665

Mihos, C.J., Bothun, G.D., & Richstone, D.O. 1993, ApJ, 418, 82

Mihos, J. C., & Hernquist, L. 1994, ApJ, 425, 13L

Miller, B., Whitmore, B., Schweizer, F., & Fall, S.M. 1997, AJ, 114, 2381

Mirabel, I. F., Booth, R. S., Johansson, L. E. B., Garay, G., & Sanders, D. B. 1990, A&A, 236, 327

Mirabel, I. F., Dottori, H., & Lutz, D. 1992, A&A, 256, L19

Mookerjea, B. et al. 2011, A&A, 232, 152

Morrissey, P., Conrow, T., Barlow, T., et al. 2007, ApJS, 173, 682

Mould, J. R., Huchra, J.P., Freedman, W. L., Kennicutt, R.C., Ferrarese, L., Ford, H.C., et al. 2000, ApJ, 529, 786

Mullan, B., Konstantopoulos, I.S., Kepley, A.A., et al. 2011, ApJ, 731, 93

Mullan, B., Kepley, A.A., Maybhate, A., et al. 2013, ApJ, 768, 194

Naab, T. & Ostriker, J. 2006, MNRAS, 366, 899

Oberst, T.E., Parshely, S.C., Stacey, G.J., Nikola, T. et al. 2006 ApJL, 652, L125

Oke, J.B. 1990, AJ, 99, 162

Pagel, B. E. J., Edmunds, M. G., Blackwell, D. E., Chun, M. S., & Smith, G. 1979, MNRAS, 189, 95

Pak, S. et al. 2004, ApJ, 609, 692

Paturel G., Petit C., Prugniel P., Theureau G., Rousseau J., Brouty M., Dubois P., Cambrésy L., 2003, A&A, 412, 45

Pellerin, A., Meyer, M., Harris, J., Calzetti, D. 2007, 658, 87

Peroux, C., Bouche, N., Kulkarni, V.P., York, D., Vladilo, G. 2007, MNRAS, 386, 2209

Pilbratt, G.L., Riedinger, J.R., Passvogel, T. et al. 2010, A&A, 518, L1

Pisano, D.J., & Wilcots, E. 2003, ApJ, 584, 228

Poglitsch, A., Waelkens, C., Geis, N. et al. 2010, A&A, 518, L2

Portegies Zwart, S., McMillan, S. & Gieles, M. 2010, ARA&A, 48, 431

Putman, M. E., Staveley-Smith, L., Freeman, K. C., Gibson, B. K., & Barnes, D. G. 2003, ApJ, 586, 170

Renaud, F., Kraljic, K., & Bournaud, F. 2012, ApJ, 760, 16

Robin, A. C., Reylé, C., Derrière, S., & Picaud, S. 2003, A&A, 409, 523

Rosolowsky, E., Keto, E., Matsushita, S., Willner, S. P. 2007, ApJ, 661, 830

Salpeter, E. 1955, ApJ, 121, 161

Schlafly, E.F., & Finkbeiner, D.P. 2011, ApJ, 737, 103

Schlegel, D. J., Finkbeiner, D. P., & Davis, M. 1998, ApJ, 500, 525

Schombert, J. M., Wallin, J. F., & Struck–Marcell, C. 1990, AJ, 99, 497

Schweizer, F. 1978, in Structure and Properties of Nearby Galaxies, ed. E. M. Berkhuijsen & R. Wielebinski (Reidel, Dordrecht), 279

Schweizer, F., Miller, B., Whitmore, B., & Fall, S. M. 1996, AJ, 112, 1839 (S96)

Searle, L. & Zinn, R. 1978, ApJ, 225, 357

Smith, B. 1994, AJ, 107, 1695

Smith, B. Struck, C., Kenney, J.D.P., & Jogee, S. 1999, AJ, 117, 1237

Solomon, P.M., & Vanden Bout, P.A. 2005, ARA&A, 43, 677

Stacey, G. et al. 1991, ApJ, 373, 423.

Temporin, S, Weinberger, R., Galaz, G., & Kerber, F. 2003, ApJ, 584, 239

Teyssier, R., Chapon, D., & Bournaud, F. 2010, ApJL, 720, 149

Toomre, A. & Toomre, J. 1972, ApJ, 178, 623

Toomre, A. 1977, in The Evolution of Galaxies and Stellar Populations, edited by B. M. Tinsley and R. B. Larson (New Haven: Yale Univ.), 401

Torres-Flores, S., et al. 2012, MNRAS, 421, 3612

Tran, H.D. et al. 2003, ApJ, 585, 750

Trancho, G., Bastian, N., Schweizer, F., Miller, B. W. 2007, ApJ, 658, 993

van Zee, L., et al. 1998, AJ, 116, 2805

Vandenbussche, B., Blommaert, J., Contursi, A., et al. 2011, PACS Spectroscopy Performance & Calibration, 2.4, 1

Vazquez, G. & Leitherer, C. 2005, ApJ, 621, 695

Venn, K., et al. 2005, AJ, 128, 1177

Walker, I., Mihos, J. C., & Hernquist, L. 1996, ApJ, 460, 121

Wallin, J. 1990, AJ, 100, 1477

Walter, F., Martin, C. L., & Ott, J. 2006, AJ, 132, 2289

Wehner, E. 2005, Ph.D. Thesis, University of Wisconsin - Madison

Wehner, E. & Gallagher, J.S. 2004, ApJL, 618, 21.

Weilbacher, P. M., Duc, P.-A., Fritze-v.Alvensleben, U., Martin, P., & Fricke, K. J. 2000, A&A, 358, 819

Weilbacher, P. M., Fritze-v.Alvensleben, U., Duc, P.-A., & Fricke, K. J. 2002, ApJ, 579, L79

Weilbacher, P.M, 2002, Ph.D. thesis, Universität Göttingen

Weilbacher, P. M., Duc, P.-A., & Fritze-v.Alvensleben, U. 2003, A&A, 397, 545

Werk, J. K., Putman, M.E., Meurer, G., R., Santiago-Figueroa, N. 2011, ApJ, 735, 71

Whitmore, B. C., Schweizer, F., Leitherer, C., Borne, K., & Robert, C. 1993, AJ, 106, 1354

Whitmore, B. C., Heyer, I., & Casertano, S. 1999, PASP, 111, 1559

Whitmore, B., Zhang, Q., Leitherer, C., Fall, S.M., Schweizer, F., & Miller, B. 1999, AJ, 118, 1551

Wilke, K., Klaas, U., Lemke, D., Mattila, K., Stickel, M., & Haas, M. 2004, A&A, 414, 69

Wolfire, M., Hollenbach, D., & McKee, C. F. 2010, ApJ, 716, 1191

Wright, E.L. 2006, PASP, 118, 1711

Yoshida, M., Taniguchi, Y., & Murayama, T. 1994, PASJ, 46, 195L

Yun, M. S., Ho, P. T. P., & Lo, K. Y. 1994, Nature, 372, 530

Zentner, A. & Bullock, J. 2003, ApJ, 598, 49

Zepf, S., Ashman, K., English, J., Freeman, K., & Sharples, R. 1999, AJ, 118, 752